

W(H)YDOC 15



5th International Workshop of Young Doctors in Geomechanics

École des Ponts ParisTech
Champs-sur-Marne, France
December 2 – 4, 2015



École des Ponts
ParisTech

J.M. Pereira, P. Delage, S. Ghabezloo & M. Vandamme (editors)
École des Ponts ParisTech, France

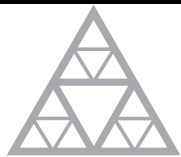
UNIVERSITÉ
— PARIS-EST

W(H)YDOC 15

5th International Workshop of Young Doctors in Geomechanics

J.M. Pereira, P. Delage, S. Ghabezloo & M. Vandamme (editors)
École des Ponts ParisTech, France

Navier



École des Ponts
ParisTech

LABEX MMCD

ÉCOLE DOCTORALE UNIVERSITÉ PARIS-EST
Sciences, Ingénierie et Environnement



ALERT Geomaterials



CFMR **CFMS**



**ÉCOLE FRANÇAISE
DU BÉTON**
www.efbeton.com



LafargeHolcim



**Sols
Mesures**
Géotechnique & Agronomie

 **Sanchez
Technologies** | Thermodynamics &
Core Analysis
Laboratory Instruments
A division of **Core Laboratories**

Foreword

Following the previous W(H)YDOC Workshops (2002, 2005, 2008, 2012), the scope of W(H)YDOC 15 (Paris, 2 – 4 December 2015) is to bring together young geotechnical doctors, as well as students completing their last PhD year, within an informal invited workshop. The Workshop aimed at favouring informal and constructive exchanges about recent research results and ideas.

A total of 18 contributions coming from 10 countries were presented during the Workshop. This book contains the summaries of these contributions, outlined in short papers provided by the authors. The workshop, as well as this book, is organised in 3 sessions: Computational geomechanics (Chairman Prof. Patrick Dangla, École des Ponts ParisTech), Experimental geomechanics (Chairman Prof. Yves Guéguen, Ecole Normale Supérieure Ulm, France), Multiscale analysis (Chairmans Prof. Antonio Gens, UPC Barcelona, Spain & Prof. Christopher Spiers, U. Utrecht, Netherlands) and Stability and structures (Prof. Manoel Cordao Neto, University of Brasilia, Brasil).

We acknowledge Prof. Antonio Gens, Prof. Christopher Spiers and Prof. Henri Van Damme for their kind acceptance to hold the Keynote Lectures presented during the Workshop. We are also grateful to the session chairmen.

We are grateful too to all the "Young Doctor Contributors" who participated to the three days meeting. Thanks are also due to their Tutors.

This Workshop was supported by the sponsorship of ALERT Geomaterials, CFMR, CFMS, Ecole des Ponts ParisTech, Ecole Française du Béton, Labex MMCD, Lafarge-Holcim, Sanchez Technologies, Sols Mesures, Université Paris-Est. Their participation is kindly acknowledged.

Jean-Michel Pereira
Pierre Delage
Siavash Ghabezloo
Matthieu Vandamme

*Laboratoire Navier
École des Ponts ParisTech
Champs-sur-Marne, December 2015*

Table of contents

Computational geomechanics	6
Insights into the response of a gallery sealing over the entire life of a deep repository, Ruiz Daniel	8
A robust numerical framework for reactive transport in cement paste, Georget Fabien [et al.]	14
The role of rheology and pore water pressure during the modelling of landslides propagation with SPH, Dutto Paola [et al.]	20
Experimental geomechanics and modelling	26
Comparison of experimentally determined and theoretically predicted elastic properties of VTI shale under uniaxial loading, Sviridov Viacheslav [et al.]	27
Experimental and modelling study of concrete delayed strain in a nuclear containment building, Hilaire Adrien	33
Early-age non-aging viscoelastic properties of cement paste: lessons learned from macroscopic testing, Irfan-Ul-Hassan Muhammad [et al.]	39
Early-age behaviour of oil-well cement and well integrity, Agofack Nicolaine	45
Brittle and semibrittle deformation of limestones: experiments and model, Nicolas Aurélien [et al.]	51

Constitutive behaviour and microstructure	57
Strength, stability, and microstructure of simulated calcite faults sheared under laboratory conditions spanning the brittle-plastic transition, Verberne Berend Antonie [et al.]	58
Significance of mineralogy for hydro-mechanical behaviour of clays, Baile Wiebke	64
Quantitative comparison between the crack apertures, strains and microstructure in Tournemire clayrocks, Fauchille Anne-Laure [et al.]	70
Multiscale modelling and analysis	76
Development and application of a multiscale modelling approach for hydromechanical coupling, Van Den Eijnden Bram [et al.]	77
Multiscale modelling of the thermo-viscoelastic properties of cement-based materials and structures at early-age, Honorio Tulio [et al.]	83
Methodologies for an efficient forecast of the delayed behaviour of prestressed concrete based on imaging and numerical simulations, Lavergne Francis [et al.]	89
A micro-mechanical study of cemented granular materials, Tengattini Alessandro	95
Structures	101
Tunnelling in anisotropic squeezing conditions, Tran-Manh Huy	102
Mechanical characteristics of monopile foundation in sand for offshore wind turbine, Duan Nuo [et al.]	108
A probabilistic approach for rainfall-induced landslide susceptibility at large scale, Fanelli Giulia	114

Computational geomechanics

INSIGHTS INTO THE RESPONSE OF A GALLERY SEALING OVER THE ENTIRE LIFE OF A DEEP REPOSITORY

D.F. Ruiz (daniel.felipe.ruiz@upc.edu)

Department of Geotechnical Engineering and Geosciences, Universitat Politècnica de Catalunya (UPC), Barcelona, Spain.

ABSTRACT. Currently underground storage is considered as the most suitable management procedure for high-level nuclear waste. A deep repository is composed by different kinds of galleries. Keeping in mind that the final goal is the isolation of the waste from the biosphere, an effective sealing system of the galleries has to be implemented. The response of the sealing system involves the entire life of the repository, including the construction and the operational phase. A numerical modelling of the short and long term hydro-mechanical response of typical sealing systems placed in the main galleries of a repository located in claystone is presented in this paper. Geometrical aspects (joints, gaps, etc.) and viscous and anisotropy behaviour of the host rock are taken into account in order to obtain a realistic response of the system.

1. Seal structure

A deep nuclear waste repository implies several types of excavation that depends on its design and on the host rock in which it is emplaced. In the particular case of claystones the nuclear waste may be placed in micro-tunnels and the different areas will be connected through a network of main galleries with diameters of several meters. Access ramps and shafts involve also large dimensions.

The seal structure evaluated in this work concerns the arrangement designed to isolate the connecting galleries, ramps and shafts after the operational phase of the repository. A tentative configuration of the seal system consists of a central core built with swelling bentonite placed between two support concrete plugs. The plugs are in contact with the filling of the gallery, made with recompacted crushed host rock. (Figure 1). As reported in Gens (2003), the performance of these systems relies on achieving low permeability values in the bentonite and surrounding rock (particularly in the Excavation Damaged Zone) and low transmissivity values along possible discontinuities (contacts and eventual gaps). The issues concerning seal behaviour are similar to those arising in the design of engineered barriers, with the important difference that no high temperatures are present.

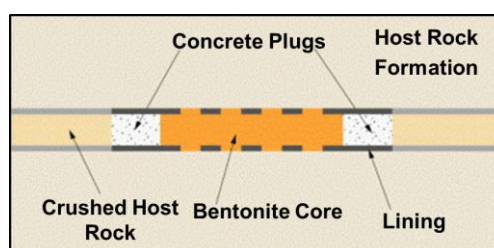


Figure 1. Configuration of the seal structure.

The performance of the sealing system is dependent on all phases of the repository:

- The excavation creates the EDZ around the openings.
- The ventilation applied during the operational phase.
- The installation conditions such dry density and compaction water content of the sealing material, presence of gaps and mode of eventual filling.

- The long-term behaviour after water pressure equilibration between the seal and the host rock; long term creep deformation of the host rock will compress the seal system.

2. Host rock modelling

Due to the characteristics of sealing systems, a hydro-mechanical (HM) analysis of the behaviour of the host rock is necessary. Although the seal system is applicable to any type of host rock, the study is focussed on the Callovo-Oxfordian (COx) claystone. This argillaceous formation located at the depth of 500 m in the site of Meuse/Haute Marne (MHM) is considered as a potential host rock for high level radioactive nuclear waste repository in France (Andra, 2012).

A major part of the observed macroscopic behaviour has its roots in the underlying microfabric of the material (Gens, 2011). A main contributor to the structural effects of the microfabric is the presence of calcium carbonate in a random manner that leads to local differential strains contributing to the development of microfissures. The above characteristics generate brittleness and progressive failure. Another important feature is the fabric anisotropy generated by particle realignment during the process of sedimentation.

COx has low permeability values that are influenced by the anisotropic microfabric. Higher values are often associated with flow parallel to bedding planes. Damage process increases the permeability by several orders of magnitude.

Host Formation (COx) and EDZ are simulated by a phenomenological model through an visco-elastoplastic stress-strain relationship based on linear elasticity and Mohr-Coulomb yield criterion. The following features are also incorporated:

- Non-linear hardening softening Law.
- Anisotropic failure criterion (Mánica et al; 2015)
- Creep deformations using a modified Lemaitre's Law in which long term deformations are function of the deviatoric stress (equation 1)

$$\dot{\epsilon}_{ij}^{vp} = \frac{2}{3} \frac{\dot{\epsilon}_{vp}}{q} S_{ij} \dot{\epsilon}_{vp} = \gamma (q - \sigma_s)^n (1 - \epsilon_{vp})^m q = \left(\frac{3}{2} s : s \right)^{1/2} \quad (1)$$

Concerning hydraulic phenomena, the Van Genuchten retention curve, the variation of the intrinsic permeability K_i with porosity and the variation of the relative hydraulic conductivity with degree of saturation S_r are required (DIT-UPC, 2002).

This argillaceous material is being intensely studied by means of laboratory and in situ tests at both small and large field scales. Figure 2 shows two types of laboratory tests performed at sample scale. A triaxial test under confined pressure of 12 MPa close to the in situ stress state and creep tests at the same confined pressure and different deviatoric stress levels. The dotted lines correspond to the numerical modelling of the tests. Features like non-linear hardening, softening and creep deformation provide a good approximation to the experimental results.

The formation presents anisotropic stress state and the shape of the EDZ depends on the orientation of the excavation. The analysis of a case of a gallery in the underground laboratory where the orientation ensures that the transverse in situ stress is nearly isotropic is shown in Figure 3. Therefore the anisotropic response of the rock to excavations and the shape of the damaged zone are only due to the microfabric. In the modelling, the shape of the EDZ is represented by the plastic multiplier and the

anisotropic and long term convergence measurements are well captured. This response involves hydro-mechanical phenomena where the consolidation process and creep deformations occur at the same time.

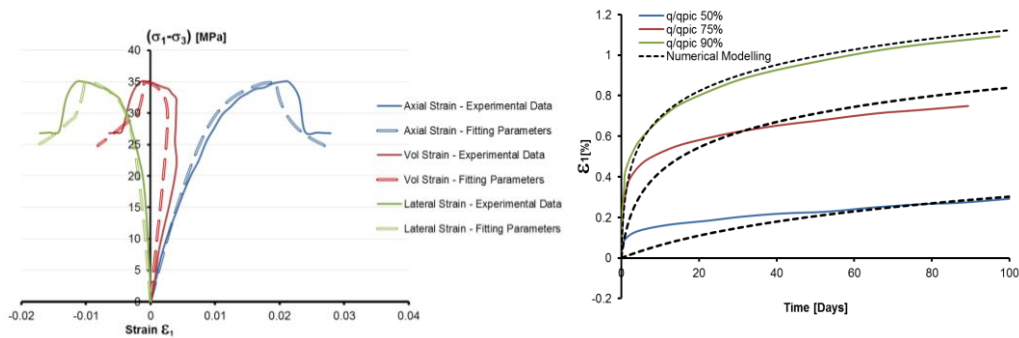


Figure 2. Modelling of laboratory tests. Triaxial (left). Creep (right)

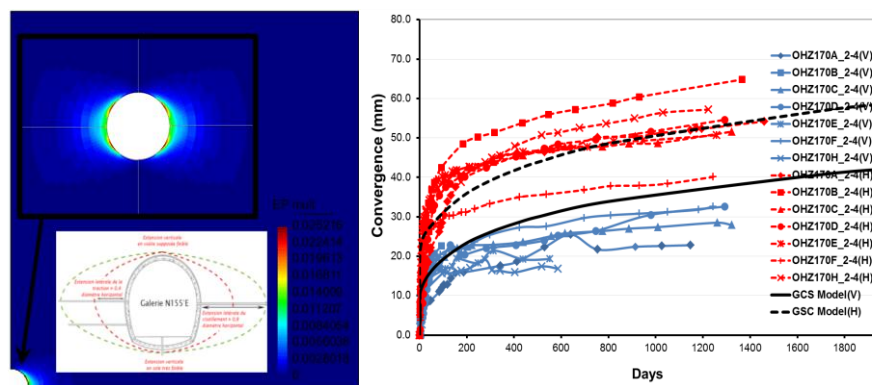


Figure 3. Modelling of field convergence. Excavation Damage Zone shape (left). Convergence comparison of computed results and observations (right).

3. Contact effects

The installation of seal structure involves contacts between the different components. Therefore the modelling of the contact effects is required in order to take into account the real performance of the structure. Stress distributions and the stability of the concrete plugs as supporting elements are only model realistically if contact effects are considered.

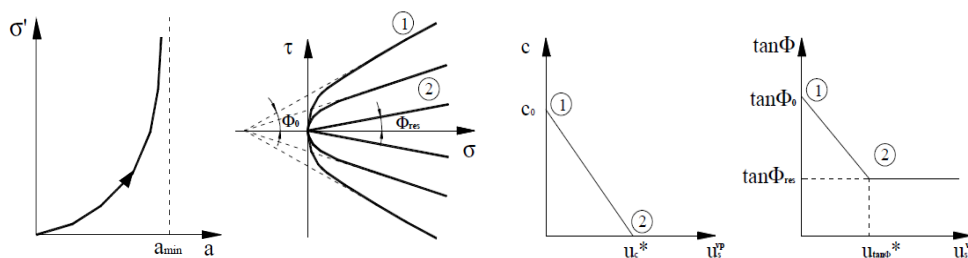


Figure 4. Constitutive law of contact element. From left to right :Elastic law, yield surface and softening law.

The implementation of a joint element formulated by Zandarín (2010) in the finite element code CODE-BRIGHT (DIT-UPC, 2002) was performed. Regarding the mechanical elastic law, the normal stiffness depends on the aperture while the tangent stiffness is an independent parameter. Viscoplastic behaviour is generated with a

hyperbolic Mohr-Coulomb yield criterion with a Perzyna approach and the softening law is a function of relative displacement (Figure 4).

Transversal fluxes depend on the permeability of the porous media which bound the contact and the longitudinal fluxes are function of the joint aperture and roughness profile that in the case of artificial contacts is almost negligible. Perfect mobility of the water inside the contact was considered.

4. Expansive behaviour of the bentonite core

The main part of the seal structure is the expansive core composed by bentonite. The goal of this core is generate a strong swelling in order to recover a stress state similar to the initial one and to achieve a very low permeability arrangement. The design swelling pressure is 7 MPa.

Bentonite powder, compacted blocks and mixture of powder and pellets are being considered as potential buffer materials. A common feature of these materials is a double structure in which microporosity inside clay aggregates coexists with the macroporosity. The modelling approach could be based on the definition of different numerical models organized in a hierarchical manner.

With a simple structure approach is possible generate a progressive swelling upon hydration. A modified version of the elastic law of the Barcelona Basic Model (Alonso 1990) has been used. Equations 4 and 5 describe the dependence of the elastic parameters on the mean stress and suction. The different parameters were calibrated based on the design swelling pressure.

$$k_i = k_{i0} (1 + \alpha_{is} S) \quad (4)$$

$$k_s = k_{s0} (1 + \alpha_{sp} \ln P/P_r) \exp(\alpha_{ss} S) \quad (5)$$

To model features such as transient collapse of the macrostructure and the evolution of the macro-micro porosity requires a double structure modelling approach.

5. Simulation of the seal structure

The hydro-mechanical modelling of the seal structure was performed using the finite element code CODE-BRIGHT (DIT-UPC, 2002) and solving the field equations related to mass balance of solid and water and the balance of momentum:

$$\frac{\partial}{\partial t} (1 - \phi) \rho_s + \nabla \cdot (j^s) = f^s \quad (6)$$

$$\frac{\partial}{\partial t} (\theta_l^w S_l^w \phi + \theta_l^g S_l^g \phi) + \nabla \cdot (j_l^w + j_g^w) = f^w \quad (7)$$

$$\nabla \cdot \sigma + b = 0 \quad (8)$$

The modelling considers a bi-dimensional and axisymmetric geometry around the axis of the gallery. The model domain has a width of 60 m and a length of 100.5 m. The outside diameter of the gallery is 8.72 m and the lining is composed of a 0.7 m thick concrete support. Finally the sealing system includes a 40.5 m long swelling core (made of bentonite), two 5 m long concrete plugs and a fill of disaggregated and recompacted COx (considered as a non-expansive material) (Figures 1 and 5). With this approach, it is not possible to reproduce the anisotropy of the EDZ but the other features are retained in order to capture the short and long term response.

Considering an operational phase of 100 years, the water flow results from the rehydration process generated after seal installation. The lining and the concrete plugs should guarantee hydration under near constant volume similar to a laboratory swelling pressure test. This condition has been analysed in the numerical modelling of seal structure.

The stages of the modelling includes the excavation of the gallery, the installation of the lining six month later, 100 years of ventilation as an extreme case during the work time of the repository, the sealing system installation and finally the hydration process from the host rock until that the initial water pressure (4.85 MPa) is recovered.

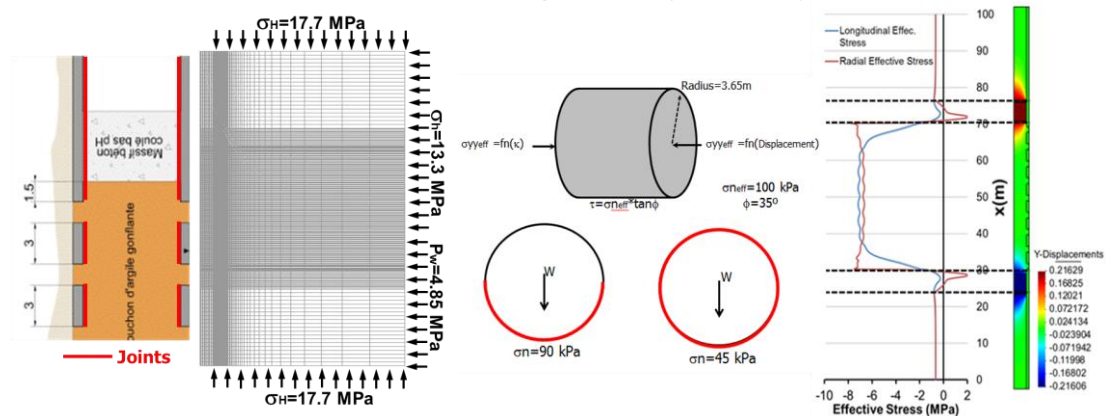


Figure 5. Model and mesh features (Left). Plugs stability (Right)

Artificial stress concentration appears close to at the contact between the concrete support plugs and the lining. This effect is due to the fact that the contact is considered non-sliding. A longitudinal displacement of the plugs (0.20 m) is computed and the longitudinal stresses vanish near the plugs. However, a central part of the core maintains the high swelling pressure and the radial pressure is constant along the gallery due to the lining (Figure 5).

The hydration process of the EDZ is affected by the conditions of all phases of the repository (Figure 6). The total saturation is reached at 1200 years and the initial water pressure (4.85 MPa) is recovered after 2500 years.

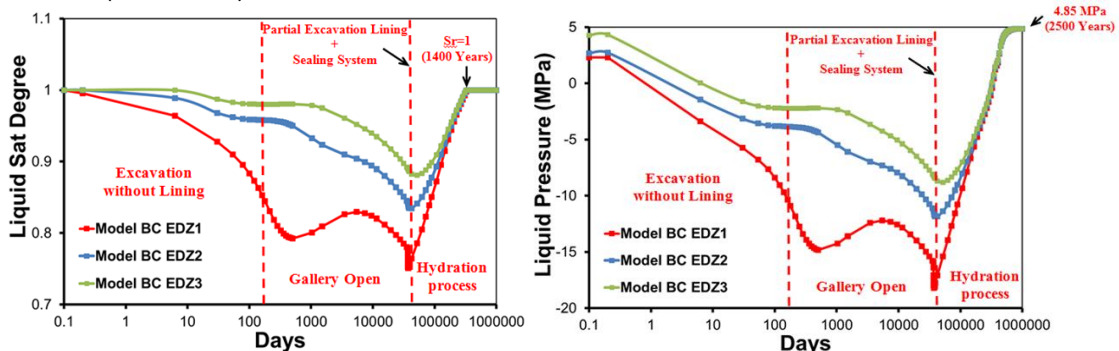


Figure 6. Hydraulic response of the Excavation Damage zone

The swelling pressure increases during the hydration processes according to the single structure approach until it reaches the design swelling pressure value. As indicated the Figure 7 the joint is closed at stresses lower than the final state of the bentonite core, because a low normal stiffness are expected. Finally the creep deformations generate a recompaction of the EDZ increasing the radial stress.

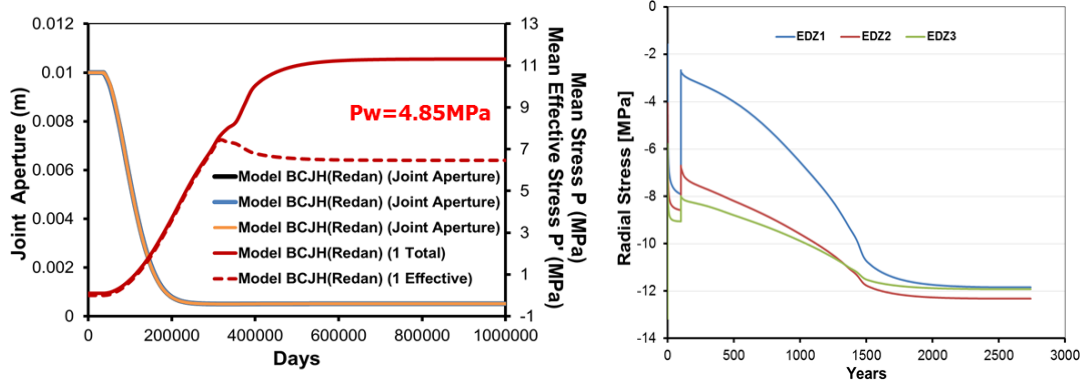


Figure 7. Swelling pressure of the bentonite and join aperture evolution (Left). Recompanction of the EDZ after seal instalation (Right).

6. Conclusions

The conception of the seal structure must guarantee a system with very low permeability and the recovery of the major part of the stress state around the excavation.

The behaviour of the seal structure is affected by all phases of the repository, including construction and the operational period. The excavation process and the ventilation of the galleries determine the initial state of the sealing.

It has been shown that, by incorporating in the analysis special features such modelling of short and long term behaviour of the host rock, contact effects and expansive behaviour of the bentonite core, a reasonable response of the system is obtained.

7. References

- Alonso, E.E. Gens, A. Josa, A. (1990). A constitutive model for partially saturated soils. *Géotechnique* 40, No. 3. 405-430.
- Andra (2012). Référentiel du comportement des formations sur le site de Meuse/Haute Marne. Report D.RP.AMFS.1 2.0024. Châtenay-Malabry: ANDRA.
- DIT-UPC (2002). CODE_BRIGHT, a 3-D program for Thermo-Hydro-Mechanical analysis in geological media: User'sguide, CIMNE, Barcelona.
- Gens, A. (2003). "The role of geotechnical engineering for nuclear utilisation". (Special Lecture). Proc. 13th Eur. Conf. Soil Mech. Geotech.Engng, Prague: IOS Press, p. 25–67
- Gens, A. (2011). On the HM behaviour of argillaceous hard soils-weak rocks. "Proc 15th Eur. Conf. Soil Mech. Geotech.Engng: geotechnics of hard soils, weak rocks". Atenes: IOS Press, p. 71-118.
- Mánica, M. A., Gens, A., Vaunat, J., & Ruiz, D.F. (2015). Anisotropic failure criterion for an argillaceous rock: formulation and application to an underground excavation case. XIII International Conference on Computational Plasticity (COMPLAS). E. Oñate, D.R.J. Owen, D. Peric and M. Chiumenti (Eds), 654-660.
- Zandarin, M. T. (2010). "Thermo-Hydro-Mechanical analysis of joints - A theoretical and experimental study". PhD Thesis. Universitat Politècnica de Catalunya (UPC).

A ROBUST NUMERICAL FRAMEWORK FOR REACTIVE TRANSPORT IN CEMENT PASTE

Fabien Georget (fabiang@princeton.edu), Jean H. Prévost
Princeton University, Princeton NJ, USA.

Bruno Huet
Lafarge Research Center, Saint-Quentin-Fallavier, France

Pierre Pimienta
CSTB, Champs-sur-Marne, France

ABSTRACT. Cement and concrete products play a major role in civil engineering for everyday building or major infrastructure (power plant, bridge, nuclear waste facilities ...). However they are very complex materials and their modelling present many physical and numerical challenges. The majority of the existing tools are targeted for reservoir and aquifer simulations and are ill-fitted for cementitious materials. We present a new reactive transport framework developed specifically for cement paste. Its main numerical feature is a strong sequential iterative coupling based on the residuals of the transport equations. Because it includes the constitutive equations in the main convergence loop, complex material models can be used. For example, the modeller can describe the impact of the different pore classes on the transport parameters. Also, a rigorous solution to the equilibrium phase assemblage problem allow us to solve problems with fronts efficiently. Through benchmarks and test cases we demonstrate the abilities of our framework.

1. ReactMiCP: the reactive transport solver

The reactive transport solver uses the operator splitting method. The advantages of this approach over global step algorithms are particularly compelling for the complex problems we want to simulate. Each operator is solved inside a separate stagger. Since they are insulated, the best methods and solvers can be chosen for each of them. Two staggers are usually defined. The transport stagger solves the transport equations, and the chemical stagger solves the mass conservation equations associated with the chemical reactions. We add another stagger, the upscaling stagger, which is often overlooked but very important in variable porosity problem. It is in charge of solving the constitutive equations. These equations upscale the chemistry solutions (pore scale) to the governing equations (REV scale) For example, it finds the macroscopic transport parameters given the current solid phase assemblage.

Two families of algorithms exist for operator splitting methods. Sequential Non-Iterative Algorithms (SNIA) do not check for convergence and solve each operator once per timestep. On the other hand Sequential Iterative Algorithms (SIA) iterates over the operators until a convergence criterion has been satisfied. The advantages of SIA are due to the error control. The better mass conservation improves the quality of the solution (e.g. the stability with respect to the timestep) and increases the maximum timestep allowed, thus decreasing the overall work.

An argument often presented against SIA is its complexity. However we propose a very simple and efficient way of implementing a SIA solver. Our implementation is based on the residuals of the governing equations. The governing equations are defined as the macroscopic mass conservation equations (i.e. the transport equations). For a component i in fluid phase α a governing equation can be written as:

$$\frac{\partial \phi S^\alpha C_i^\alpha}{\partial t} = -\nabla \cdot F_i^\alpha + \sum_B R_i^{\beta \rightarrow \alpha}$$

Where φ is the porosity, S^α the saturation of fluid phase α , C_i^α the total concentration of the component in the phase, F_i^α the total flux of component i in phase α and $R_i^{\beta \rightarrow \alpha}$ the chemistry exchange term from phase β to phase α .

The governing equations are solved inside the transport stagger using a predictor-multicorrector algorithm to implement the backward Euler method. The variables used are the rate of change of the main variables, e.g. the time derivatives of the saturation, the aqueous and solid total concentration, the partial pressure... For a main variable x , we solve for $\dot{x} = \frac{\partial x}{\partial t}$ and, $x_k = x_o + \Delta t \dot{x}_k$, where k is the iteration number. The chemistry exchange terms are computed inside the chemistry stagger.

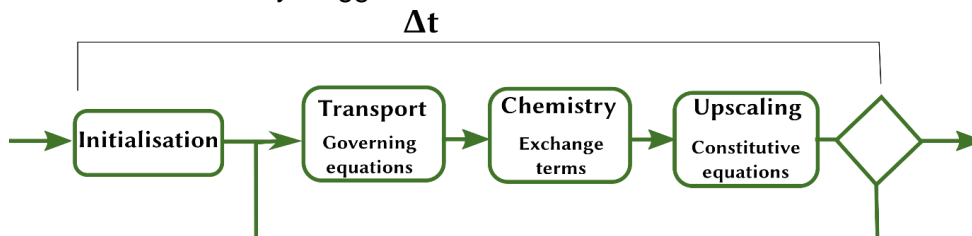


Figure 1: Main algorithm of the reactive transport solver

Figure 1 describe our algorithm. The first stage of a timestep concerns the initialization of each stagger. During this step, the predictor and velocity vector are initialized, as well as the chemistry rate and some macroscopic parameters in order to reduce the number of iterations. The initial residuals ($\|R_0\|$) are also computed during this step. They will be used to check the progress made during the iterations. Finally, any equations that need to be solved by the forward Euler method, if included by the modeller, can be solved during this step.

Inside a fixed-point iteration, the staggers are solved sequentially. They each update their own variables. At the end of an iteration, the global residuals are computed again using the transport stagger. If the system has converged, the next timestep can begin. Otherwise a new iteration is started. The definition of the criteria of convergence is crucial for the good behaviour of the solver. At least three values must be checked. The absolute and the relative norms of the residuals ($\|R_k\|$, $\|R_k\|/\|R_0\|$), and the update ($\|\dot{x}\|$). The variables taken into account in the update are the governing equations' variables but it should also contain purely chemical variables such as the volume fraction of mineral phases. The reason is that at equilibrium the aqueous solution can be at steady-state but the system is still evolving. Although the tolerances for each stagger should be quite restrictive to avoid any oscillations and reduce the number of fixed-point iterations, it has been observed that the global tolerances for the reactive transport solver can be relaxed.

Another important advantage of the iterative approach is the easy implementation of an adaptive timestep algorithm. Adaptive timestep is necessary to efficiently solve simulations since it allows to adapt the amount of work done to the amount of work actually needed by the system. The number of iterations are a good indication of how easy it is to solve the problem for a given timestep. A large number of iterations indicates a steep problem while a single iteration implies that the iterative scheme is superfluous. Thus the user can define an ideal range of iteration. An algorithm will then try to keep a moving average of the number of iterations inside this range. In practice, the range $[1, 15]$ has been observed to be a good choice in many cases. The moving average is necessary to smooth out any accident. The user must also define an admissible timestep range to constrain the algorithm since timesteps too small or too big lead to stability and convergence problems.

A failure in a stagger should not be critical for the reactive transport solver. Failures will happen on occasion and a robust solver should deal with them. In our algorithm, all the unique values are saved at the beginning of the timestep inside the predictors. Therefore they can be restored. In addition, the chemistry exchange terms and the updates are cleared. The transport parameters can also be reset by calling the upscaling stagger. A new timestep is then started using a smaller (or in rare cases a bigger) timestep. Although the system can

recover from such an error, it should be avoided if possible since the process is CPU intensive due to the coldstart. Adjusting the timestep or the convergence tolerances are possible methods to decrease the failure rate. However, in problems where dissolution/precipitation fronts are propagating such failures are relatively common when the front jump from one cell to the other.

The formulation described here is very generic and other governing equations such as the stress, poromechanical or energy conservation equations could also be added in the transport stagger.

2. DFPM: the finite element solver

To allow an efficient coupling and to increase the possibility of customization we implemented a new vertex centered finite element solver for the transport stagger. The algorithms used are the ones implemented with success in Dynaflow (Prévost (2010)). In addition to the predictor-multicorrector algorithm described in the previous section, an important process is the element by element formulation based on the residuals. Only the method to compute the residuals inside an element needs to be implemented. The Jacobian is computed using a finite difference scheme. It allows to treat automatically any sufficiently smooth non-linearities. It is important especially if a priori unknown user models are injected into the equations. An example of the numerical advantages of this method is shown in the section 6.

3. SpecMiCP: the speciation solver

A new speciation solver, SpecMiCP, was implemented to be used in the chemistry stagger (Georget et al. (2015)). It was designed to allow a very efficient coupling. SpecMiCP is available through an API (application programming interface) which makes its inclusion in a reactive transport solver very easy. It also uses intensive variables which makes it ill-fitted for batch simulations of experiments but allows automatic scaling in the reactive transport solver. Thus the convergence properties are mainly independent of the mesh size.

The main distinguishing feature of SpecMiCP is the formulation of the solid phase equilibrium assemblage as a complementarity problem. The problem is reformulated using a C function and solved with a custom semismooth Newton solver (Facchinei and Pang (2003)). This rigorous mathematical approach, compared to the traditional trial and error process, give us better convergence properties. These properties are not just theoretical but allow the solver to be 10-15x faster than PHREEQC on our example problems. One other very important consequence for reactive transport is that the basis of chemical components can stay the same throughout the computation. Hence it grants us the possibility to use only one basis shared among all the modules. It greatly simplify the coupling process and avoid any expensive basis switching.

4. MoMas reactive transport benchmark

Well-established benchmark are very useful in a scientific community because they give a true insight on the relative advantages and limitations of algorithms and software. To test our coupling method, we used the MoMas reactive transport benchmark (Carrayrou et al. (2010)), in particular we modelled the 1D “easy” test case.

The results of the advective case are displayed in figure 2. The results from ReactMiCP are compared with two other solvers based on operator splitting: HYTEC (SIA) and SPECY (SNIA). Since the error is not controlled, SPECY needs a very fine mesh and very small timesteps, and thus it cannot obtain a good solution in the allowed time specified by the benchmark. On the other side, HYTEC obtains a relatively good solution but is very slow compared to the other codes. In the middle ground, our software controls the error and is fast

so it obtains a good solution in a reasonable amount of time. The two orders of magnitudes difference in the CPU time between our solver and HYTEC is probably due to a more efficient coupling and the relative compactness of SpecMiCP compared to CHESH, the speciation solver of HYTEC. This demonstrate that specific code should be written to be used in a splitting operator algorithm. It still should be noted that although HYTEC is two orders of magnitude slower than ReactMiCP, it is still providing a better answer than the non-iterative software.

Although this benchmark does not test for very important features such as ionic strength, kinetics or solid phase assemblage, it is a good validation of our approach and coupling algorithms.

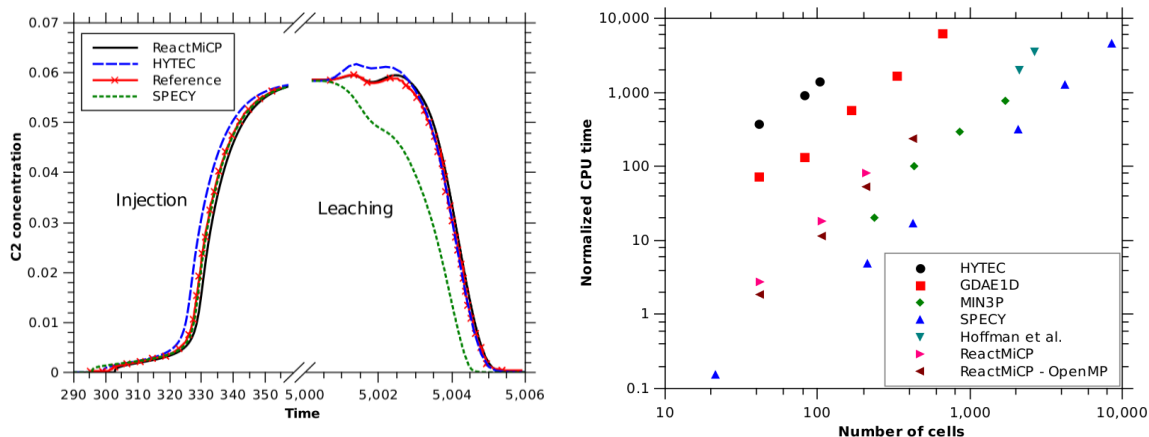


Figure 2: Advection case of the 1D easy test case of the MoMas reactive transport benchmark.

5. Leaching of cement paste in CO₂-rich brines

Our goal is to create a tool specialized for cement and concrete simulations. To test the completion of this objective we modelled the leaching of cement paste in CO₂-rich brines. The study investigated the impact of the boundary conditions (pH, [CO₂], [Ca²⁺]) and reproduced the experiments of Matteo (2011).

The problem is interesting to test the capacities of ReactMiCP since it is a highly-variable porosity problem. The phase assemblage change completely in a few cells and the porosity vary from 0.2 to 0.8. To further test the modelling abilities of our solver and try to better represents the physics of the material, we implemented a complex upscaling model for the prediction of the diffusion coefficient based on a multi-coated sphere assemblage. The model was inspired by the work of Bary and Béjaoui (2006).

Due to the inclusion of the upscaling stagger in the main convergence loop, our solver was able to solve the problem without difficulty. It simulates 30 days of leaching in 10 minutes to an hour. This computing efficiency is not only to shine in benchmarks, it allowed us to run many simulations which resulted in a better understanding of the underlying physics of the problem. Although no quantitative answer could be obtained due to the large number of uncertainties we were able to reproduce qualitatively the experiments. Figure 3 presents some results obtained. The left figure shows a profile obtained at the end of one of the simulation. A calcite peak can be observed, it marks a clear separation between the cement paste and an aluminosilicate layer. We found that it is fundamental to understand the properties of this calcite layer to predict the overall rate of reactions of the system. Depending on these properties, the system will behave differently as shown on the right plot of figure 3. At low pH and low CO₂, the system is governed by a thick layer of low Ca/Si C-S-H. By increasing the amount of carbonates in the system, we can clog the porosity by forming a dense layer of calcite. Adding more carbon dioxide in the system will decrease the pH at the calcite peak and foster its dissolution leading to higher reactivity. Being able to predict accurately the

transition between the different domains is critical for geological sequestration of CO₂, in order to ensure the integrity of the cement well-plugs.

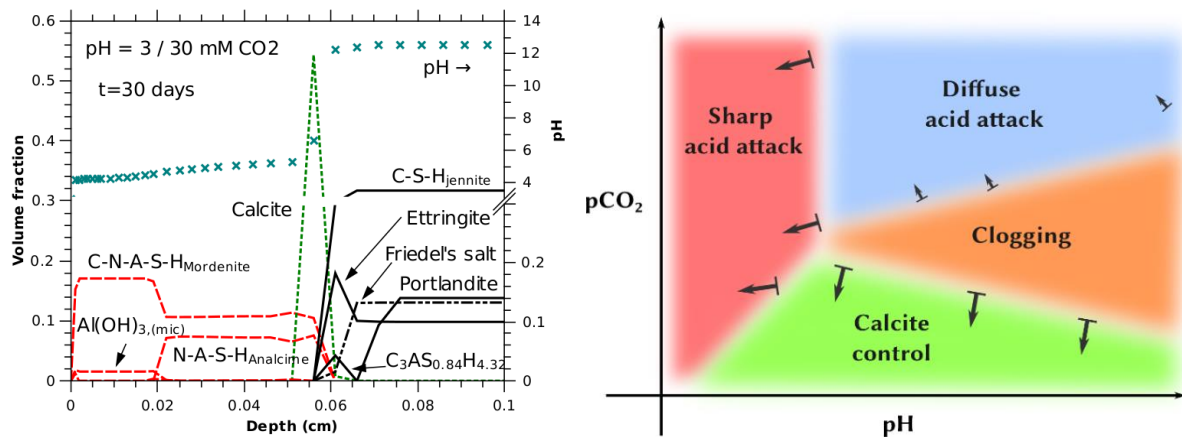


Figure 3: Leaching of cement paste in CO₂-rich brines. Left: pH and solid phases profiles obtained at pH=3, 30mM CO₂ after 30 days. Right: Separation of the main mechanisms observed in the experiments and the simulations. Arrows represent the gradient of reactivity (defined as the apparent diffusion coefficient of the portlandite dissolution front).

6. Drying in porous medium with large capillary pressure

The last example demonstrates our abilities to solve non-linear user model in the transport stagger. We solve the drying of a sample by considering 3 equations. The transport stagger solves for the transport of water in the liquid and the gas phase and in the chemistry stagger we solve the separation of water into the liquid and gas phase. In these equations, the partial pressure of water, the relative permeability and the capillary pressure are functions of the saturation given by the user. The functions and parameters used in these sections were extracted from Prommas et al. (2011).

More efficient methods exist to solve this problem but this is an excellent toy problem to demonstrate the features of our solver. The capillary pressure is high in cement paste and the capillary flow is one of the dominant mechanism. Therefore, our framework will only be useful if it can model it accurately, especially to couple physical phenomena such as hydration, drying and carbonation.

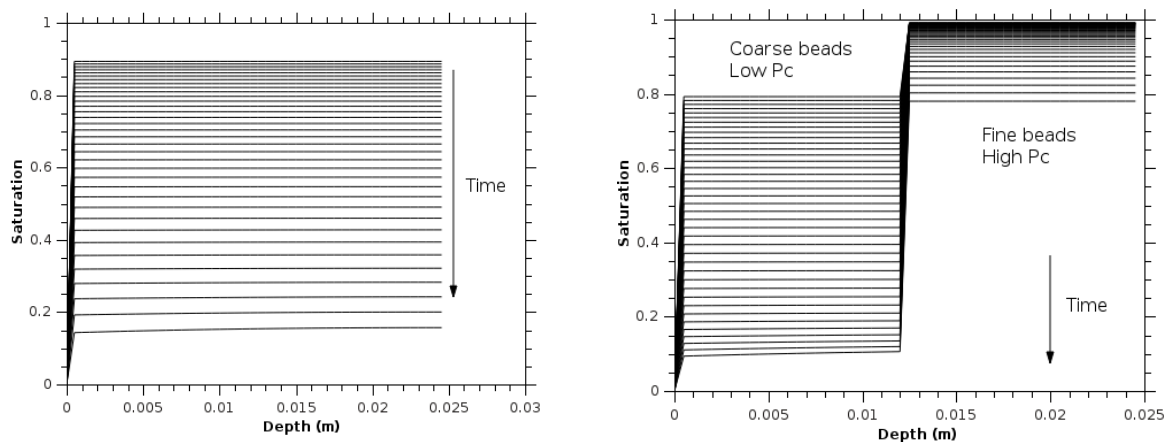


Figure 4: Drying of beads beds. Left: drying of fine beads, Right: drying of a layer of coarse beads on top of a layer of fine beads.

Figure 4 displays the results of the experiment. The left figure shows the result for the fine bed assemblage. Due to the high capillary pressure of the system, the saturation is almost constant in the sample and the medium dry homogeneously. The right figure presents the drying of an assemblage of coarse beads on top of fine beads. For a same saturation, the capillary pressure will be higher for the fine beads. At equilibrium, at the interface between the two materials the capillary pressure must be constant, thus the saturation in the smaller beads will be higher. The coarser beads on top will dry faster. This behaviour has been observed in experiments (Georget (2012)) and is well represented in the simulations.

7. Conclusions

Cement and concrete are complex materials (high P_c , multiscale pore size distribution, large number of solid phases ...) and thus require special tools for their modelling and simulation. The main takeaway of this study is that following rigorous mathematical methods is worthwhile since they are more flexible and robust. The sequential iterative method including all the equations, the complementarity conditions for solving the equilibrium phase assemblage or the finite difference Jacobian to take into account all non-linearities are examples of the more complex but more powerful methods we apply. A few illustrative examples are presented to demonstrate the features of the framework.

8. Acknowledgments

This work was supported by a grant from Lafarge and CSTB, Scientific and Technical Center for Building, to Princeton University. This support is most gratefully acknowledged.

9. References

- F. Georget. Experimental study and modelling of the drying of gypsum. Master's thesis, ESPCI Paristech, June 2012.
- F. Georget, J. H. Prévost, and R. J. Vanderbei. (2015) A speciation solver for cement paste modeling and the semismooth Newton method. *Cement and Concrete Research*, 68(0):139–147.
- F. Georget, J. H. Prévost, and B. Huet. Validation of a reactive transport solver based on a semismooth speciation solver. *Computational Geosciences*. (Submitted to).
- F. Georget, J. H. Prévost, and B. Huet. Reactive transport modelling of cement paste leaching in brines. (In preparation).
- F. Georget SpecMiCP <https://bitbucket.org/specmicp/specmicp>
- B. Bary and S. Béjaoui. (2006) Assessment of diffusive and mechanical properties of hardened cement pastes using a multi-coated sphere assemblage model. *Cement and Concrete Research*, 36(2):245–258.
- J. Carrayrou, J. Hoffmann, P. Knabner, S. Kräutle, C. de Dieuleveult, J. Erhel, J. V. der Lee, V. Lagneau, K. Mayer, and K. MacQuarrie. (2010) Comparison of numerical methods for simulating strongly nonlinear and heterogeneous reactive transport problems---the MoMaS benchmark case. *Computational Geosciences*, 14(3):483--502.
- F. Facchinei and J.-S. Pang. Finite-dimensional variational inequalities and complementarity problems. Springer, New York, 2003.
- J. H. Prévost. Dynaflow: A nonlinear transient finite element analysis program. User Manual. Princeton, NJ, 2010.
- R. Prommas, P. Keangin, and P. Rattanadecho. (2010) Energy and exergy analyses in convective drying process of multi-layered porous packed bed. *International Communications in Heat and Mass Transfer*, 37(8):1106–1114.

THE ROLE OF RHEOLOGY AND PORE WATER PRESSURE DURING THE MODELLING OF LANDSLIDES PROPAGATION WITH SPH

P. Dutto (paola.dutto@bam.de),
Bundesanstalt für Materialforschung und -prüfung (BAM), Berlin, Germany.

M. M. Stickle,
Universidad Politécnica de Madrid, Madrid, Spain.

M. Pastor,
Universidad Politécnica de Madrid, Madrid, Spain.

ABSTRACT. Landslides can cause major economic damage and a large number of casualties. Here a model that combines a depth integrated description of the soil-pore fluid mixture together with a set of 1D models dealing with pore pressure evolution within the soil mass is presented. The mathematical model is based on the Biot-Zienkiewicz equations. Concerning the material behaviour, the approach used is the Perzyna viscoplasticity. A simple shear rheological model is derived, providing the basal friction needed in depth integrated models. Then, the chosen numerical technique, the Smoothed Particle Hydrodynamics (SPH), has been enriched by adding a 1D finite differences grid associated at each node in order to improve the description of pore water profiles in the avalanching soil. This model has been then applied to simulate the propagation phase of the Aberfan flowslide occurred in 1966.

1. Introduction

Flowslides are rapid flows, either saturated or unsaturated, where the material has a high compaction tendency, a low density and it is characterized by a metastable structure. The prediction of the propagation of these kind of hazards would suppose the achievement of great human and economic benefits, due to the fact that their effects are often catastrophic and devastating.

In order to make such a prediction, a depth integrated mathematical model described in Pastor et al. (Pastor et al. 2013) and a rheological approach based on Perzyna viscoplasticity (Perzyna 1966) are taken into consideration. Concerning the numerical technique, the Smoothed Particle Hydrodynamics (SPH) (Lucy 1977; Monaghan & Lattanzio 1985; Gingold & Monaghan 1977; Benz 1990; Liu & Liu 2010) is used, which has been enriched with a set of one dimensional finite differences grid associated to each SPH node in order to improve the description of the pore water pressures along the height of the flowslide.

The final goal of the study has been to apply the SPH depth integrated numerical model to simulate the propagation phase together with the path, velocity, depth and pore pressure profiles of Aberfan flowslide occurred in 1966.

2. Mathematical model

The mathematical model is based on the model developed at Swansea University (Zienkiewicz et al. 1980) and cast in terms of velocity and pore water pressure.

The equations have been depth integrated (Pastor et al. 2013) and resulting to be:

$$\frac{\bar{D}h}{Dt} + \frac{\partial \bar{v}_i}{\partial x_i} h = e_R \quad (1)$$

$$h \frac{D \bar{v}_i}{Dt} - \frac{\partial}{\partial x_j} b_3 \frac{h^2}{2} \delta_{ij} = -\bar{v}_i e_R + b_i h + \frac{1}{\rho} \frac{\partial}{\partial x_j} h \bar{\sigma}_{ij}^* - \alpha \frac{\partial}{\partial x_j} (h \bar{v}_i \bar{v}_j) + \frac{1}{\rho} \left| N^B \right| t_i^B \quad (2)$$

$$\frac{dp_w}{dt} = \rho g \frac{dh}{dt} \left(1 - \frac{x_3}{h} \right) + \frac{K_v}{\alpha} \delta_v - \frac{K_v}{\alpha} k_w \frac{\partial^2 p_w}{\partial x_3^2} \quad (3)$$

where e_R is the erosion rate, h is the depth of the flow, \bar{v}_i is the i -th component of the velocity of the soil skeleton, $\bar{\sigma}_{ij}^*$ is the effective stress tensor, t_i^B is the i -th component of the surface stress acting on the basal surface, $\left| N^B \right|$ is the normal vector to the basal surface, p_w is the pore pressure, δ_v is the rate of deformation tensor, k_w is the permeability, K_v is a suitable stiffness module and α is a general coefficient. Equation (1) and (2) represent the balance of mass and momentum respectively and are discretised with the SPH technique. Equation (3) represents the evolution of the pore pressure along the height of the landslide and is discretised with a 1D finite differences grid associated to each SPH node.

3. A new simple rheological law based on Perzyna viscoplasticity

In order to complete the mathematical model described above, a suitable constitutive or rheological law is much needed. Here, a new simple rheological model for frictional material based on Perzyna viscoplasticity is presented. It aims to close the gap between solid mechanics model used for landslides' triggering and rheological model normally used for the propagation phase.

Perzyna viscoplasticity model describes the evolution of the viscoplastic strain rate by means of an over-stress function. By choosing as over-stress function three different yield criteria (Mohr-Coulomb, Von Mises and Cam Clay), it has been showed (Pastor et al. 2013) that Perzyna viscoplasticity gives similar results, in terms of velocity profiles, than those obtained with classical rheological laws (Newtonian or Bingham model).

Moreover, the hypothesis of the infinite landslide model are assumed in order to overcome the loss of information along the vertical due to the depth integration of the mathematical model.

Finally, the expression that defines the basal friction is found as:

$$\tau_b = s_b \left[\left(\frac{\bar{v} \sqrt{2} \mu}{h} \right)^{\frac{1}{N}} + 1 \right] \quad (4)$$

where $s_b = \sigma_{3b} \tan \varphi$ is the basal shear strength.

4. Application of the model to Aberfan 1966 flowslide

Introduction

Aberfan is today a former coalmining village in South Wales (UK). In 1966 a flowslide of coal waste occurred, propagating onto the village itself and provoking 144 fatalities. Information about the failure mechanisms and material properties are provided in (Bishop, A. W., Hutchinson, J. N., Penman, A. D. M. & Evans 1969) while other raw information are available at the UK National Archive.

The Aberfan colliery waste was tipped on the side of a hill (Tip 7) facing the village. The triggering mechanisms of the flowslide lay in the hydrogeology of the site. Due to heavy rain, in fact, artesian pore pressure rose up in the sandstone beneath the less permeable glacial deposit at the toe of the slope and caused the hazard. In table 1 the characteristics of the Aberfan flowslide are reported.

Table 1. Aberfan flowslide characteristics.

<u>Concept</u>	<u>Value</u>	<u>Description</u>
Height	67 m	Height of the tip measured from the toe
Slope	12 degrees	Slope of the underlying terrain
Distance	275 m	Distance before division in two lobes
Total distance	600 m	Total distance travelled
Velocity	4,5 - 9 m/s	Estimated velocity

Numerical simulation

In order to simulate the Aberfan flowslide, the topographic mesh and the SPH nodes representing the initial mass are needed. Authors have built both of them by using the topographic information and maps available at the UK National Archive. They are show in figure 1.

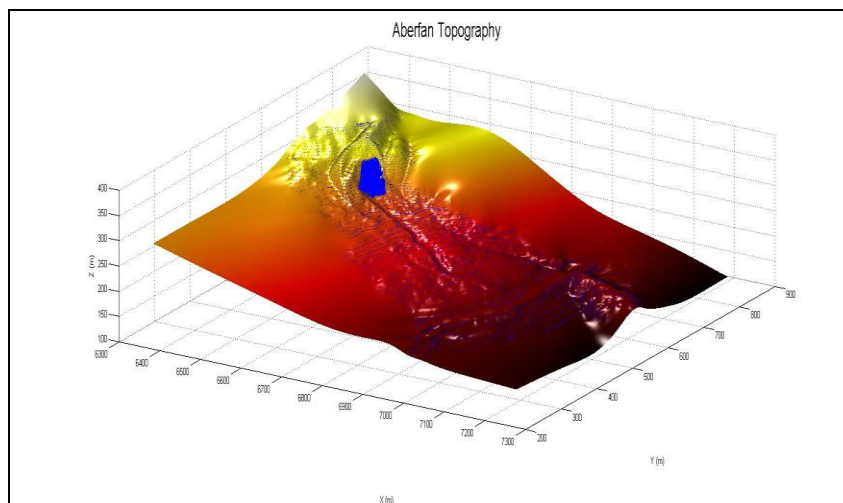


Figure 1. Sliding portion of the Aberfan flowslide (in blue) and the topography used for the simulation.

In table 2, the parameters used to model the Aberfan flowslide which give the best agreement with field observation are presented.

Table 2. Parameters of the numerical simulation.

Parameter	Value	Description
$\tan \phi'$	0.726	Tangent of the friction angle
N	1	Rheological law parameter
γ	0.001 s	Viscosity
ρ	$1740 \frac{Kg}{m^3}$	Total distance travelled
eR	65.E-4	Erosion coefficient
Cv	65.E-5	Consolidation coefficient
p_w^{rel}	0.8	Initial pore pressure
h_h^{rel}	0.4	Initial height of the basal saturated layer

Erosion has been taken into account through the erosion coefficient of the Hungr erosion law (Hungr 1995). In fact, with a careful reading of the report written by Bishop et al. (Bishop, A. W., Hutchinson, J. N., Penman, A. D. M. & Evans 1969), erosion is widely mentioned. Moreover, p_w^{rel} represents the initial pore water pressure at the basal surface, varying between 0 and 1; 1 corresponding to liquefaction. Finally, the relative height of the basal saturated layer h_h^{rel} was assumed to be 0.4 times the total height of the flowslide at the beginning.

Results and discussion

The results of simulation are shown in figure 2.

The height of the soil is showed at time 0, 10, 20 30, 45 and 55 s and it is satisfactorily reproduced by the model. It is possible to note that the final height of the soil of the left lobe at 50 seconds is almost 10 meters which match with the real height that hit the school building of Aberfan village.

Furthermore, the simulation reproduces well the division of the flowslide in to two lobes.

Results of the soil height also well matched with the one dimensional results obtained by Pastor et al (Pastor et al. 2013; Pastor et al. 2014).

In figure 2, on the right, the pore pressure contours evolution is presented at 0, 2, 5 and 10 s.

Please note that, in order to improve readability, the saturated layer has been expanded and now it occupies the whole mass. This is possible because we are considering the depth of the basal saturated layer proportional to the one of the landslide.

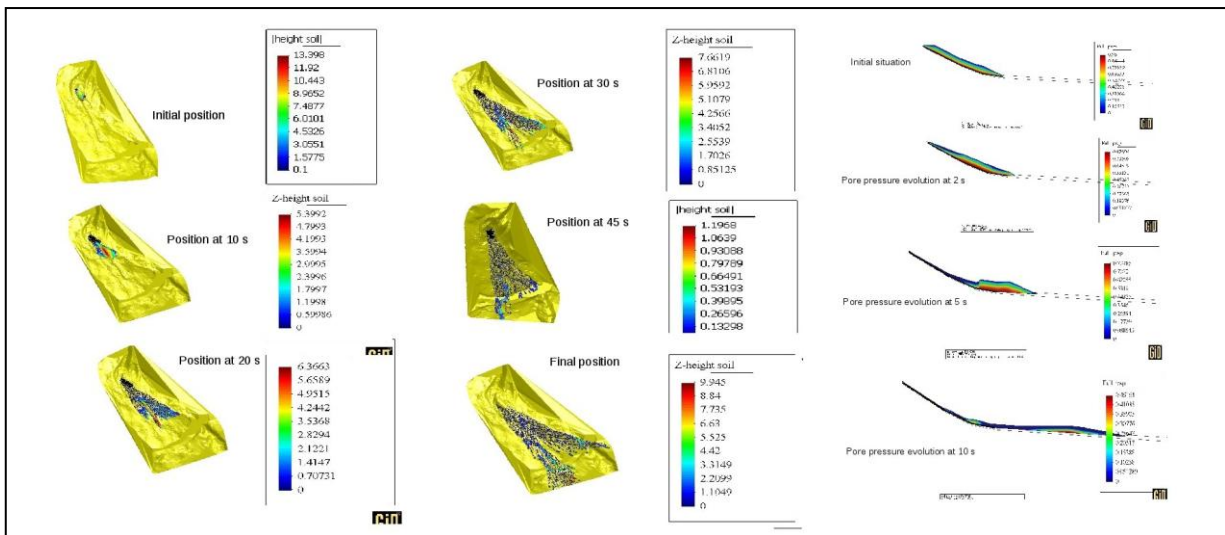


Figure 2. Results sequence of Aberfan flowslide simulation at 0, 10, 20, 30, 45 and 50 s and, on the right, Pore pressure contours evolution at 0, 2, 5 and 10 s.

5. Conclusions

It has been presented here a framework which has been applied to successfully model the case of the Aberfan flowslide occurred in 1966.

The mathematical model is based on the v-pw Biot- Ziekiewicz model (Zienkiewicz et al. 1980), for propagation and consolidation of avalanches, debris flow and fast landslide problems.

Then, the numerical model combines a SPH model for landslide propagation and a set of Finite Difference meshes associated to each of the SPH nodes where the pore pressure evolution is solved (Pastor et al. 2013).

Concerning the constitutive model, Perzyna viscoplasticity (Perzyna 1966) has been taken as a base model for a new rheological model for frictional materials, presenting the advantage of being close to some rheological models of interest.

6. References

- Benz, W., 1990. Smooth Particle Hydrodynamics - a Review. In *Proceedings of the NATO Advanced Research Workshop on The Numerical Modelling of Nonlinear Stellar Pulsations Problems and Prospects*. p. 269.
- Bishop, A. W., Hutchinson, J. N., Penman, A. D. M. & Evans, H.E., 1969. *Geotechnical investigations into the causes and circumstances of the disaster of 21st October 1966. In A selection of technical reports submitted to the Aberfan Tribunal.*
- Gingold, R.A. & Monaghan, J.J., 1977. Smoothed Particle Hydrodynamics - Theory and Application to Non-Spherical Stars. *Monthly Notices of the Royal Astronomical Society*, pp.375–389.
- Hungr, O., 1995. A model for the runout analysis of rapid slides, debris flows and avalanches. *Canadian Geotechnical Journal*, 32, pp.610–623.

- Liu, M.B. & Liu, G.R., 2010. Smoothed Particle Hydrodynamics (SPH): an Overview and Recent Developments. *Archives of Computational Methods in Engineering*, 17(1), pp.25–76.
- Lucy, L.B., 1977. A numerical approach to the testing of the fission hypothesis. *The Astronomical Journal*, 82, p.1013.
- Monaghan, J.J. & Lattanzio, J.C., 1985. A Refined Particle Method for Astrophysical Problems. *Astronomy and astrophysics*, 149(1), pp.135–143.
- Pastor, M. et al., 2013. A viscoplastic approach to the behaviour of fluidized geomaterials with application to fast landslides. *Continuum Mechanics and Thermodynamics*.
- Pastor, M. et al., 2014. Depth Averaged Models for Fast Landslide Propagation: Mathematical, Rheological and Numerical Aspects. *Archives of Computational Methods in Engineering*.
- Perzyna, P., 1966. Fundamental problems in viscoplasticity. *Advances in applied mechanics*, 9, pp.243–377.
- Zienkiewicz, O.C., Chang, C.T. & Bettess, P., 1980. Drained, undrained, consolidating and dynamic behaviour assumptions in soils. *Géotechnique*, 30(4), pp.385–395.

Experimental geomechanics and modelling

COMPARISON OF EXPERIMENTALLY DETERMINED AND THEORETICALLY PREDICTED ELASTIC PROPERTIES OF VTI SHALE UNDER UNIAXIAL LOADING

V. Sviridov (marvel@zedat.fu-berlin.de), S. Mayr, S. Shapiro
Freie Universitaet Berlin, Department of Earth Sciences, Berlin, Germany.

ABSTRACT. Stress conditions have a significant influence on the seismic properties and on the anisotropy in sedimentary rocks and especially shale. Understanding of such mechanisms plays an important role in 4D monitoring and sonic logs interpretation. This study presents the interpretation of the ultrasonic wave velocities measurements in vertical transverse isotropic (VTI) shale under anisotropic uniaxial stress conditions. In order to reconstruct the all independent elastic constants we measured 5 different velocities (full set). A significant velocity change is observed only parallel to loading direction, indicating the closure of aligned thin cracks (i.e. compliant pore space). The Thomsen anisotropy parameters epsilon and gamma show nonlinear decrease up to 20% by loading up to 30 MPa. Based on the determined full set of velocities we calculated the compliance tensor with axial stress for the application of the porosity deformation approach (Ciz and Shapiro, 2009) on the data. The model theoretically describes the observed stress dependency of elastic compliances of anisotropic media under uniaxial stress conditions. Furthermore we show that the influence of the stiff porosity deformation is negligible in comparison to the influence of the compliant pore space deformation.

Introduction

Stress conditions have a significant influence on the seismic properties and especially on the anisotropy in sedimentary rocks. Understanding of such mechanisms plays an important role in 4D monitoring and quantitative interpretation of seismic data. The investigation of shale elastic properties and their change with stress is the essential part of understanding 4D processes.

This study investigates a full set of ultrasonic wave velocities in shale under anisotropic uniaxial stress conditions. We apply the porosity deformation approach Ciz and Shapiro (2009) on the data and present the comparison of theoretically predicted elastic compliances of anisotropic media with measured ones.

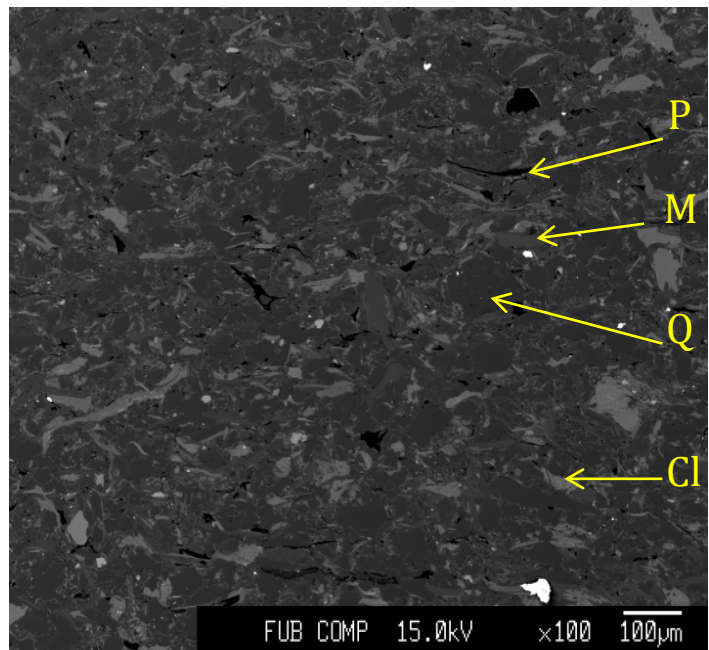


Figure 1. The sample mineralogy. P – pore space (black); M - Mica (medium grey); Q - Quartz (dark grey); Cl - Chlorite (light grey). A predominantly horizontal oriented alignment of P, M, Cl is observed.

Sample description

The investigated sample BaZ is cut perpendicular to the bedding and thus has a so called vertical transversely isotropic (VTI) symmetry, which is characterized by the vertical symmetry axis being parallel to the x_3 axis - usually the direction of the gravity forces. The specimen BaZ is extracted from the depth of 3777 meters (Upper Carboniferous) and is a sandy diagenetically consolidated argillite with dominant quartz content (see Figure 1).

The pore space and the grains have a linearly oriented preferred direction. The grain size is 100-150 μm and the dominant minerals are quartz (~50%), chlorite, mica, with admixtures of rutile and zircon. Room-humidity density of the sample was determined by water-saturation method and is equal to 2690 kg/m^3 . The connected porosity is about 2.8%.

Experimental methodology

The full set of elastic constants of the rock was determined by pulse transmission technique in ultrasonic frequency range 0.4–1 MHz, e.g., Mayr and Burkhardt (2006). The five required elastic wave velocities were measured in the following directions: P and S velocities in axial direction; P and S_h (polarized in bedding plane) velocities in radial direction and P_{incl} velocity measured under an inclination angle $\theta = 26^\circ$ to the bedding plane, see Figure 2. Correspondingly to the study of Dellinger und Vernik (1994) we consider the first arrival of P_{incl} wave as phase velocity. We estimated the errors to be 0.5% for P wave and 1% for P_{incl} and S waves. The measurements were performed under uniaxial stress conditions $\sigma_3 \neq 0$; $\sigma_1 = \sigma_2 = 0$ and ambient humidity of the sample. The uniaxial stress $\sigma_3 \neq 0$ applied along the symmetry axis in a TI sample will not produce additional symmetry planes, e.g. Mayr et al. (2014). The strain of the sample was measured by 4 strain gages.

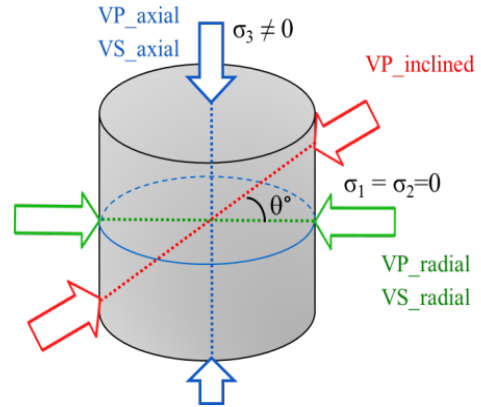


Figure 2. Experimental setup. The arrows and dotted lines indicate the directions of ultrasonic measurements. The sample has VTI symmetry, the bedding plane is horizontal.

Theoretical background

We used the anisotropic porosity deformation approach (originally: piezosensitivity theory) data analysis. The theory assumes an orthorhombic elastic medium with a pore space, which is separated into compliant and stiff porosity. The theory states that changes of elastic parameters under the pressure exponentially depend on the deformation of the compliant porosity and linearly on the deformation of the stiff porosity. The porosity deformation approach is able to predict any elastic parameter behaviour under stress. In case of uniaxial load, when the principal stress $\sigma_3 \neq 0$, the principal stresses $\sigma_1 = \sigma_2 = 0$ and the compressive stress is assumed to be positive (see Figure 2), the compliances tensor \underline{S} can be calculated with following equations, which we derive from general orthorhombic piezosensitivity theory Shapiro and Kaselow (2005); Ciz, and Shapiro, (2009):

$$S_{11}^{dr} = S_{11}^{drs} + D_{111} \quad (1)$$

$$S_{33}^{dr} = S_{11}^{drs} + K \cdot \sigma_3 + D_{333} \cdot e^{-F_3 \cdot \sigma_3} \quad (2)$$

$$S_{44}^{dr} = S_{44}^{drs} + K \cdot \sigma_3 + D_{144} + D_{244} + D_{344} \cdot e^{-F_3 \cdot \sigma_3} \quad (3)$$

$$S_{66}^{dr} = S_{66}^{drs} + 2 \cdot D_{111} \quad (4)$$

$$S_{13}^{dr} = const \quad (5)$$

where,

$S_{11}^{dr} = S_{22}^{dr}$, S_{33}^{dr} , $S_{44}^{dr} = S_{55}^{dr}$, S_{66}^{dr} , S_{13}^{dr} - are the five independent compliances of the drained rock, calculated using the full set of velocities measurements;

S_{ik}^{drs} – are theoretical compliances of the rock in a reference state (“Swiss cheese model”), when the compliant porosity is completely closed and stiff porosity corresponds to unloaded state;

K – is a coefficient of linear function of the stress, it is related to the stiff pore space deformation;

D_{NMM} – is a coefficient of exponential function of the stress;

F_1 – an exponent in the stress exponential; σ_1 a principal component of the stress;

D_{NMM} and F_1 are related to the compliant pore space deformation.

Measurement results

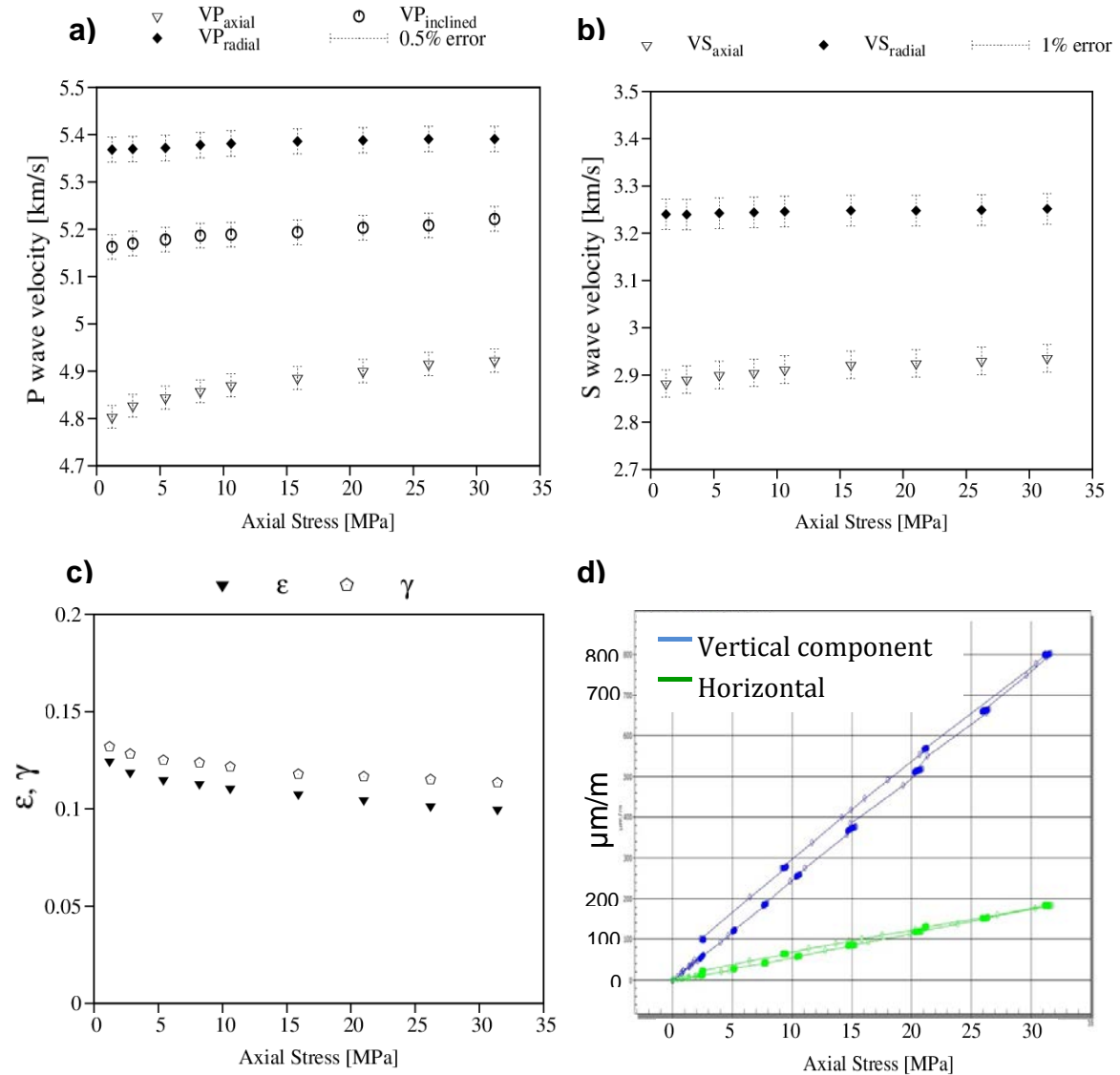


Figure 3. Room dry BaZ-VTI sample: (a) P wave velocity in axial, radial and inclined directions vs stress. (b) Sh wave velocity in axial (polarized out of bedding plane) and radial (polarized in bedding plane) directions vs stress. (c) Anisotropy parameters ϵ and γ vs stress. (d) Strain vs stress, loading and unloading cycles.

The effect of sample shortening, measured by strain gages, is about 0.08% in axial direction and expansion about 0.02% in radial direction, see Figure 3d, which corresponds to an apparent Poisson ratio of 0.25. The corresponding velocity overestimation will be in the

worst case about 0.07% and therefore lies within the error bars. Strain measurements show a hysteresis effect by loading and unloading cycles, which is an indication of the inelastic deformation. The curve of dependence of the strain versus the stress has a nearly linear form. The velocity changes with stress show the following trends: in loading direction a significant nonlinear increase of both velocities P and S_h can be measured, see Figure 3a, 3b. Perpendicular to the loading direction P and S_h velocity change is negligible – within the error bars; P_{incl} shows a small velocity increase. The anisotropy parameters, (Thomsen 1986) ϵ and γ systematically decrease with stress, see Figure 3c, while η and δ show fluctuations around a constant value.

Application of the theory on experimentally obtained data

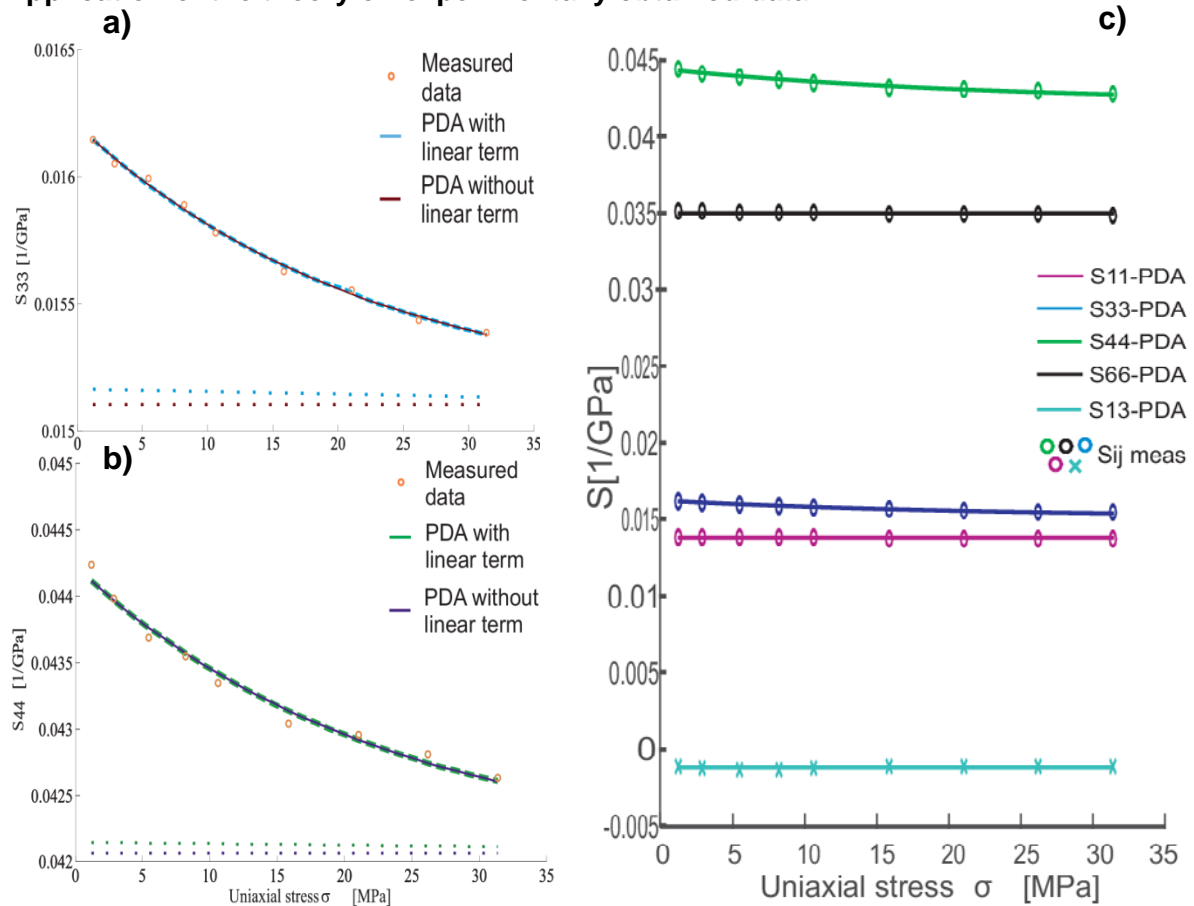


Figure 4. Room dry BaZ-VTI sample: (a, b) S_{33} and S_{44} compliances measured and predicted values. (c) Full set of measured and predicted compliances. For the predictions is used porosity deformation approach (PDA). The circles represent measured data, the solid lines represent theoretically predicted compliances without linear term and the dashed lines represent theoretically predicted compliances with linear term. The dotted lines indicate the compliance of rock in the reference state, when the whole compliant pore space is closed.

The theory was applied on the measured full data set for considered VTI sample. Two possible variations of the theory were examined. The first one takes into account the deformation of compliant pore space plus the deformation of the stiff porosity. The modelling was done using equations 1-4, including all terms, see Figure 4a, 4b dashed lines. In the second variation the influence of the stiff porosity deformation is excluded, hence the modelling was done in correspondence with equations 1-4, but without term K,

see Figure 4a, 4b solid lines. Figure 4 demonstrates that the difference between both solutions, with and without influence of stiff porosity, is negligible. According to the theoretical predictions significant change of compliances is observed only for two parameters, for S_{33} and S_{44} , while S_{13} , S_{11} and S_{66} fluctuate around constant values, see Figure 4c.

Interpretation and discussion

During the measurements the following effects are observed:

- o velocity change is only significant in loading direction;
- o the shape of velocity change is nonlinear;
- o the hysteresis effect;
- o the decrease of anisotropy parameters ε and γ , while η and δ show fluctuations around a constant value.

These effects can be explained by orientation of the loading direction with respect to the symmetry plane and therefore by the closure of thin cracks, which is partly irreversible. This compliant porosity, which is the most sensible to the stress, e.g. Mayr et al. (2014) is oriented parallel to the bedding and perpendicular to the uniaxial stress σ_3 (see Figure 1, 2). It means that the area of stress influence - the surface of the inner pore space is maximal in axial direction. Concurrently the axial direction is the most sensible to the stress and the only loaded direction. It explains the orientation of observed effects and the nonlinear dependency of elastic parameters. The relatively small applied stresses (up to 32 MPa) explain the absence of significant stiff porosity deformations.

After the application of PDA we conclude that the stiff porosity deformation in low stresses area does not significantly influenced the elastic parameters of the rock, see Figure 4. It is possible to reduce the number of independent parameters by modelling, namely to exclude the linear term K responsible for stiff pore space deformation (see equations 1-4).

The significant change of compliances is observed only for two parameters: for S_{33} and S_{44} , see Figure 4c, while S_{11} and S_{66} have nearly constant values. The curve of decrease of compliances versus stress has a nonlinear shape and is well predicted with an exponential function. It can be explained by orientation of stress conditions to the symmetry of the sample. The parameter S_{13} does not change significantly, which is in agreement with the theory.

The interesting feature is that the dependence of S_{33} versus stress and S_{44} versus stress have a similar shape. From the physical point of view both parameters are controlled by the same process of pore space deformation in the loading direction. From the analytical point of view they both are controlled by the same exponent F_3 in the stress exponential and therefore the shape is similar. This again leads to a reduction of the number of independent parameters by modelling.

Conclusions

The acquired full data set of elastic constants of vertical transverse isotropic sample under uniaxial stress conditions and the application of the theory reveal the following mechanisms of anisotropic elastic behaviour:

- a) the orientation of the stress to the layering, i.e. to the alignment of the compliant pore space, plays a crucial role for the change of anisotropy parameters;
- b) the elastic parameters of the rock in the low stress area are controlled by the compliant pore space deformation, whereas the influence of the stiff porosity is negligible;
- c) the dependence of the changed elastic parameters versus stress has a nonlinear form and is well described with an exponential function, which is predicted by the porosity deformation approach.

Acknowledgments

The research was carried out in the frame of the DGMK-project 741. We thank the companies EMPG (Hannover), GDF SUEZ (Lingen), DEA Deutsche Erdoel AG and Wintershall Holding GmbH (Kassel) for financing the project and the authorization to present the results.

References

- Ciz, R., and Shapiro, S. A. (2009). Stress-dependent anisotropy in transversely isotropic rocks: Comparison between theory and laboratory experiment on shale. *Geophysics*, vol. 74, no. 1.
- Dellinger, J., and Vernik, L. (1994). Do traveltimes in pulse-transmission experiments yield anisotropic group or phase velocities? *Geophysics*, vol.59, no. 11 (November 1994); P. 1774-1779.
- Mayr S.I and Burkhardt H (2006). Ultrasonic Properties of Sedimentary Rocks: Effect of Pressure, Saturation, Frequency and Microcracks. *Geophys. J. Int.* 164, 246–258.
- Mayr, S., Sviridov, V., and Shapiro, S. (2014a). Analysis of p- and s-wave velocities in a transversal isotropic sandstone and a shale under uniaxial loading conditions. In DGMK/ÖGEW Frühjahrstagung 2014, Fachbereich Aufsuchung und Gewinnung Celle, 24./25. April 2014, pages 1–9.
- Shapiro, S. Elastic piezosensitivity of porous and fractured rocks. *Geophysics*, vol. 74, no. 1, 2003.
- Shapiro, S. and Kaselow, A. (2005). Porosity and elastic anisotropy of rocks under tectonic stress and pore-pressure changes. *Geophysics*, 70(5):N27-N38.
- Thomsen, L. (1986). Weak elastic anisotropy. *Geophysics*. Vol.51, No 10.Conclusions

EXPERIMENTAL AND MODELLING STUDY OF CONCRETE DELAYED STRAIN IN A NUCLEAR CONTAINMENT BUILDING

AdrienHilaire (adrien.hilaire@epfl.ch),
LMC-EPFL, Lausanne, Switzerland

FaridBenboudjema, AvelineDarquennes, Georges Nahas
LMT-ENS Cachan, Cachan, France

ABSTRACT. The behaviour of a containment building in a nuclear plant is studied. A model was developed to simulate the behaviour of this massive prestressed structure from its casting to the end of its serviceability. This model is able to predict the risk of cracking at early age and the loss of prestress at long term. All phenomena affecting delayed behaviour of concrete are considered: hydration, heat and moisture diffusion, autogenous, drying and thermal shrinkage, basic and drying creep and cracking. In tandem with this work, experimental tests have been realised. Parameters are identified from their results. The delayed behaviour of the structure is calculated, the results are compared with in-situ measurements. Results highlight the importance of the creep modelling.

1. Introduction

Concrete containment of the nuclear power plants is the last barrier to nuclear release. These structures are designed to have a long lifespan (40 years for now, with a possible extension up to 60 years which is under evaluation). The gas-proofing of this kind of structures is based on the low conductivity of concrete (10^{-11} m/s for a standard concrete). However, this property is only ensured if the material is not too much damaged. Therefore, the internal safety enclosure is bi-axially prestressed in order to protect concrete from cracking during an accidental loading. The ageing of the structure may have two main consequences. Firstly, the prestress has to remain sufficiently high to counterbalance the tensile stresses caused by the accident. Secondly, cracking induced by non-accidental loads has to be limited: cracks may increase the kinetics of the transfers of aggressive agents and the durability may be reduced by an acceleration of the degradation phenomena like corrosion.

The lifespan of this structure is broken down into two distinguished periods: the early age and the long term phases. The modelling of the early age stage is firstly detailed through the presentation of a thermo-chemo-mechanical (TCM) model for concrete. Then the long-term phase is studied; mechanics of unsaturated porous media is used to consider couplings between creep, shrinkage and damage. In tandem with this work, experimental tests have been realised. Parameters are identified from their results. The delayed behaviour of this structure is calculated from its casting until the end of its serviceability, the results are compared with in-situ measurements. Results highlight the value of this kind of approach.

2. Thermo-Chemo-Mechanical modelling of concrete at early age

During the casting process of massive concrete structures, heat is released by the cement hydrations reactions and may lead to large temperature gradients and time variations of temperature in the core of concrete. This evolving temperature gradient combined with autogenous shrinkage generates mechanical stresses in the structure. Consequently, this stress state associated to the low-strength concrete in tension may lead to cracks.

The consideration of tensile creep is required to have a relevant estimation of the stress state. However, the tensile creep compliance of concrete is still being debated, a sensitivity study of this parameter is reported in this part.

Chemo-thermal modelling at early age

The hydration of concrete is a thermo-activated process. An Arrhenius law (Ulm and Coussy, 1998) is used to describe the kinetics of this chemical reaction:

$$\dot{\xi} = \tilde{A}(\xi) \exp\left(-\frac{E_a}{RT}\right)$$

in which ξ is the hydration degree, E_a is the activation energy, T is the temperature and $\tilde{A}(\xi)$ is the normalized affinity. The evolution of the temperature is governed by the thermal diffusion equation where C_{th} is the heat capacity, k_{th} is the thermal conductivity and L_{hyd} is the latent heat of hydration:

$$C_{th}\dot{T} = \nabla(k_{th}\nabla T) + L_{hyd}\dot{\xi}$$

Mechanical behaviour of concrete

Concrete is considered as a visco-elastic damageable material. At early age, the total strain in concrete, ϵ_{tot} , is calculated as the sum of the elastic strain, ϵ_{el} , the thermal strain, ϵ_{th} , the autogenous shrinkage, ϵ_{au} , and the basic creep, ϵ_{bc} .

$$\epsilon_{tot} = \epsilon_{el} + \epsilon_{th} + \epsilon_{au} + \epsilon_{bc}$$

The evolution of the damage variable is calculated according to the equations proposed by Benboudjema and Torrenti (2008). The Young's modulus, the Poisson's ratio and the tensile strength evolve with hydration according to the relationships proposed De Schutter and Taerwe (1996).

Basic creep is taken into account by using a rheological model made of two cells (Figure 1). The first one is a Kelvin-Voigt chain and is associated to the short-term creep. The long-term creep is assumed logarithmic and is calculated thanks to the dashpot whose the viscosity is taken proportional to time. The parameters of the basic creep vary due to hydration in order to consider the ageing characteristics of creep. Finally, a coefficient α_{bc} is introduced to take into account the difference between tension and compression (Hilaire et al., 2014).

$$\dot{\epsilon}_{bc} = \alpha_{bc} \frac{\langle \sigma \rangle^+}{\eta_{am}(t)} + \frac{\langle \sigma \rangle^-}{\eta_{am}(t)}$$

where $\langle \sigma \rangle^+$ is the positive part operator

The model is validated using the experimental campaign done by Briffaut et al (2012). The model and the experimental results agree quite closely. A realistic ageing viscoelastic behavior is simulated with this model; the identification of few parameters is required.

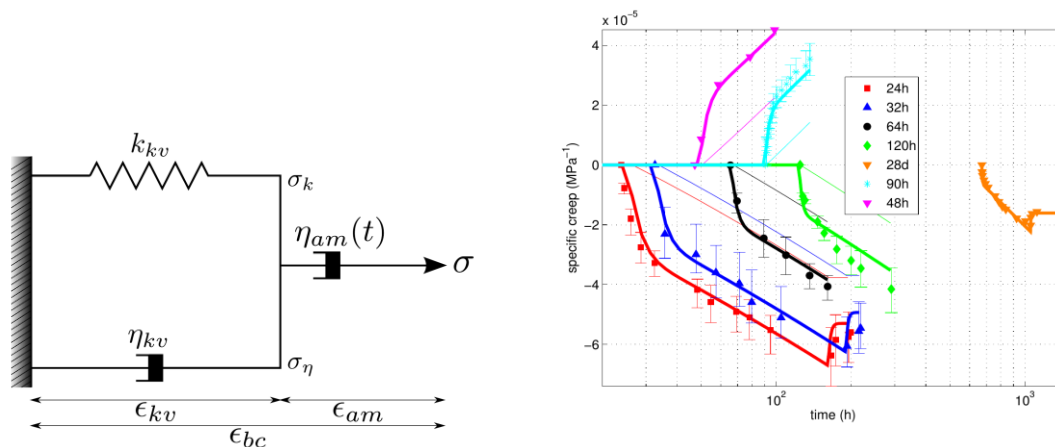


Figure 1. Basic creep chain and model validation based on experiments done by Briffaut et al (2012).

Influence of the tensile creep modelling on the early age behaviour of a massive concrete structure

The casting of a massive wall representative of concrete containment is simulated. The influence of the coefficient α_{bc} is assessed. Four cases are studied:

- Concrete is assumed as an elastic-damageable material.
- $\alpha_{bc} = 1.69$, this value was identified according to the experimental work of Briffaut et al (2012).
- $\alpha_{bc} = 1.69/3$, this value is associated to a very low creep compliance.
- $\alpha_{bc} = 1.69 \times 3$, this value is associated to a very high creep compliance

Final damage field is presented on the Figure 2; the final damage field is highly dependent on the value of the α_{bc} parameter. For $\alpha_{bc} = 1.69/3$, the structure is severely damaged when for $\alpha_{bc} = 1.69 \times 3$, the structure remains sound.

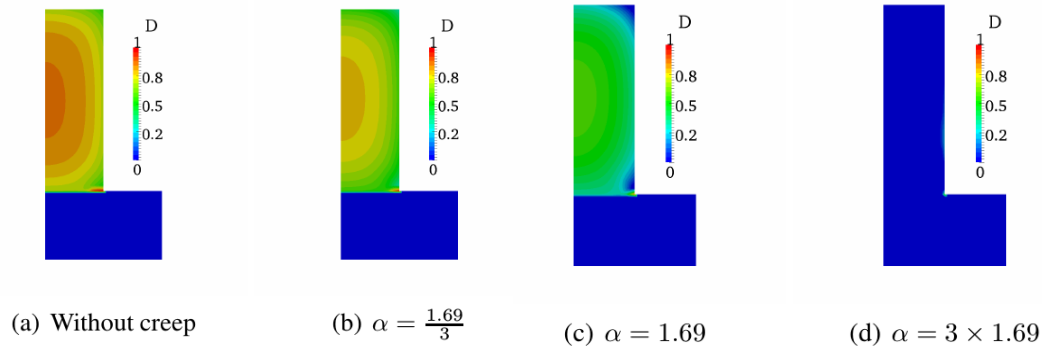


Figure 2. Damage field at the end of the early age for different values of α_{bc}

3. Long-term behaviour of concrete under biaxial loading

At long term, the amplitude of shrinkage and creep mainly affects the loss of prestress in a nuclear containment. Drying process of concrete is an important factor for quantifying delayed strains; it is the direct cause of the drying shrinkage and drying creep. Moreover, the diffusive nature of this process and the large dimension of the structure imply a gradient of relative humidity. Consequently, a stress state is created and damage may occur.

One of the specificities of this kind of structures is the biaxial compressive loading generated by the prestressing cables. It raises the question of the Poisson's ratio for creep. An experimental campaign has been performed to study this problem.

In the following section, the results of the biaxial basic creep test are detailed. Then, the modelling of water transfer is briefly presented and validated. Finally, the behaviour of a sample of concrete under a moderate relative humidity is simulated to validate the hygro-mechanical model at long term.

Basic creep under biaxial compressive stresses

An experimental set-up was designed to measure basic creep strains. The load is representative of the compressive stresses induced by the prestressing cables (8.5 Mpa in the x-axis and 12 Mpa in the y-axis). The test is performed under endogenous conditions. The displacement field is analysed by Digital Image Correlation (Tomicevic et al, 2013), this method enables to check whether the applied boundary conditions on the sample are appropriated.

The specific basic creep along the x-axis and the y-axis is plotted on the Figure 3. The two curves are coincident when the creep Poisson's ratio is identified. The experimental data exhibit a Poisson's ratio equal to -0.05.

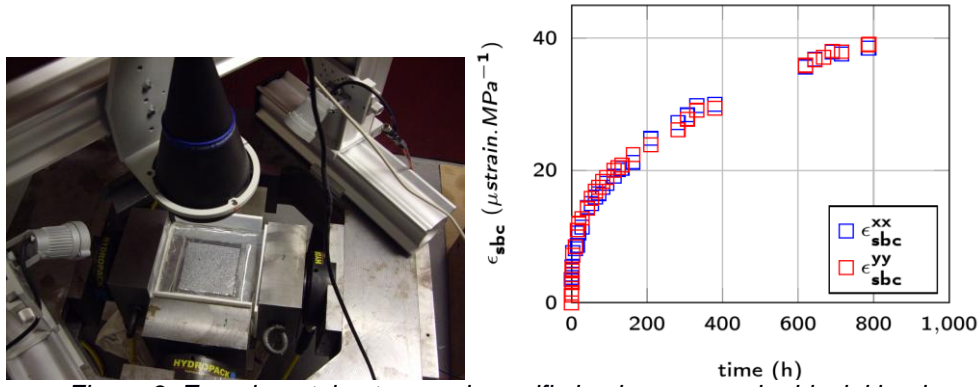


Figure 3. Experimental set-up and specific basic creep under biaxial load

Drying model

The characteristics of the studied concrete ($w/c = 0.55$) and the environmental conditions ($RH = 50\%$) enable to only consider the transfer of the liquid phase of water (Thierry et al., 2007). The mass flow of the liquid water is assumed darcean. Consequently, the mass balance equation for liquid water can be expressed as follows:

$$\rho_l \phi \frac{dS_l}{dp_c} \frac{\partial p_c}{\partial t} = \text{div} \left(\rho_l \frac{K_l}{\eta_l} k_{rl} \mathbf{grad}(p_c) \right)$$

where p_c is the capillary pressure, S_l the saturation degree, ϕ the porosity, ρ_l the density of water, K_l the intrinsic permeability, k_{rl} the relative permeability and η_l the viscosity.

A Van Genuchten relationship is used to link capillary pressure and saturation degree (Van Genuchten, 1980), the parameters of the law are identified according to the isotherm of desorption. Finally, the relative permeability is a function of the saturation degree (Chung and Consolazio, 2005).

Weight loss tests have been performed on cylindrical specimens subjected to desiccation after 28 days of curing. The evolution of the weight loss is plotted and compared to the result of the numerical simulation on the figure 4.

Drying shrinkage of concrete

At the material scale and following the mechanics of unsaturated porous media (Gawin et al., 2007), the intrinsic instantaneous drying shrinkage, ϵ_{ds} , is linked to the internal pressure, $S_l p_c$, via the Biot coefficient b :

$$\epsilon_{ds} = (1 - 2\nu)b \frac{S_l p_c}{E}$$

The viscous part of the shrinkage is calculated using the creep rheological model. Drying creep strain, ϵ_{dc} , is governed by the following equation where λ_{dc} is a material parameter:

$$\dot{\epsilon}_{dc}(t) = \lambda_{dc} \sigma |\dot{\epsilon}_{ds}(t)|$$

In addition to the previous weight loss measurement, the drying shrinkage is recorded. The diffusive nature of the water transfer implies some structural effects at the scale of the specimen. These effects can be captured with a finite element analysis. The evolution of drying shrinkage versus the weight loss is displayed with experimental results on the Figure 4. The shrinkage kinetics is well captured at the beginning of the dessiccation. However, the long-term shrinkage seems to be slightly overestimated.

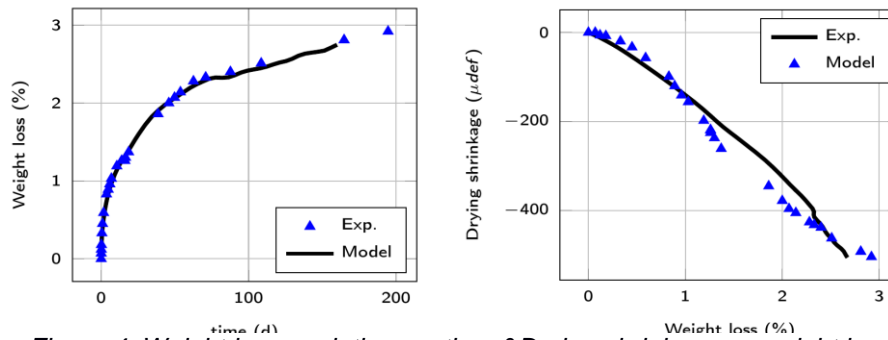


Figure 4. Weight loss evolution vs. time & Drying shrinkage vs. weight loss

4. Thermo-Chemo-Mechanical modelling of concrete at early age

An application case is modeled. The behavior of a massive wall is studied; the geometry of the wall is presented on the figure 5. It is built in three successive lifts; the duration between each lift is 28 days. The drying process of concrete is assumed to start 84 days after the casting of the first lift. At 209 days, compressive stresses are applied on the structure along the vertical and the longitudinal axis.

The delayed strain at long term is computed in two different ways. The first calculation is based on the Model Code 2010 (Torrenti and Benboudjema, 2015); the parameters of the relations proposed by this code are adjusted on experimental results. The second simulation is performed with the model presented in this paper. Figure 5 shows the comparison of in-situ measurements and strains prediction according to the two different models. The delayed strains predicted by MC2010 are clearly underestimated. On the other hand, the numerical results obtained from the TCHM model are more relevant. However, the kinetics of the delayed strain along the vertical axis is marginally overestimated.

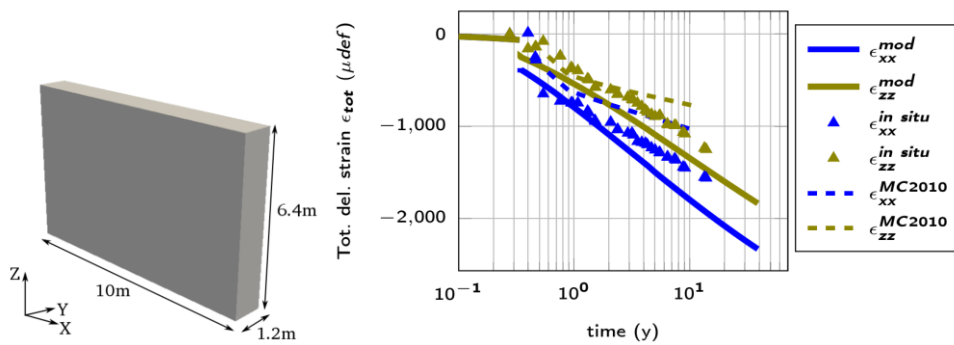


Figure 5. Geometry of the beam & comparison of in situ measurements and numerical results

5. Conclusions

A model able to simulate the aging and the behavior of a nuclear containment building is presented. Because of the size of the structure, the chemo-thermal problem at the early age is uncorrelated with the long term drying of concrete. The mechanical problem, however, is common to both phases. Consequently, the relations governing this problem are relevant from the casting until the end of the operating life of the structure. A relatively low number of parameters are introduced in this approach. If this choice simplifies the identification process of the parameters, the main phenomena influencing delayed behavior of concrete are considered.

Experimental tests have been performed to identify model parameters and to validate the modeling. In particular, an experimental set up has been developed to measure creep under biaxial loading.

The effectiveness of such a kind of approach is demonstrated through the numerical simulation of a massive prestressed concrete wall. The prediction of the delayed strains by the tool developed in this work seems more accurate than the one predicted by the Model Code 2010.

6. References

- Ulm, F.-J., Coussy, O (1998). Couplings in early-age concrete: from material modelling to structural design. *International Journal of Solid and Structures*, 35, 4295–4311.
- Benboudjema, F., Torrenti, J-M (2008). Early-age behaviour of concrete nuclear containments. *Nuclear Engineering Design*, 238, 2495-2506.
- De Schutter, G., Taerwe, L (1996). Degree of hydration-based description of mechanical properties of early age concrete. *Materials and Structures*, 29, 335-344.
- Hilaire, A., Benboudjema, F., Darquennes, A., Berthaud, Y., Nahas, G (2014). Modelling basic creep in concrete at early-age under compressive and tensile loading. *Nuclear Engineering Design*, 269, 222-230.
- Briffaut, M., Benboudjema, F., Torrenti, J-M., Nahas, G (2012). Early age basic creep for massive structures: experimental results and rheological modelling. *ACI Materials Journal*.
- Thiery, M., Baroghel-Bouny V., Bourneton N., Villain, G. (2007). Modélisation du séchage des bétons. *Revue Européenne de Génie Civil*, 11, 541-577.
- Van Genuchten, M.T, A Closed-form Equation for Predicting the Hydraulic Conductivity of Unsaturated Soils. *Soil Science Society of American Journal*, 44, 892-898.
- Chung, J-H., Consolazio, G-R. (2005). Numerical modeling of transport phenomena in reinforced concrete exposed to elevated temperatures of mechanical properties of early concrete. *Cement and Concrete Research*, 35, 597-608.
- Tomičević, Z., Hild, F., Roux, S. (2013). Mechanics-aided digital image correlation. *The Journal of Strain Analysis for Engineering*, 48, 330-343.
- Gawin, D., Pesavento, F., Schrefler, B. A. (2007). Modelling creep and shrinkage of concrete by means of effective stresses. *Materials and Structures*, 40(6), 579-591.
- Benboudjema, F., Torrenti, J-M., (2015). On the Very Long-Term Delayed Behavior of Biaxially Prestressed Structures: The Case of the Containments of Nuclear Power Plants. *CONCREEP10. September 2015*, 631-639.

EARLY-AGE NON-AGING VISCOELASTIC PROPERTIES OF CEMENT PASTE: LESSONS LEARNED FROM MACROSCOPIC TESTING

Muhammad Irfan-ul-Hassan^{a, b} (muhammad.irfan-ul-hassan@tuwien.ac.at), Bernhard Pichler^a, Christian Hellmich^a

^a Institute for Mechanics of Materials and Structures, Vienna University of Technology (TU Wien), Karlsplatz 13/202, A-1040 Vienna, Austria

^b Civil Engineering Department, University of Engineering and Technology, Lahore, Pakistan

ABSTRACT. Elastic and creep properties of ordinary Portland cement pastes are quantified, based on a very recently developed early-age testing protocol consisting of hourly-repeated three-minutes-long creep experiments. The testing series is started 21 hours after production and it is continued until the specimens reach a material age of eight days. Up to that age, the specimens are conditioned to 20 degrees Celsius. During each individual creep test, the material microstructure remains virtually the same, because hydration *does not* proceed significantly during three minutes. Two subsequent creep tests, in turn, characterize two *different* microstructures, because hydration *does* proceed significantly during one hour. Non-destructive testing is ensured by subjecting specimens to compressive loads smaller than or equal to 15 percent of the uniaxial compressive strength. The measured strain histories can be explained very well by means of a power-law type creep function, and this allows for identification of elastic Young's moduli, creep moduli, and power-law exponents, as functions of the material age. Complementary quasi-isothermal differential calorimetry allows for assigning identified elastic and creep properties to specific values of hydration degree. Notably, the quasi-statically determined elastic Young's moduli agree very well with dynamic Young's moduli quantified by means of ultrasound testing.

1. Introduction

Standard early-age creep tests on cementitious materials typically last so long that the microstructure existing at the time of loading differs – because of ongoing hydration – from the microstructure existing at the time of unloading. This is referred to as *aging* creep testing. It does *not* provide access to the creep properties of a *specific* material microstructure. This has motivated us to develop an innovative creep testing protocol which provides quantitative access to creep properties of young cement pastes with specific microstructures.

We perform hourly-repeated minutes-long creep tests on cement pastes, during the first week after their production. The duration of our tests is so short that there is not enough time for hydration to change the microstructure significantly. One hour, in turn, is enough at early ages that hydration changes the microstructure considerably. Therefore, our test series allows for characterizing the evolution of microstructure-specific creep properties, throughout the first week after material production. In this context, it is important to perform non-destructive testing, and this is ensured by subjecting the specimens to maximum compressive forces amounting to only 15 percent of the compressive strength which is reached at the time instant of testing.

This paper is structured as follows. Materials and methods are described in Section 2. The test evaluation strategy for identification of elastic Young's modulus and of power-law creep properties is the topic of Section 3. Results are illustrated both as functions of sample age and as functions of the degree of hydration, see Section 4. After a short discussion, the paper closes with conclusions given in Section 5.

2. Materials and Methods

Raw Materials

The used raw materials include a commercial cement of type CEM I 42.5 N and distilled water. Herein, we report on test results obtained with cement pastes produced with an initial water-to-cement mass ratio amounting to $w/c = 0.50$.

Production and Storage of Specimens

Specimens are cylinders with a diameter of 7.0 cm and a height of 30.0 cm. Immediately after sample preparation, the opening of the mold is sealed by several layers of food preservation foil, in order to avoid evaporation of water. Subsequently, the specimens are stored inside a temperature chamber at 20 degrees Celsius. The specimens are demolded at an age of 20 hours. Again, the free surfaces of the specimens are wrapped in several layers food preservation foil, in order to prevent the specimens from drying.

Test Setup

The test setup is very similar to the one recently developed for early-age stiffness characterization of cement pastes, see [1]. Five Linear Variable Differential Transducers (LVDTs), attached to two aluminum rings, measure the axial deformation in the central region of the samples, see Fig. 1. In more detail, the aluminum rings are positioned at a mutual distance of 16.0 cm, each of them 7.0 cm distant from the interfaces between specimen and load platens, in order to ensure shear-free stress and strain states in the measurement region. The described setup is placed inside a temperature chamber which is installed an electromechanical universal testing machine, see Fig. 1.



Figure 1. Test setup including cylindrical specimen made of cement paste and five Linear Variable Differential Transducers attached to the specimen using two parallel aluminum rings

Creep Testing Protocol

At a material age of 21 hours, the first loading-unloading test is performed [2]. Thereby, the load plateau is held constant for a duration of three minutes. Similar tests are repeated once every hour. Loading and unloading are carried out under prescribed force-rates: compressive loading is increased at a speed of 7.697 kN/s (equivalent to a stress rate of 2.0 MPa/s), while unloading is carried out with 3.849 kN/s (equivalent to a stress rate of 1.0 MPa/s), see Fig. 2. As to ensure non-destructive testing, load plateau levels are

selected to be smaller than or equal to 15 % of the compressive strength, see Fig. 2. Notably, the compressive strength of cement paste can be predicted reliably, based on a validated multiscale model [3].

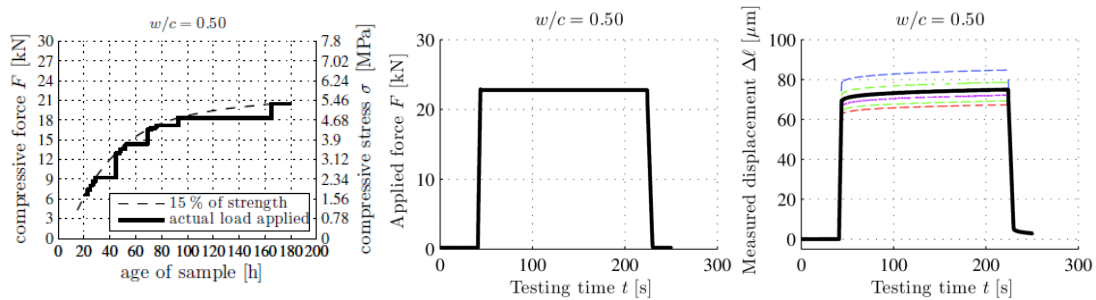


Figure 2. Creep testing approach: prescribed compressive forces/stresses in the 168 individual creep tests (left), force history prescribed during the three-minutes creep test performed at a material age of 70 h (middle), measured and mean displacements quantified by five LVDTs (right), see also [2]

3. Test Evaluation: Identification of Elastic and Creep Properties

Test evaluation aims at quantifying the elastic Young's modulus and creep properties. This is carried as explained below.

Evaluation of elastic Young's Modulus

At first, we determine – for each individual test – the *unloading* modulus E_u from pointwisely defined stress-strain relationships. Notably, cement pastes are highly creep active materials at early ages, such that measured strains during unloading are not purely elastic, but they do also include creep deformations. Therefore, the unloading modulus can only serve as a first estimate for the *elastic* Young's modulus E .

In order to identify the elastic Young's modulus, we proceed as follows. Based on the unloading modulus, we quantify the creep strains, simply by subtracting the elastic strains from the total strains, see also [2]

$$\epsilon_{creep}(t) = \epsilon_{total}(t) - \epsilon_{elastic}(t) \quad (1)$$

The resulting creep strain evolution exhibits an unexpected feature. The creep strains, namely, should be consistently *compressive*, but *tensile* creep strains are obtained at the start of the loading phase, see the “tensile undershooting” peak shown in Fig. 3 (a). This non-physical situation results from the fact that unloading modulus slightly underestimates the elastic Young's modulus. Therefore, starting with unloading modulus, progressively larger estimates of the elastic Young's modulus are considered in Eq. (1). This delivers creep strain evolutions exhibiting progressively diminishing tensile undershooting peaks. Once the tensile peak has disappeared for the first time, i.e. once entirely *compressive* creep strains prevail, see Fig. 3(b), the progressive increase of Young's modulus is stopped, and the obtained value is treated as the *elastic* Young's modulus. The corresponding creep strain history is the basis for quantifying creep properties, as discussed next.

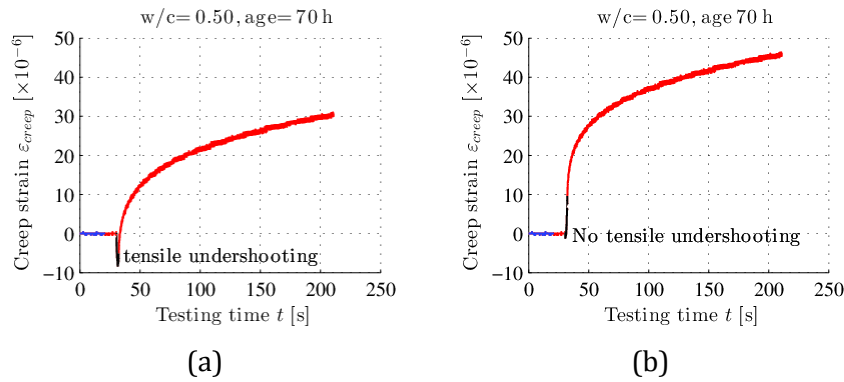


Figure 3. Creep strains obtained with: (a) unloading modulus (b) identified elastic Young's modulus, see also [2]

Quantification of Power-Law Creep Properties

In order to quantify creep properties, we follow Tamtsia and Beaudoin [4] and use a power-law type creep function. This model limits the number of fitting parameters to only two. Considering a loading history, where the stress is (i) increased, instantaneously at time instant t_o , up to stress level σ_o , and (ii) kept constant afterwards, the power-law creep function allows for quantification of the strain history as

$$\epsilon_{creep}^{model}(t) = \sigma_o \int_{t_o}^t C \left(\frac{\tau - t_o}{t_{ref}} \right)^\gamma d\tau \quad t \geq t_o \quad (2)$$

In Eq. (2), $t_{ref} = 1$ day denotes a constant reference time, t_o denotes the time instant of sudden loading, C the creep compliance rate at time $t = t_o + t_{ref}$, and γ represents a dimensionless power-law exponent. Since creep strains also develop during the loading phase of our creep tests, the force history is subdivided into a series of small loading steps and Boltzmann's superposition principle is applied

$$\epsilon_{creep}^{model}(t) = \sum_{i=0}^n \frac{F(t_{i+1}) - F(t_i)}{A} \frac{1}{E_c} \left(\frac{t - t_i}{t_{ref}} \right)^\beta \quad (3)$$

Where $E_c = \frac{\gamma+1}{C t_{ref}}$ is referred to as the creep modulus, and $\beta = \gamma + 1$ denotes, by analogy to γ in Eq. (2), a dimensionless power-law exponent.

Based on Eq. (3), experimentally derived creep histories are fitted by adjusting the creep modulus E_c and the power-law exponent β , such that the difference between the measured and modeled creep strains attains a minimum, i.e.

$$\epsilon_{SRSS}(E_c, \beta) = \sqrt{\frac{1}{N} \sum_{i=1}^N [\epsilon_{creep}(t_i) - \epsilon_{creep}^{model}(t_i)]^2} \rightarrow \min \quad (4)$$

4. Results and Discussion

Evaluation of all experimental results, obtained by testing two nominally identical specimens, allows for quantification of the temporal evolutions of the elastic Young's

modulus, the creep modulus, and the power-law exponent, see Fig. 4. Both the elastic Young's modulus and the creep modulus increase under-linearly with increasing age of cement paste, see Figs. 4(a) and (b). The power-law exponent β slightly decreases with increasing age of cement paste, see Fig. 4(c). Overall, the quality of test repetition is very satisfactory and this strongly corroborates the significance of the used creep testing protocol.

The degree of hydration ξ is a much more preferable maturity parameter compared to the age of the material, because the speed of the chemical hardening reaction between cement and water increases significantly with increasing curing temperature. This provides the motivation, to study the quantified elastic and creep properties as a function of the degree of hydration, see Fig. 5. The elastic Young's modulus increases linearly with increasing hydration degree, in the studied regime of hydration degrees from 35 to 65%. The creep modulus increases over-linearly with increasing hydration degree. The power-law exponent β slightly and linearly decreases with increasing hydration degree.

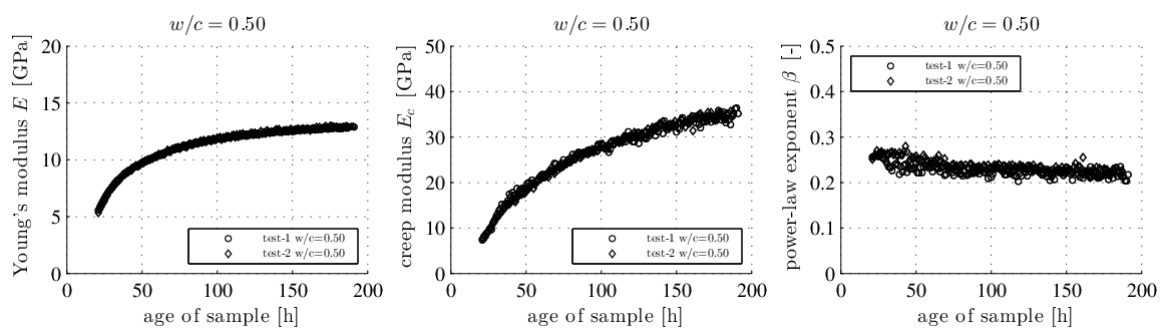


Figure 4. Temporal evolutions of: elastic Young's modulus E (left), creep modulus E_c (middle), and power-law exponent β (right), for cement paste with $w/c = 0.50$, see also [2]

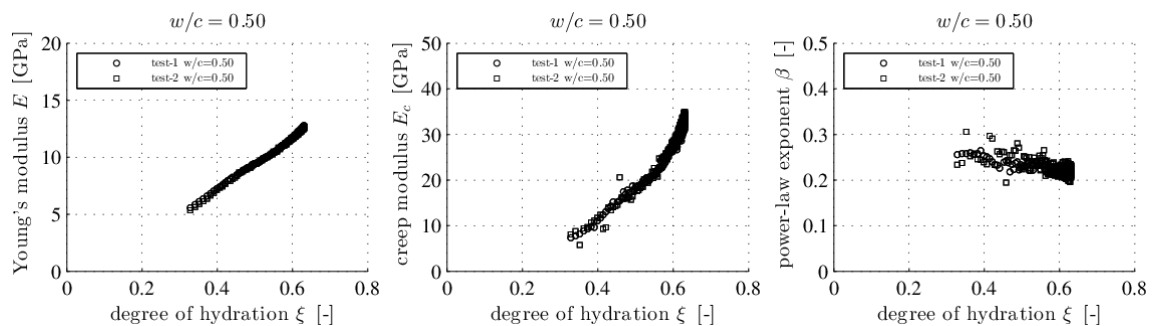


Figure 5. Evolutions of: elastic Young's modulus E (left), creep modulus E_c (middle), and power-law exponent β (right), as functions of degree of hydration ξ , for cement paste with $w/c = 0.50$, see also [2]

Very remarkably, the quasi-statically identified elastic Young's moduli are equal to dynamic Young's moduli determined by Karte et al.¹ on the same material, see [2].

Conclusions

The following conclusions are drawn.

- A recently developed early-age creep testing protocol for young cementitious materials provides valuable quantitative insight into the evolution of elastic and creep properties of specific material microstructures. This will be valuable for development and validation of future multiscale models for creep of cement paste.

- The described strategy for determining quasi-static *elastic* Young's moduli delivers stiffness values that are identical to dynamic Young's moduli derived from measured wave speeds of ultrasonic longitudinal and shear waves. This underlines – in the framework of creep-active materials – the importance of distinguishing (i) *loading* Young's moduli (which are likely to be of visco-elastic visco-plastic nature), (ii) *unloading* Young's moduli (which are likely to be of visco-elastic nature), and (iii) truly *elastic* Young's moduli.

References

- [1] Karte, P., Hlobil, M., Reihnsner, R., Dörner, W., Lahayne, O., Eberhardsteiner, J., and Pichler, B. (2015) Unloading-based stiffness characterization of cement pastes during the second, third, and fourth day after production, *Strain* 51 (2) 156 – 169.
- [2] Irfan-ul-Hassan, M., Pichler, B., Reihnsner, R., and Hellmich, Ch. (2015) Elastic and creep properties of young cement paste, as determined from hourly repeated minutes-long quasi-static tests. Under revision.
- [3] Pichler, B. and Hellmich, Ch. (2011) Upscaling quasi-brittle strength of cement paste and mortar: A multi-scale engineering mechanics model, *Cement and Concrete Research* 41 (5) 467 – 476.
- [4] Tamtsia, B., Beaudoin, J., and Marchand, J. (2004) The early age short-term creep of hardening cement paste: Load-induced hydration effects, *Cement and Concrete Composites* 26 (5) 481 – 489.

EARLY-AGE BEHAVIOUR OF OIL-WELL CEMENT AND WELL INTEGRITY¹

Nicolaine Agofack (nicolaine.agofack@ntnu.no)

ENPC, Champs sur Marne, France & TOTAL EP, Pau, France
Currently at SINTEF-Petroleum, Trondheim, Norway

ABSTRACT.

The early-age mechanical properties of class G cement (w/c = 0.44) are studied in this paper. The experimental setups including an oedometric cell, an ultrasonic cement analyzer and a calorimeter are used to analyse the critical time creation of residual strain, the static modulus, the macroscopic shrinkage and the stress–strain behaviour. Various conditions of temperature (between 7 and 30°C) and pressure (between 0.3 and 45MPa) are explored. It is found that after a hydration degree of about 18%, mechanical loadings can induce residual strain in the cement paste. The elastic oedometric modulus increases during hydration and depends on the hydrating pressure. The macroscopic shrinkage and the stress–strain behaviour are coupled and are more affected by the hydrating pressure than the hydrating temperature. At 144 hours and for samples hydrated under low pressure significant residual strains occur due to application of the mechanical loading.

Keywords: early-age, cement hydration, shrinkage, stress–strain behaviour, cement-sheath integrity, residual strain.

1- Introduction

In oil and gas industry, when drilling exploration or development wells, a mud is used for which the principal functions are to support the walls of the geological formation, to maintain the wellbore stability, to cool and clean the drill bit, to carry out the cuttings and to provide hydrostatic pressure which helps to prevent formation fluids entering into the well bore. Steel tubular (called "*casing*") is then run into the well and cement slurry is pumped to fill the annulus space between two casings or between the casing and the geological formation. Time is given for the cement slurry to harden and to form a cement sheath, which plays an important role for well integrity. Along the well, it provides zonal isolation of different fluids; it protects the tubular against corrosion and provides mechanical support. The loss of cement-sheath integrity can result in the pressurization of annulus, in gas migration up to a shallower formation or to the surface, and, in catastrophic cases, in a blowout and total damage of the infrastructure. The cement paste is an evolving porous material, its state changes progressively from fluid to solid during the hydration process. Along the well, different compositions of cement slurries can be used and their hydration takes place in different conditions of temperature and pressure. Therefore, at a given time, cement paste behaviour and properties depend on (1) the slurry composition of the cement paste including water-to-cement (w/c) ratio or presence of additive agents, (2) the hydration conditions of temperature and pressure and (3) the effects of the loading history on the cement paste. Indeed, during the life of a well, from drilling to completion, production and P&A (plug and abandonment), the cement sheath is submitted to various mechanical and thermal loadings that can potentially damage its principal properties and alter its performance. Analysing the well safety conditions and the response of the cement sheath submitted to these loadings needs an appropriate constitutive law for the cement paste in well conditions. Since some of these loadings are applied before the complete hydration of

¹ The studies presented in this paper are covered by a **Patent of TOTAL EP**

the cement paste, as for example during a casing test, the simulation of the response of cement paste needs the knowledge of the initial state of stress in the cement paste. The evaluation of the stress state needs a complete simulation of the cement paste behaviour in well conditions from the placement to the final hydration. The constitutive model should be therefore able to simulate the cement paste behaviour during hydration. As mentioned above, the cement paste behaviour varies with cement formulation in terms of w/c ratio or cement powder composition, the hydration conditions in terms of temperature and pressure and also the previous loadings. These aspects need to be taken into account in the constitutive law. In this work, our purpose was to study the poro-chemo-mechanical behaviour of cement paste at very early-age, during the first six days of hydration. In addition, some cement samples submitted to mechanical loadings during this early-age were also tested after six months in order to analyse the effects of early-age loadings on the long-term properties. The material used was an oil well cement class G, with water-to-cement ratio equal to 0.44. This material with similar composition was used in previous studies (Ghabezloo, 2008; 2010; 2011; Ghabezloo, et al., 2008; 2009; Vu, 2012, Vu et al., 2012). The hydration conditions correspond to a temperature range from 7 to 30°C and a pressure range from 0.3 to 45MPa. Three experimental devices were used: a uniaxial strain (oedometric) cell, an Ultrasonic Cement Analyzer (UCA) and a high pressure high temperature calorimeter. The oedometric equipment was used to measure continuously the total deformation of the hydrating cement paste at controlled temperature and pressure conditions. It was also used to measure and to study the static elastic modulus and the complete stress–strain response of cement paste during its hydration by performing mechanical unloading/loading cycles on the cement paste samples even before the formation of a solid structure, what would be impossible in a standard triaxial cell. The UCA was used to measure the evolution of the ultrasonic compressive P-wave velocity during cement hydration. It measures the transit-time of P-waves between the top and the bottom of the sample. The calorimeter was used to estimate the degree of hydration from the measure of hydration heat.

2- Critical time for creation of residual strain

The cement sheath is submitted to various loadings during the drilling or the casing test. According to Jackson (1993), Behrmann et al. (1997) and Thiercelin et al. (1997), the increase of pressure during drilling can exceed 40MPa in the oil wells, and the applied pressure during a casing test can vary from a few tens of MPa in normally pressurized reservoirs to more than 80MPa in high pressure reservoirs. Waiting too long after the placement of cement slurry in the annulus space for performing these tests could potentially induce significant residual strains in the cement paste and this could lead to the formation of a micro-annulus or to cement damage (Bois, et al., 2011; Bois, et al., 2012; Garnier, et al., 2010; Bois, et al., 2013). A key question is: after how long the loading cycles in the cement paste can lead to the creation of residual strains? The experimental results revealed that during the hydration, there is a critical time after which, the application of mechanical loadings can potentially induce residual strain in cement paste. This time, called "*critical time for creation of residual strain*" was reached at constant hydration degree between 18% and 20%. It was also demonstrated that this critical time can be determined through a UCA test. The Boundary Nucleation and Growth (BNG) model (Avrami 1939; 1940; 1941; Cahn, 1956) was used to model the pressure and temperature dependence of this critical time. Within the range of studied temperatures and pressures, the predictive capacity of the BNG model for estimation of the critical time for creation of residual strain was demonstrated.

3- Elastic static properties of hydrating cement paste

Another important part of this work consists in measuring the elastic static modulus of cement paste during its hydration under different conditions of temperature and pressure. This was done by applying several unloading/reloading mechanical cycles on the cement paste samples, every 5 or 10 hours during hydration. Every loading cycle was run at 3MPa/min and its duration was about 20 minutes. At relatively low temperature of the test (7°C), the cycle was then considered as performed at constant hydration degree. The experimental results showed the increase of the static oedometric modulus during hydration. It was approximatively 3.5GPa for cement slurry, more than the bulk modulus of water, probably due to the presence of cement particles (Vu, 2012). After 300 hours of hydration, the oedometric modulus was found to be approximatively 15GPa and 18GPa for samples hydrated under 15 and 25MPa, respectively.

4- Shrinkage and stress-strain behavior

At very early-age, the shrinkage of cement paste and the decrease of its pore pressure are considered to be the main cause of leakage in oil and gas wells (Parcevaux et al., 1984; Justnes et al., 1995; Lyomov et al., 1997). When hydration of cement is taking place at constant temperature and under atmospheric pressure, the external volume reduction is called autogenous shrinkage (Jensen, et al., 2001; Bentz, et al., 2004; Jaouadi, 2008), commonly encountered in civil engineering. If the hydrating pressure is different from the atmospheric pressure, the diminution of the external volume of cement paste is called *macroscopic shrinkage*. The macroscopic shrinkage of cement paste was measured for different conditions of temperature and pressure. It was found that at constant hydration temperature, the macroscopic shrinkage increased with the increase of the hydrating pressure. After 140 hours of hydration, it was about 10mm/m, 22mm/m and 36mm/m for samples hydrated under 0.3, 10 and 45MPa, respectively. Under similar hydration pressures, the effect of temperature on the macroscopic shrinkage is more pronounced during the first 60 hours of hydration and seems to vanish for higher hydration states. The long-term effect of temperature on the macroscopic shrinkage was then less important compared to that of the hydrating pressure. These results were compatible with those found in the literature (API, 1997; Reddy, et al., 2007; Reddy, et al., 2009) and with the more recent ones of Abuhaikal et al. (2013). In order to study the effect of hydrating conditions on stress-strain behaviour of the cement paste, at 144 hours of hydration, mechanical loading/unloading cycles were applied to every above-mentioned sample. The results showed that the stress–strain behaviour of cement paste at 144 hours is more affected by the hydration pressure than by the hydration temperature. In particular, for samples hydrated under low pressure (e.g. 0.3 or 3MPa), significant residual strains occur due to application of the mechanical loading. This showed a high risk of creation of macro-cracks and micro-annulus at shallow depths of cement sheath.

5- Modelling

A coupled chemo-poro-mechanical model was developed to simulate the macroscopic shrinkage of cement paste hydrated at different conditions of temperature and pressure. A modified Cam-Clay type yield surface with an associate flow rule was used. Two hardening mechanisms are considered, the degree of hydration and the accumulation of plastic volumetric strain. It was assumed that, before the percolation threshold (approximatively for a degree of hydration less than 20%), the volumetric deformation is totally irreversible. After this threshold, cement is considered as a porous material (Ghabezloo et al. 2008) and is described within the poromechanical framework (Biot et al., 1957; Rice et al., 1976;

Zimmerman, 1991; Vardoulakis et al., 1995; Coussy, 2004; Ghabezloo et al., 2008). Its deformations were then divided into two parts: elastic and plastic. The chemical shrinkage of the cement results in a decrease of pore pressure during hydration and potentially the desaturation of the cement paste. At a given time, the pore pressure decrease depends on the current porosity ϕ , and the poroelastic parameters of the cement paste. The poromechanical formulation was therefore extended to the case of partially saturated media through mainly the introduction of an effective stress parameter (χ) (Aichi and Tokunaga, 2011, 2012; Ghabezloo and Hemmati, 2011). The poroelastic parameters vary during hydration and with hydration conditions of temperature and pressure. Their estimation was done through a multi-scale homogenization method, with self-consistent scheme (Ulm et al., 2004; Pichler et al., 2009; Ghabezloo, 2010). At a given time, the degree of hydration depends on cement paste composition as well as hydration conditions of temperature and pressure. A coupled BNG-Diffusion model was developed for cement hydration (Fudji & Kondo, 1974; Bernard et al., 2003 and Vu, 2012). The results from BNG-Diffusion model and from homogenization were used as inputs in the macroscopic shrinkage's model. This latter was calibrated and validated with the range of studied temperature and pressure. It was demonstrated that, under low stress conditions, the cement paste became unsaturated after a certain degree of hydration. It was also observed that, due to the macroscopic shrinkage, there was a possible debonding of cement paste from the walls of the oedometric cell. In oil and gas well, this reflects the possible debonding of cement sheath from formation and/or from casing due to the macroscopic shrinkage, which can lead to fluids leakage. At a given degree of hydration, the simulation of the stress–strain behaviour of cement paste due to the mechanical loading needs the knowledge of the initial state of stress in the cement paste. This was provided by the simulation results of macroscopic shrinkage. A strong coupling was found between the macroscopic shrinkage and the stress-strain behaviour of cement paste. Modelling separately the two phenomena can lead to misunderstand the stress-strain behaviour of the cement during the early-age. The simulation results showed an excellent predictive capacity of the model and the possible (re)saturation during the mechanical loading.

Acknowledgements

The authors gratefully acknowledged TOTAL for supporting this research. They also wish to thank Joselin DE-LA-IGLESIA and Sandrine ANNET-WABLE from TOTAL for performing calorimeter experiments and Nicolas CRUZ from ACEI for his assistance in the testing program.

6- References

- Abuhaikal, M., Musso, S., Thomas, J. & Ulm, F.-J. (2013). An apparatus for Dissecting Volumetric Changes in Hydrating Cement Paste. *Mechanics and Physics of Creep, Shrinkage and Durability of Concrete*, doi: 10.1061/9780784413111.037, 316-323.
- Aichi, M. & Tokunaga, T. (2011). Thermodynamically consistent anisotropic constitutive relations for a poroelastic material saturated by two immiscible fluids. *International Journal of Rock Mechanics & Mining Sciences*, 48, 580–584 .
- Aichi, M. & Tokunaga, T. (2012). Material coefficients of multiphase thermoporoelasticity for anisotropic micro-heterogenous porous media. *International journal of Solid and Structures*, 49, 3388–3396.
- API (1997). Shrinkage and Expansion in Oilwell Cements. *API Publishing Services*, Washington.

- Avrami, M. (1939). Kinetics of phase change I., General Theory. *Journal of Chemical Physics*, 7, 1103–1112.
- Avrami, M. (1940). Kinetics of phase change II., Transformation-Time Relations for Random Distribution of Nuclei. *Journal of Chemical Physics*, 8, 212–224.
- Avrami, M. (1941). Granulation, Phase Change, and Microstructure. Kinetics of phase change III. *Journal of Chemical Physics*, 9, 177–184.
- Behrmann, L. A., Li, J. L., Venkitaraman, A. & Li, H. (1997). Borehole Dynamics During Underbalanced Perforating. *Society of Petroleum Engineers*, Issue SPE 38139, 17–24.
- Bentz, D. P. & Jensen, O. M. (2004). Mitigation strategies for autogenous shrinkage cracking. *Cement & Concrete Composites*, 26, 677–685.
- Bernard, O., Ulm, F.-J. & Lemarchand, E. (2003). A multiscale micromechanics-hydration model for the early-age elastic properties of cement-based materials. *Cement and Concrete Research*, 33, 1293–1309.
- Biot, M. A. & Willis, D. G. (1957). The elastic coefficients of the theory of consolidation. *Journal of Applied Mechanics*, 24, 594–601.
- Bois, A.-P., Garnier, A., Rodot, F., Saint-Marc J. & Aimard, N. (2011). How to Prevent Loss of Zonal Isolation Through a Comprehensive Analysis of Micro-Annulus Formation. *SPE Drilling & Completion*, 13–31.
- Bois, A.-P., Garnier, A., Galdiolo, G. & Laudet, J.-B. (2012). Use of a Mechanistic Model To Forecast Cement-Sheath Integrity. *SPE Drilling & Completion*, no. SPE 139668, 303–314.
- Bois, A.-P., Vu, M.-H., Ghabezloo, S., Garnier, A. & Laudet, J.-B. (2013). Cement sheath integrity for CO₂ storage—An integrated perspective. *Energy Procedia*, 37, 5628–5641.
- Cahn, J. W. (1956). The kinetics of grain boundary nucleated reactions. *Acta Metallurgica*, 4, 449–459.
- Coussy, O. (2004). Poromechanics. *John Wiley and Sons*.
- Fuji, K. & Kondo, W. (1974). Kinetics of the hydration of tricalcium silicate. *Journal of the American Ceramic Society*, 57, 492–497.
- Garnier, A., Saint-Marc J., Bois, A.-P. & Kermanac'h Y. (2010). A Singular Methodology to Design Cement Sheath Integrity Exposed to Steam Stimulation. *SPE Drilling & Completion*, no. SPE 117709, 58–69.
- Ghabezloo, S. (2008). Comportement thermo-poro-mécanique d'un ciment pétrolier. Thèse de Doctorat, *École Nationale des Ponts et Chaussées*, Paris, France, 204p.
- Ghabezloo, S., Sulem, J., Guedon, S., Martineau, F. & Saint-Marc, J. (2008). Poromechanical behaviour of hardened cement paste under isotropic loading. *Cement and Concrete Research*, 38, 1424–1437.
- Ghabezloo, S., Sulem, J. & Saint-Marc, J. (2009). The effect of undrained heating on a fluid saturated hardened cement paste. *Cement and Concrete Research*, 39, 54–64.
- Ghabezloo, S. (2010). Association of macroscopic laboratory testing and micromechanics modelling for the evaluation of the poroelastic parameters of a hardened cement paste. *Cement and Concrete Research*, 40, 1197–1210.
- Ghabezloo, S. & Hemmati, S. (2011). Poroelasticity of a micro-heterogenous material saturated by two immiscible fluids. *International Journal of Rock Mechanics and Mining Sciences*, 48, 1376–1379.
- Jackson, P.B. (1993). Effect of Casing Pressure on Gas Flow Through a Sheath of Set Cement, *SPE/IADC Drilling Conference*, SPE/IADC 25698, 215-224.
- Jaouadi, I. (2008). Etude numérique et expérimentale du retrait endogène de la pâte de ciment au jeune âge. Thèse de doctorat, *École Polytechnique Fédérale de Lausanne*, Suisse, 209p.
- Jensen, O. M. & Hansen, P. F. (2001). Autogenous deformation and RH-change in perspective. *Cement and Concrete Research*, 31, 1859–1865.
- Parcevaux, P. A., Sault, P. H. & Schlumberger, E. a. F. D., (1984). Cement Shrinkage and Elasticity : A New Approach for a Good." SPE Annual Technical Conference and Exhibition. Society of Petroleum Engineers, Houston, Texas, 1-7.

- Pichler, B., Hellmich, C. & Eberhardsteiner, J. (2009). Spherical and acicular representation of hydrates in a micromechanical model for cement paste: prediction of early-age elasticity and strength. *Acta Mech*, 203, 137–162.
- Reddy, B. R., Santra, A., McMechan, D., Gray, D., Brenneis, C. & Dunn, R. (2007). Cement Mechanical-Property Measurements Under Wellbore Conditions. *Society of Petroleum Engineers*, 33–38.
- Reddy, B. R., Xu, Y., Ravi, K. & Gray, D. (2009). Cement-Shrinkage Measurement in Oilwell Cementing -A Comparative Study of Laboratory Methods and Procedures. *Society of Petroleum Engineers*, Issue SPE 103610, 104–114.
- Rice, J. R. & Cleary, M. P. (1976). Some basic stress diffusion solutions for fluid-saturated elastic porous medias with compressible constituents. *Reviews of Geophysics and Space Physics*, 14, 227–241.
- Thiercelin, M. J., Dargaud, B., Baret, J. F. & Rodriguez, W. J. (1997). Cement Design Based on Cement Mechanical Response. *Society of Petroleum Engineers*, Issue SPE 38598, 337–348.
- Ulm, F.-J., Constantinides, G. & Heukamp, F. H. (2004). Is concrete a poromechanics material? - A multiscale investigation of poroelastic properties. *Materials and Structures / Concrete Science and Engineering*, 37, 43–58.
- Vardoulakis, I. & Sulem, J. (1995). Bifurcation Analysis in Geomechanics. *Blackie Academic and Professiona*.
- Vu, M.-H., Sulem, J. Ghabezloo, S., Laudet, J.-B., Garnier, A. & Guédon, S. (2012). Time-dependent behaviour of hardened cement paste under isotropic loading. *Cement and Concrete Research*, doi:10.1016/j.cemconres.2012.03.002.
- Vu, M.-H. (2012). Effet des contraintes et de la température sur l'intégrité des ciments des puits pétroliers. Thèse de Doctorat, *École Nationale des Ponts et Chaussées*, Paris, France, 240p.
- Zimmerman, R. (1991). Compressibility of sandstones. *Elsevier Sci*.

BRITTLE AND SEMIBRITTLE DEFORMATION OF LIMESTONES: EXPERIMENTS AND MODEL

Aurélien Nicolas (nicolas@geologie.ens.fr), Jérôme Fortin, Yves Guéguen
Laboratoire de Géologie, Ecole Normale Supérieure, CNRS UMR 8538, Paris, France.

ABSTRACT. Deformation of carbonate rocks can either occur with dilatancy or compaction, having implications for porosity changes, failure and petrophysical properties. Hence, understanding the micro-mechanisms responsible for deformation is of great interest. In this study, the brittle-ductile transition of a low-porosity limestone is observed during constant strain rate deformation experiments performed at various confining pressures and $T=70^{\circ}\text{C}$. A constitutive model for the stress-strain relation during deformation of low-porosity carbonate rocks is derived from the micro-mechanisms identified. The micro-mechanical model is based on (1) brittle crack propagation, (2) a plasticity law for porous media with hardening and (3) crack nucleation due to dislocation pile-ups. The model adequately predicts a brittle behaviour at low confining pressures, which switches to a semibrittle behaviour characterized by inelastic compaction followed by dilatancy at higher confining pressures. Model predictions are in close agreement with experimental results. The porosity range of applicability of the model is discussed and found to be 0-20%.

1. Introduction

Carbonates represent more than 60% of oil reservoir rocks, have been proposed as reservoirs for the geological sequestration of carbon dioxide and are crossed by faults zones (e.g. Armijo et al., 1992). Thus, understanding and predicting their mechanical behaviour is of great interest. Experimental studies have already been conducted on limestones (e.g. Heard, 1960, Baud et al., 2000, Vajdova et al., 2004). These studies have shown that depending on the confining pressure, samples can have a brittle or a ductile behaviour, even at room temperature. The brittle-ductile transition depends on grain size and porosity (Vajdova et al., 2004, Wong & Baud, 2012).

At low confining pressure, samples undergo an elastic compaction beyond which dilatancy takes place. Finally, the differential stress reaches a peak beyond which strain softening is occurring. This is typical of a brittle behaviour. Deformation at microscopic scale is accommodated by microcrack nucleation and/or propagation leading to their coalescence. At high confining pressure, an inelastic shear-enhanced compaction associated with strain hardening follows the elastic compaction (Baud et al., 2000). Yet, inelastic compaction is transient and volumetric strain reverses to dilatancy (Baud et al., 2000). These features involving macroscopically distributed deformation by both crystal plasticity (mechanical twinning and dislocation glide) and microcracking, and inducing a pressure dependent strength are typical of the semibrittle (ductile) regime as defined by Evans et al. (1990). In calcite, microplasticity is active at room temperature (e.g. Turner et al., 1954) but dislocations and twins can only slip in their plane. Micro-defects accumulate and no recovery process takes place. Localized residual stresses due to pile-ups can be sufficient to nucleate new microcracks (e.g. Wong, 1990) and thus induce dilatancy.

2. Material and methods

In this study, experiments were performed on Tavel limestone, a micritic microporous limestone. This rock is composed of coarse grained micrite particles (diameter $\sim 5 \mu\text{m}$) fused from one to another, leading to larger micritic aggregates (Vajdova et al., 2004).

The pressure vessel used is a conventional triaxial cell installed in the Laboratoire de Géologie at the École Normale Supérieure in Paris. During an experiment, the sample is first loaded isostatically up to a pressure of 20 MPa, which is kept constant at 20 MPa during heating to 70°C (~ 18 hours). Then, samples are loaded isostatically up to the desired confining pressure. Finally, the differential stress is applied by deforming the sample at a controlled strain rate of 10^{-5}s^{-1} . Axial and radial strains are measured with strain gauges. The volumetric strain is calculated as $\varepsilon_{\text{vol}} = \varepsilon_{\text{ax}} + 2\varepsilon_{\text{rad}}$, where ε_{ax} and ε_{rad} are the axial and radial strains, respectively.

3. Experimental observations of the mechanical behaviour

In this paper, compressive stresses and compactive strains are counted positive. Principal stresses will be denoted σ_1 and σ_3 , σ_1 being the highest principal stress and σ_3 the confining pressure, P_c . The differential stress $\sigma_1 - \sigma_3$ will be denoted Q and the mean stress $(\sigma_1 + 2\sigma_3)/3$ will be denoted P . Figure 1 (a) shows the differential stress as a function of axial strain, and Figure 1 (b) shows the effective mean stress versus volumetric strain for experiments performed at $P_c = 5, 20, 35, 55, 70$ and 85MPa. For $P_c < 55$ MPa, the observed features are typical of the brittle regime: i) samples undergo an elastic compaction until a point denoted C' (Wong et al., 1997), beyond which dilatancy takes place (Figure 1 b); ii) the differential stress reaches a peak, beyond which strain softening is occurring; iii) observation of the samples after deformation indicates that the deformation was localized in a shear fault. For $P_c \geq 55$ MPa, samples exhibit (1) an elastic compaction and (2) an inelastic shear-enhanced compaction associated with strain hardening beyond a critical stress denoted C^* (Baud et al., 2000). Yet, the inelastic compaction is transient and volumetric strain reverses from inelastic compaction to dilatancy beyond a critical stress denoted $C^{*'}$ (Wong et al., 1997). These features (i) involving macroscopically distributed deformation by microcracking, grain rotations and plasticity (dislocation creep, twinning) (e.g. Fredrich et al., 1989); (ii) leading to final axial strains lying in the range 3-5% at failure and (iii) inducing a pressure-dependent strength; are typical of the semibrittle (ductile) regime as defined by Evans et al. (1990). Thus, the brittle-ductile transition occurs at $35 \text{ MPa} < P_c \leq 55 \text{ MPa}$ in Tavel limestone.

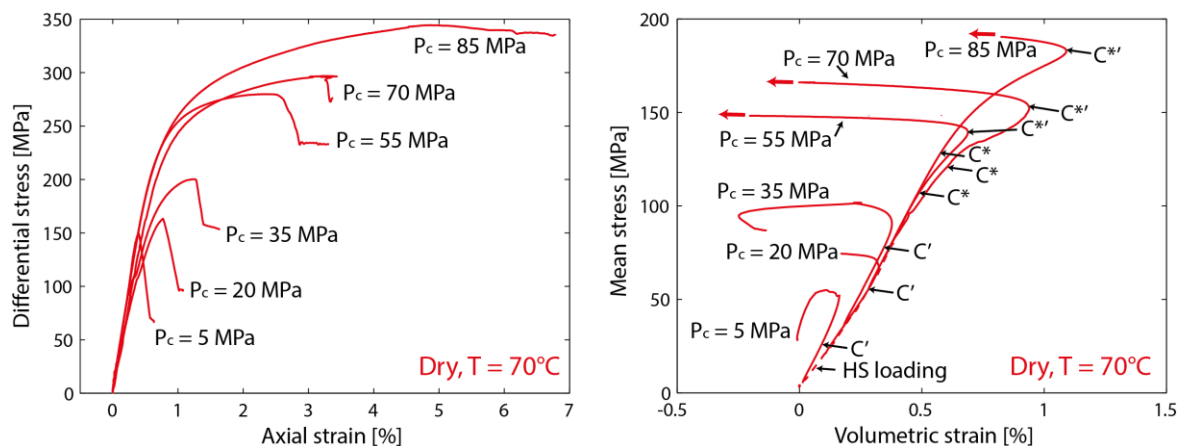


Figure 1: (a) Differential stress is plotted versus axial strain for all the constant strain rate deformation experiments. (b) Mean stress is plotted versus volumetric strain for the same constant strain rate experiments.

4. Derivation of the constitutive model

Porous limestones are heterogeneous in terms of microstructure (e.g. grain type and size,

porosity distribution, cementation), physical properties and mechanical behaviour, and key parameters are not easy to identify (Regnet et al., 2015a). In this model, we assume that the microstructure is characterized by (1) a matrix composed of pure calcite, (2) porosity made-up of equant pores and (3) cracks. Predicting the mechanical behaviour of limestones implies to embody all the possible micromechanisms. Thus, the derivation of the micro-mechanically motivated constitutive model includes five key steps: (i) derive the effective elastic moduli for the cracked porous medium to get the elastic strains, (ii) calculate the macroscopic strains related to crack growth of an array of interacting cracks, (iii) calculate the macroscopic strains related to dislocations from crystal plasticity, (iv) account for crack nucleation and growth from dislocation pile-ups, and (v) finally calculate the macroscopic stress evolution during constant strain rate loading:

(i) Elastic moduli of the medium containing spheroidal pores and cracks will vary as a function of its initial values and the evolutions of porosity and crack density (e.g. Fortin et al., 2007). Cracks are assumed to be randomly oriented.

(ii) We use Ashby & Sammis' (1990) approach to calculate the stress intensity factor K_I in a three-dimensional setting. Wing cracks are assumed to grow from pre-existing penny-shaped cracks and form an array of interacting cracks in an isotropic linear elastic surrounding medium subjected to compressive stresses (Figure 2a). Wings can grow from each end of the initial crack, parallel to the maximum principal stress. The faces of the initial crack can either slide with some friction characterized by a friction coefficient or open. Subcritical crack growth is not considered. Macroscopic strains related to crack growth are calculated via the work conjugate relation (Deshpande & Evans, 2008).

(iii) Plastic pore collapse is modelled using Duva & Hutchinson's (1984) calculation for the plastic deformation of a porous medium (Figure 2b). This macroscopic description is coupled with a microscopic description of the plasticity, through dislocation movements. We calculate the increase of dislocation density as the solid matrix deforms plastically.

(iv) A number of dislocations per pile-up is calculated from the dislocation density and a pile-up density. New crack nucleation is calculated with Wong's (1990) model (Figure 2c). Macroscopic strains due to new cracks is calculated via the work conjugate relation.

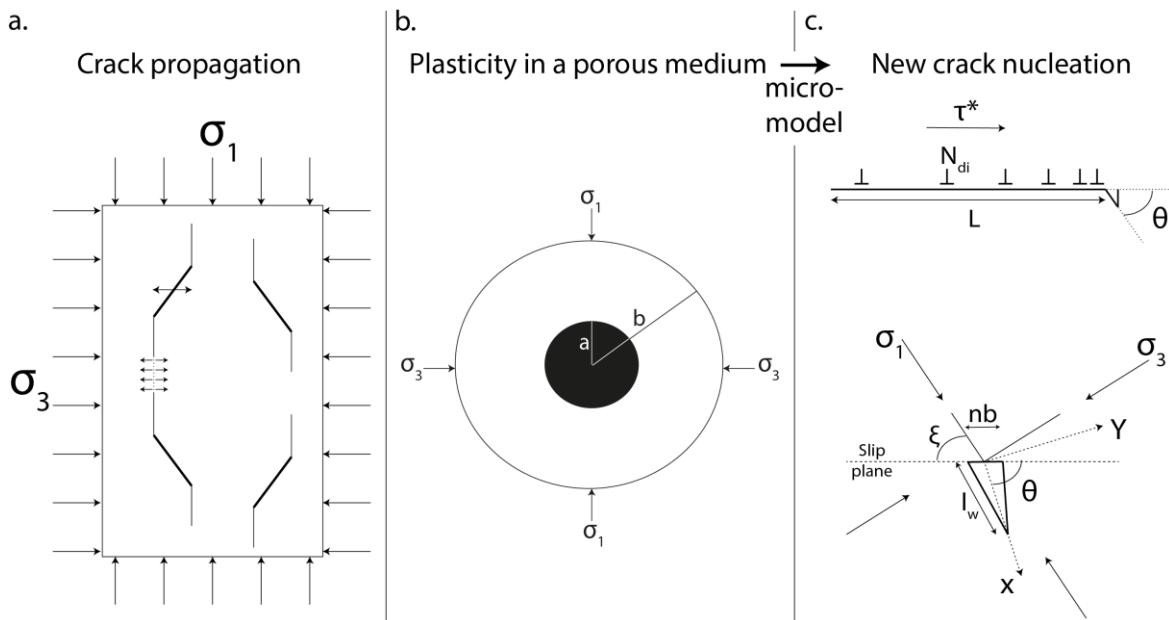


Figure 2: (a) Array of propagating wing cracks. (b) Plasticity around a pore, inducing plastic pore collapse. (c) Dislocation pile-ups induce new crack nucleations.

(v) The overall stress-strain curve of the porous material submitted to a constant strain rate is finally derived from the previous steps. Total strain is the sum of the elastic, the

crack-induced and the microplasticity-induced strains. During a short time dt , total strain $d\epsilon$ is:

$$d\epsilon = d\epsilon^e + d\epsilon^{\text{cracks}} + d\epsilon^{\text{mp}}, \quad (1)$$

where $d\epsilon^e$, $d\epsilon^{\text{cracks}}$ and $d\epsilon^{\text{mp}}$ are the elastic, crack and porous material microplastic strain increments, respectively. Total axial strain is $d\epsilon_{\text{ax}} = \dot{\epsilon}_{\text{ax}} dt$, where $\dot{\epsilon}_{\text{ax}}$ is the imposed constant axial strain rate. The crack and plastic axial strains are calculated with the work conjugate relation and the porous medium plasticity law, respectively. Then, the macroscopic axial stress increment $d\sigma_1$ is:

$$d\sigma_1 = E d\epsilon_1^e, \quad (2)$$

where E is the evolving Young modulus of the cracked porous medium and $d\epsilon_1^e$ the axial elastic strain increment. This incremental procedure is repeated to obtain the entire constitutive stress-strain relation.

5. Comparison with experimental data

Mean stress versus volumetric strain is shown in Figure 3a for experimental triaxial loading at various confining pressures. Predicted behaviour is reported in Figure 3b. Experimental and predicted stress-strain curves are very similar. At confining pressures strictly below 55 MPa, the predicted mechanical behaviour is brittle. At confining pressures equal or above 55 MPa, the predicted mechanical behaviour is characterized by elastic compaction, transient inelastic compaction, ultimately leading to dilatancy. The inferred predicted brittle-ductile transition occurs at a confining pressure between 35 MPa and 55 MPa, in the same range as the experimental value.

Below the brittle-ductile transition, the model reproduces the general trend of the deformation. Stress states C' and peak stresses are generally over estimated, which is probably due to a too small initial crack length. Dilatancy at rupture is overestimated by the model at $P_c = 35\text{MPa}$. However, predicted stress states C^* and $C^{*'}$ and related volumetric strains are very close to experimental ones. The onset of dilatancy is controlled by the pile-up density ρ_{pu} . Note however that the same value of ρ_{pu} is used for all model predictions whatever the confining pressure is. For the predictions shown here, $\rho_{\text{pu}} = 1.6 \times 10^8 \text{m}^{-2}$; which corresponds to about 1 pile-up over 15 grains of size $5\mu\text{m}$.

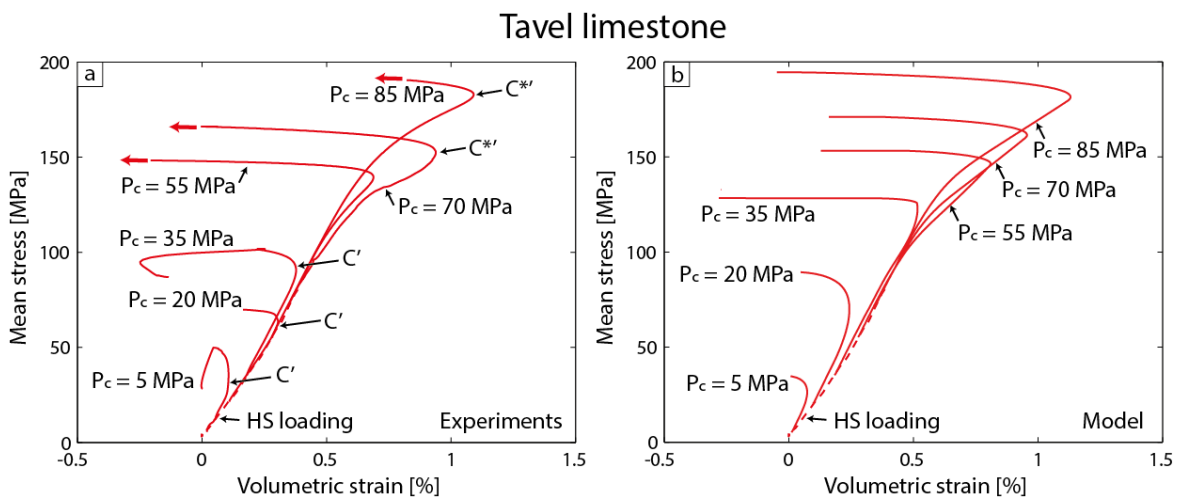


Figure 3: (a) Mean stress is plotted versus volumetric strain for all the constant strain rate experiments (as in Figure 1). (b) Corresponding mean stress versus volumetric strain model predictions.

6. Range of applicability of the model

Initial porosity is a key parameter that controls the deformation and failure modes of limestones (Vajdova et al., 2004). The model takes into account (1) the dilatancy due to crack development at low confining pressure and (2) the semibrittle behaviour characterized by (i) shear-enhanced compaction due to microplastic flow, (ii) switching to dilatancy because of local stress concentrations caused by pile-ups. To what extent can the model developed here be applied to various carbonate rocks? Up to what porosities is it relevant?

Baud et al. (2009) investigated systematically the micromechanics of compaction in two high porosity carbonates, Majella grainstone (porosity: 30%) and Saint-Maximin limestone (porosity: 37%). In both cases, grain crushing is the dominant mechanism of deformation beyond C^* . In Estailades limestone (porosity: 28%), Dautriat et al. (2011) showed that inelastic cataclastic compaction is coupled with an elastic wave velocity decrease due to grain crushing. Thus, the micromechanisms of deformation in Majella grainstone, Saint-Maximin and Estailades limestones are very different from the micromechanisms taken into account in the model developed in this study. The mechanical behaviour of high porosity limestones cannot be accounted for by the present model.

Baud et al. (2000) interpreted shear enhanced compaction in Solnhofen limestone (porosity 3%) as resulting from plastic collapse of spherical pores embedded in a solid matrix. For porosities lower than 15%, deformation beyond C^* in the semibrittle regime and inelastic pore collapse are controlled by plastic micromechanisms (dislocation slip processes, twinning) associated with some microcracking (Vajdova et al., 2004). It can be suggested that, as porosity increases, a transitional behaviour is likely to develop, and volumetric strain due to shearing and rotation of fragments becomes more important (e.g. Vajdova et al., 2012). The transition between shear-enhanced compaction controlled by crystal plasticity and grain crushing is likely to occur for a porosity of approximately 20% (Vajdova et al., 2004). Thus, the present model probably predicts adequately the stress-strain evolution for carbonates of porosity lower than 20%.

Compaction of porous rocks is known to be localized in many cases, as shown in sandstones by Mollema & Antonellini (1996) among many others. Baud et al. (2009) showed that compaction localization occurs in high porosity carbonates. This kind of phenomenon has not been considered in the present model because experimental results do not show localization for low porosity limestones.

7. Conclusions

The complex general trends of stress-strain relations of low-porosity limestones is reproduced by a model based on (1) brittle crack propagation, (2) a plasticity law for porous media with hardening and (3) crack nucleation due to dislocation pile-ups. The model is based on (i) three parameters relevant to the brittle behaviour (pre-existing crack length and density, sliding coefficient on these cracks), (ii) two parameters relevant to the micro-plastic flow in the solid non-porous medium (a reference strain rate and an initial yield stress), and (iii) a parameter characterizing the density of large pile-ups. Parameters relevant to the brittle behaviour can be determined from observations of the microstructure. The parameters relevant to the ductile behaviour are fitted to experimental data. Despite the limited number of parameters, the model adequately predicts a brittle behaviour at low confining pressures, which switches to a semibrittle behaviour characterized by inelastic compaction followed by dilatancy at higher confining pressures. Possible applications include predicting the complex rheology of porous limestones in various conditions, for example for reservoir management.

8. References

- Armijo, R., Lyon-Caen, H., & D., P. (1992). East-west extension and holocene normal-fault scarps in the hellenic arc. *Geology*, 20, 491–494.
- Ashby, M. & Sammis, C. G. (1990). The damage mechanics of brittle solids in compression. *Pure and Applied Geophysics*, 133, 489–521.
- Baud, P., Schubnel, A., & Wong, T.-f. (2000). Dilatancy, compaction, and failure mode in Solnhofen limestone. *Journal of Geophysical Research: Solid Earth*, 105(B8), 19289–19303.
- Baud, P., Vinciguerra, S., David, C., Cavallo, A., Walker, E., & Reuschlé, T. (2009). Compaction and failure in high porosity carbonates: Mechanical data and microstructural observations. (pp. 869–898).
- Dautriat, J., Gland, N., Dimanov, A., & Raphanel, J. (2011). Hydromechanical behavior of heterogeneous carbonate rock under proportional triaxial loadings. *Journal of Geophysical Research: Solid Earth (1978–2012)*, 116(B1).
- Deshpande, V. & Evans, A. G. (2008). Inelastic deformation and energy dissipation in ceramics: A mechanism-based constitutive model. *Journal of the Mechanics and Physics of Solids*, 56.
- Duva, J. & Hutchinson, J. (1984). Constitutive potentials for dilutely voided nonlinear materials. *Mechanics of materials*, 3(1), 41–54.
- Evans, B., Fredrich, J. T., & Wong, T.-F. (1990). The brittle-ductile transition in rocks: recent experimental and theoretical progress. *The Brittle-Ductile Transition in Rocks*, (pp. 1–20).
- Fortin, J., Guéguen, Y., & Schubnel, A. (2007). Effects of pore collapse and grain crushing on ultrasonic velocities and Vp/Vs. *Journal of Geophysical Research: Solid Earth*, 112(B8).
- Fredrich, J. T., Evans, B., & Wong, T.-F. (1989). Micromechanics of the brittle to plastic transition in Carrara marble. *Journal of Geophysical Research: Solid Earth*, 94(B4), 4129–4145.
- Heard, H. C. (1960). Chapter 7: Transition from brittle fracture to ductile flow in Solnhofen limestone as a function of temperature, confining pressure, and interstitial fluid pressure. *Geological Society of America Memoirs*, 79, 193–226.
- Mollema, P. & Antonellini, M. (1996). Compaction bands: a structural analog for anti-mode I cracks in aeolian sandstone. *Tectonophysics*, 267(1), 209–228.
- Paterson, M. S. & Wong, T.-f. (2005). *Experimental Rock Deformation - The Brittle Field*. Springer Verlag.
- Regnet, J., Robion, P., David, C., Fortin, J., Brigaud, B., & Yven, B. (2015a). Acoustic and reservoir properties of microporous carbonate rocks: Implication of micrite particle size and morphology. *Journal of Geophysical Research: Solid Earth*, 120(2), 790–811.
- Turner, F. J., Griggs, D. T., & Heard, H. (1954). Experimental deformation of calcite crystals. *Geological Society of America Bulletin*, 65(9), 883–934.
- Vajdova, V., Baud, P., & Wong, T.-F. (2004). Compaction, dilatancy, and failure in porous carbonate rocks. *Journal of Geophysical Research: Solid Earth*, 109(B5).
- Vajdova, V., Baud, P., Wu, L., & Wong, T. (2012). Micromechanics of inelastic compaction in two allochemical limestones. *Journal of Structural Geology*, 43(0), 100 – 117.
- Wong, T.-F. (1990). A note on the propagation behavior of a crack nucleated by a dislocation pileup. *Journal of Geophysical Research: Solid Earth*, 95(B6), 8639–8646.
- Wong, T.-f., David, C., & Zhu, W. (1997). The transition from brittle faulting to cataclastic flow in porous sandstones: Mechanical deformation. *Journal of Geophysical Research: Solid Earth*, 102(B2), 3009–3025.
- Wong, T.-F. & Baud, P. (2012). The brittle-ductile transition in porous rock: A review. *Journal of Structural Geology*, 44(0), 25 – 53.

Constitutive behaviour and microstructure

Strength, stability, and microstructure of simulated calcite faults sheared under laboratory conditions spanning the brittle-plastic transition

Berend A. Verberne (b.a.verberne@uu.nl), Johannes, H. P. de Bresser, André R. Niemeijer, Christopher J. Spiers
High pressure and –temperature laboratory, Utrecht University, Utrecht, The Netherlands.

ABSTRACT. Carbonate rocks form major hydrocarbon and geothermal reservoirs. However, induced and natural (micro)seismicity is commonplace in these rocks, posing various hazards. We investigate the fault-slip mechanisms active in simulated calcite (CaCO_3) faults under conditions spanning the entire crust. Shear tests were carried out at an effective normal stress of 50 MPa, at temperatures of 20 to 600°C, employing sliding velocities (v) of 0.1 to 10 $\mu\text{m/s}$. Results showed (unstable) v -weakening behaviour from ~80-100°C to ~550°C, but stable v -strengthening <80-100°C and >550°C. Using the post-test microstructure as a basis, plus a previously proposed micromechanical model, we show that these stability transitions are caused by changes in the (nano)granular flow processes accommodating shear. Our results imply that faults cutting carbonate rocks at depths >2-3 km are prone to exhibiting runaway slip hence earthquakes, consistent with widespread observations of (induced) seismicity at these depths in carbonate terrains (e.g. the Lacq gas field, France).

1. Introduction

Repetitive (micro)earthquakes on pre-existing faults are recurring slip instabilities thought to be analogous to the jerk sliding motion, or “stick-slip”, frequently observed in laboratory fault-slip experiments (*Brace & Byerlee, 1966*). For regular stick-slip to occur, the slipping contact must decrease in strength with increasing displacement rate, hence be velocity (v)-weakening, while the opposite case of v -strengthening leads to stable sliding (*Ruina, 1983*). This v -dependence of frictional strength is a material property of the sliding medium, which, in the case of natural faults, consists of accumulated granular wear material or “fault gouge”.

Carbonate rocks form over 60% of the world’s oil and gas reservoirs (*Agosta & Tondi, 2010*), and are frequently considered the most important targets for geothermal energy production (*Goldscheider et al., 2010*). However, induced (micro)seismicity associated with carbonate reservoir rocks is commonplace (e.g. *Maury et al., 1992*) and tectonically-active carbonate terrains are notably prone to destructive earthquakes (e.g. M_w 5.9 2012 Emilia and M_w 6.1 2009 L’Aquila, Italy). To investigate the seismogenic slip behaviour of faults in carbonate rocks, we conducted an experimental investigation on simulated fault gouge prepared from the dominant carbonate mineral, calcite (CaCO_3). Specifically, we aim to determine the strength and slip stability of our samples, at conditions relevant to the seismogenic zone, i.e. spanning the brittle-plastic transition. We use the post-test microstructure to study the physical processes controlling shear.

2. Materials & methods

Frictional shearing experiments were performed on ~1 mm thick layers of simulated calcite gouge prepared from pure CaCO_3 single crystals (Iceland Spar). The starting median grain size (d_{50}) of the sample powders measured 15 to 20 μm .

We employed the saw-cut, direct-shear as well as the ring-shear geometry (see *Verberne, 2015*). Saw-cut and direct-shear tests employed a sequentially stepped load-point displacement rate within the range from 0.1 to 10 $\mu\text{m/s}$, and were performed under

(lab-)dry or water-saturated conditions, at temperatures (T) of $\sim 18^\circ$ to 150°C , at an effective normal stress (σ_n^{eff}) of 50 to 53 MPa. In the case of water-saturated experiments, the pore fluid consisted of deionized water, which was pressurized to 10 MPa. The total displacement achieved in these tests measured 4 to 6 mm. Constant- v and v -stepping experiments in the ring shear were conducted in the range $0.1 \leq v \leq 100 \mu\text{m/s}$, at $\sigma_n^{\text{eff}} = 50$ MPa, at $T = 20^\circ$ to 600°C . Effective normal stress-stepping experiments were also performed in this temperature range, employing $20 \leq \sigma_n^{\text{eff}} \leq 140$ MPa, at fixed sliding velocities of 0.1 and $100 \mu\text{m/s}$. All ring shear tests were performed under water-saturated conditions, using deionized water, and pore fluid pressures ranging from 10 to 100 MPa. The total displacement in these experiments measured ~ 20 to 30 mm.

Sheared gouge layers were recovered and subjected to micro- and nanostructural investigation using light and electron microscopy. Recovered samples were resin-impregnated and then sectioned after hardening, and/ or examined as loose fragments collected fresh after an experiment. In the case of sectioning, thin slices ~ 5 to $30 \mu\text{m}$ in thickness were prepared in an orientation normal to the shear plane.

3. Results

Mechanical data

Saw-cut as well as direct-shear tests showed that the apparent coefficient of friction ($\mu = \text{shear stress} / \text{effective normal stress}$, or $\tau / \sigma_n^{\text{eff}}$) at steady-state, determined at $v = 1 \mu\text{m/s}$, measured ~ 0.6 to 0.8 (Fig. 1). Regardless of the shear geometry employed, wet or (nominally) dry, all experiments showed a transition from stable, v -strengthening slip to potentially unstable, v -weakening slip at $T \geq 80$ to 100°C . Experiments showing v -weakening frequently showed stick-slip behaviour (e.g. at 150°C in Fig. 1).

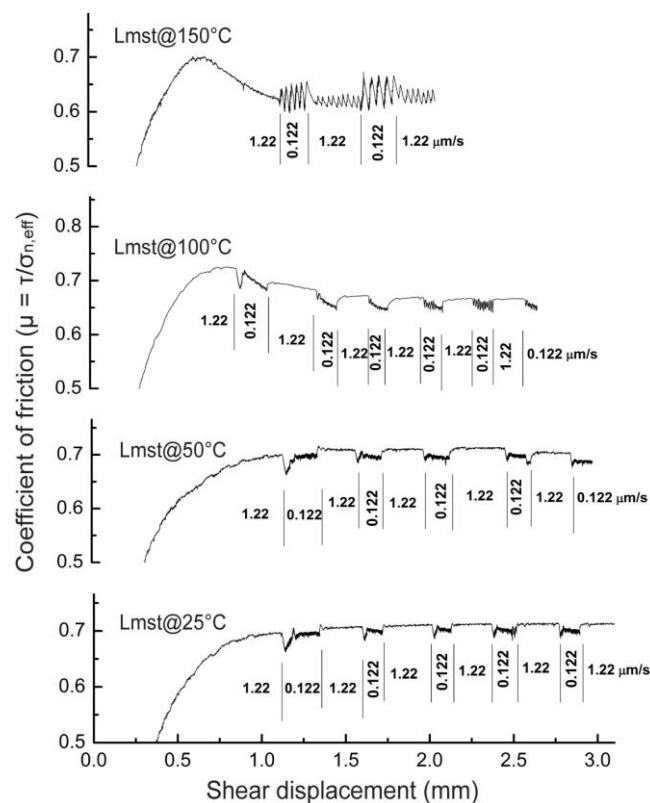


Figure 1. Saw-cut shear (friction) tests conducted at an effective normal stress of 53 MPa. Shear displacement rates (sequentially stepped in each test) and temperatures (25, 50, 100, and 150°C) as indicated (taken from Verberne, 2015).

The velocity dependence of shear strength (Γ) was quantified using the expression

$$\Gamma = \frac{\tau_{i+1} - \tau_i}{\sigma_n^{eff} (\ln(v_{i+1}) - \ln(v_i))} = \frac{\Delta \tau}{\sigma_n^{eff} \Delta \ln(v)} \quad (1)$$

where the subscript i refers to sliding before a step in displacement rate. Positive values of Γ indicate v -strengthening, and negative values v -weakening behaviour. The value of Γ was determined from each velocity step, and plotted against temperature for the direct- and ring shear tests (Figs 2a, b). Despite minor differences in the magnitude of Γ between dry and wet tests, all data suggest a transition from v -strengthening ($\Gamma > 0$) to v -weakening ($\Gamma < 0$) behaviour above temperatures of 80 to 100°C (Fig. 2a). Importantly, this demonstrates that the presence of (pressurized) pore water is not crucial to produce v -weakening behaviour.

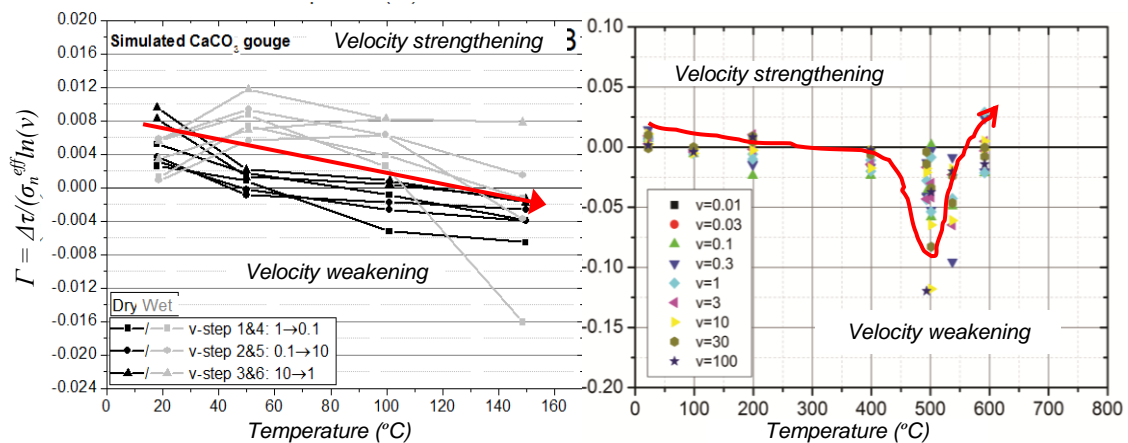


Figure 2. Plot of the sliding velocity dependence of strength (Γ) against temperature, for a) dry (black symbols) and wet (grey symbols) direct shear tests and b) ring shear tests.

Ring shear tests conducted up to 550°C continued to display v -weakening behaviour, until a transition to stable v -strengthening slip occurred at 550 to 600°C (for $v = 0.1$ to 10 $\mu\text{m/s}$, see Fig. 2b). Effective normal stress stepping experiments conducted in the temperature range from 20 to 600°C, employing $30 \leq \sigma_n^{eff} \leq 100$ MPa and $1 \leq v \leq 100$ $\mu\text{m/s}$ consistently showed a linear dependence of shear stress (τ) upon increasing σ_n^{eff} (Verberne, 2015), suggesting frictional sliding behaviour.

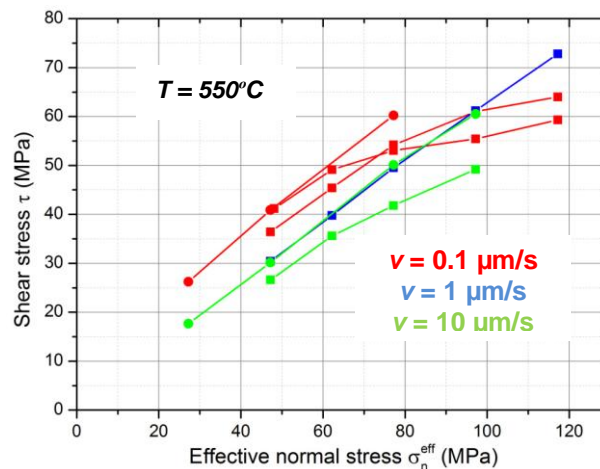


Figure 3. Plot of shear stress against effective normal stress for experiments conducted at 550°C, employing (constant) sliding velocities (v) of 0.1 (red symbols), 1 (blue symbols), and 10 (green symbols) $\mu\text{m/s}$.

To investigate the dependence of shear stress upon increasing effective normal stress at constant v , near the transition from v -weakening to v -strengthening (Fig. 2b), σ_n^{eff} -stepping tests were conducted, employing $20 \leq \sigma_n^{eff} \leq 140$ MPa and a constant temperature of $\sim 550^\circ\text{C}$. This showed a linear dependence of τ upon increasing σ_n^{eff} when using (constant) $v \geq 1 \mu\text{m/s}$ (Fig. 3). However, at $v = 0.1 \mu\text{m/s}$, this showed a flattening-off of the τ vs. σ_n^{eff} curve at σ_n^{eff} -values above 65 to 80 MPa (Fig. 3).

Microstructures

All sections prepared from experiments which were conducted in the temperature range from 20° to 200°C showed a pattern of shear strain localization into ultra-fine grained, boundary-parallel and inclined shear bands (Fig. 4a). The shear bands display a strong, uniform, optical birefringence, and optical extinction, indicative of a crystallographic preferred orientation (CPO).

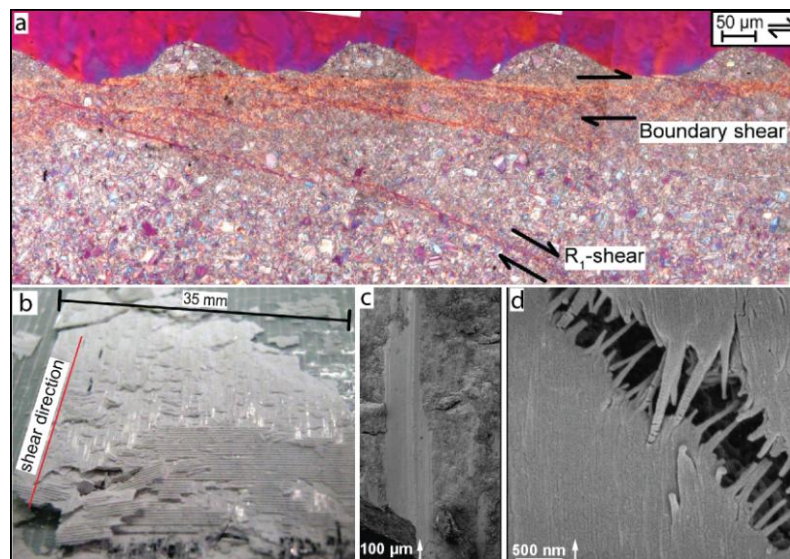


Figure 4. Microstructures of simulated calcite fault gouge sheared at $\sigma_n^{eff} = 50$ MPa, at $T = 20$ to 200°C , employing $v = 0.1$ to $10 \mu\text{m/s}$. a) Photomosaic of transparent light micrographs. b) Sheared gouge sample displaying shiny (“mirror-like”) slip surfaces. c and d) SEM micrographs of a shiny surface patch. Image in (d) shows a crack cutting the patch in (c).

Internally split sheared gouge fragments recovered from the boundary shear display striated, highly-reflective (shiny) surface patches, aligned parallel to the shear direction (Fig. 4b). SEM investigation of the boundary shear, or principal slip zone (PSZ), showed that it comprises a porous ($\phi = 20\text{-}30\%$), sheet-like volume of partially sintered, ~ 100 nm nanocrystalline spherules, with embedded dense, planar patches of aligned, ~ 100 nm-wide nanospherule chains or fibres that constitute the shiny slip surfaces (Figs. 4c, d). Towards higher temperatures, i.e. in gouge layers recovered from velocity-stepping experiments performed at 400° to 600°C using $v = 0.1$ to $100 \mu\text{m/s}$, localized slip in a PSZ was accompanied by more distributed deformation, involving grain size sensitive (GSS, diffusion creep) and/ or grain size insensitive (GSI, dislocation creep) processes.

However, the effect of sliding velocity on microstructural evolution at high temperature is important. Samples recovered from experiments performed at conditions close to the higher temperature transition from v -weakening to v -strengthening behaviour (i.e. at $\sim 550^\circ\text{C}$), which employed constant $v = 0.1 \mu\text{m/s}$, showed a microstructure indicating distributed or homogeneous deformation (Fig. 5a). By contrast, samples recovered from experiments conducted under the same conditions, but using $v = 100 \mu\text{m/s}$, showed the development of a single, ~ 30 to $40 \mu\text{m}$ wide PSZ (Fig. 5b).

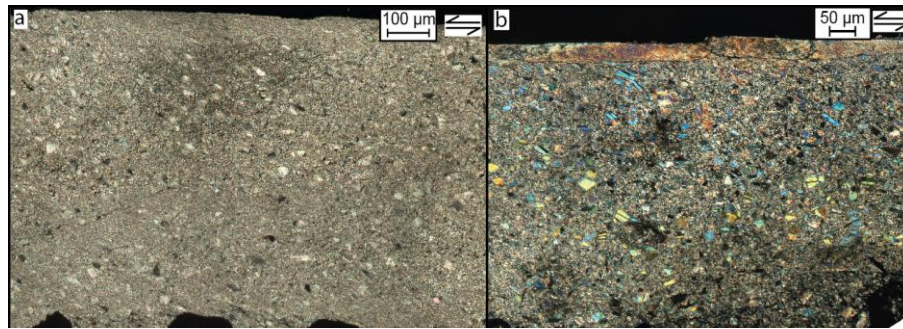


Figure 5. Microstructures recovered from ring shear tests conducted at a temperature of 550°C and effective normal stress of 50 MPa, at constant sliding velocities (v) of a) 0.1 $\mu\text{m/s}$ and b) 100 $\mu\text{m/s}$.

4. Discussion - Microphysical mechanism

The Niemeijer-Spiers model for shear deformation of granular materials (Fig. 6; Niemeijer & Spiers, 2007; Den Hartog & Spiers, 2013), which involves competition between dilatation by granular flow vs. creep-controlled compaction, predicts qualitatively similar trends in frictional behaviour to the trends with increasing temperature observed in the present mechanical data (e.g. Fig. 2b & Fig. 6d). The model predicts three regimes of sliding-velocity-dependent granular flow (Regimes A, B and C in Fig. 6), i.e. critical state granular flow (Regime A, v -strengthening), granular flow involving balanced dilatation and compaction (Regime B, v -weakening), and non-dilatant (frictional-)viscous flow (Regime C, v -strengthening). Under v -weakening conditions, creep-controlled compaction is fast enough to impart higher strength at lower sliding velocities.

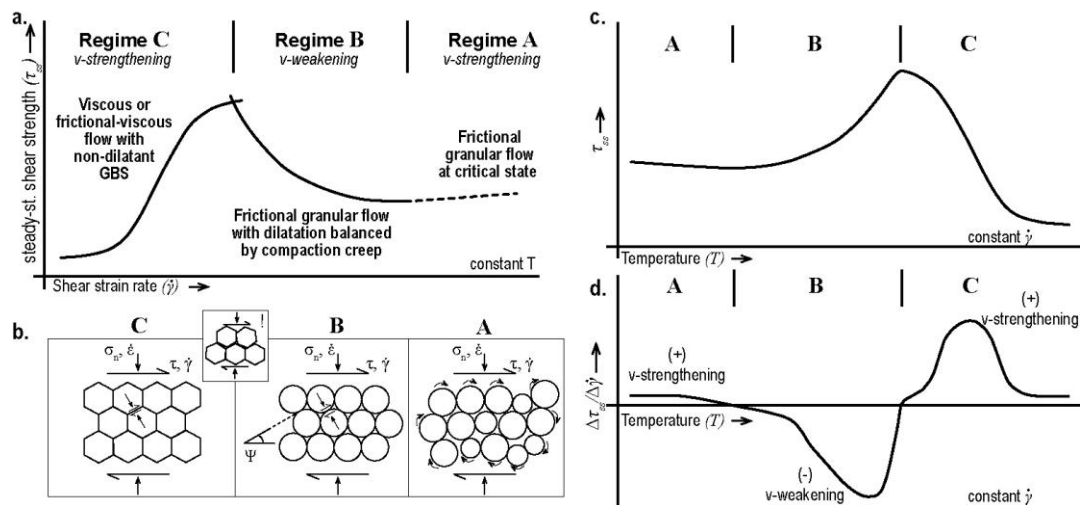


Figure 6. a) The dependence of steady-state shear strength (τ_{ss}) on shear strain rate ($\dot{\gamma}$), as predicted by the Niemeijer-Spiers model. Increasing temperature translates this curve rightwards. b) Schematic model microstructures characterizing each shear Regime in (a). Ψ = dilatation angle. c) The evolution of τ_{ss} and (d) $\dot{\gamma}$ with temperature, as qualitatively predicted by the model (cf. Fig. 2b). For more detail on the model see Niemeijer & Spiers (2007) or else Verberne (2015).

At relatively low temperatures in our experiments (20 to 200°C), a mechanism of nanogranular flow with partial accommodation by diffusive mass transport is proposed to have controlled shear deformation. The transition from v -strengthening to v -weakening slip, i.e. from Regime A to B in Fig. 6, occurs due to enhanced diffusive mass transfer rates at elevated temperatures. At temperatures of 400 to 600°C, intracrystalline plasticity and dynamic recrystallization of the bulk gouge material start to play a significant role, especially at the lower slip velocities employed. The transition from v -weakening to v -

strengthening behaviour observed at 550 to 600°C is interpreted as a transition from (localized) frictional sliding, involving balanced dilatant granular flow and creep-controlled compaction (Regime B), to (more distributed) non-dilatant, viscous/ plastic shear flow involving GSS and/ or GSI (creep) deformation processes (Regime C).

4. Conclusions

We investigated fault slip processes active in simulated calcite fault gouge, under conditions spanning the brittle-plastic transition in the Earth's crust. Our results show a transition from (stable) velocity (v)-strengthening to (potentially) unstable v -weakening at ~80-100°C, and back to v -strengthening around ~550-600°C. Using the shear gouge micro-/nanostructure as a basis, we showed that gouge shear is controlled by a competition between dilatation (granular flow) and creep-controlled compaction, which, when balanced, can result in (potentially) unstable v -weakening behaviour.

Our results have important implications for (stimulation of) oil, gas, and/ or geothermal energy production from carbonate rock reservoirs. Assuming a constant effective normal stress of 50 MPa and a geotherm of ~20-30°/km, faults cutting carbonate rocks in the range from ~3- or 4 km to ~18-24 km depth can be expected to be inherently unstable, potentially leading to runaway fault slip and (micro)earthquake nucleation. This is consistent, for example, with observations of abundant seismicity associated with gas production from carbonate oil and gas reservoirs, such as the Lacq field (France) (Bardainne *et al.*, 2008). Also, seismicity at depths of 15-20 km where carbonates are inferred to be present is common in the southern Apennines (Italy) (Boncio *et al.*, 2007).

5. References

- Agosta, F., & Tondi, E. (2010). Faulting and fracturing of carbonate rocks: New insights into deformation mechanisms, petrophysics and fluid flow properties. *J. Struct. Geol.* 32, 1185-1186.
- Bardainne, T., Dubos-Sallée, N., Sénéchal, G., Gaillot, P., & Perroud, H. (2008). Analysis of the induced seismicity of the Lacq gas field (Southwestern France) and model for deformation. *Geophys. J. Int.* 172, 1151-1162.
- Boncio, P., Mancini, T., Lavecchia, G., & Selvaggi, G. (2007). Seismotectonics of strike-slip earthquakes within the deep crust of southern Italy: Geometry, kinematics, stress field and crustal rheology of the Potenza 1990-1991 seismic sequences (M_{max} 5.7). *Tectonophysics* 445, 281-300.
- Brace, W. F., & Byerlee, J. D. (1966). Stick slip as a mechanism for earthquakes. *Science* 153, 990-992.
- Den Hartog, S. A. M., and Spiers, C. J. (2013). Influence of subduction zone conditions and gouge composition on frictional slip stability of megathrust faults. *Tectonophysics* 600, 75-90.
- Goldscheider, N., Mádl-Szőnyi, Erőss, A., & Schill, E. (2010). Thermal water resources in carbonate rock aquifers. *Hydrogeol. Int.* 18, 1303-1318.
- Maury, V. M. R., Grasso, J.-R., & Wittlinger, G. (1992). Monitoring of subsidence and induced seismicity in the Lacq Gas Field (France): the consequences on gas production and field operation. *Eng. Geol.* 32, 123-135.
- Niemeijer, A. R., and Spiers, C. J. (2007). A microphysical model for strong velocity weakening in phyllosilicate-bearing fault gouges. *J. Geophys. Res.* 112, B10405, doi:10.1029/2007JB005008.
- Ruina, A. L. (1983). Slip instability and state variable friction laws. *J. Geophys. Res.* 88, B12, doi:10.1029/JB088iB12p10359.
- Verberne, B. A. (2015). Strength, stability, and microstructure of simulated calcite faults sheared under laboratory conditions spanning the brittle-plastic transition. *Utrecht Studies in Earth Sciences* 90, Ph.D. Thesis, 300 pp.

SIGNIFICANCE OF MINERALOGY FOR HYDRO-MECHANICAL BEHAVIOUR OF CLAYS

Wiebke Baille (wiebke.baille@rub.de), Tom Schanz
Ruhr-Universität Bochum, Chair of Foundation Engineering, Soil and Rock Mechanics, D-44780 Bochum, Germany.

Snehasis Tripathy
Geoenvironmental Research Centre, School of Engineering, Cardiff University, Newport Road, Cardiff, CF24 3AA, Wales, UK.

ABSTRACT. The influence of mineralogy and micro-structural properties on the hydro-mechanical behaviour of kaolinite, illite and montmorillonite clay was investigated over a wide range of stress and suction. A specially fabricated high stress oedometer device was used to investigate the volume change of the clays for initially saturated and compacted saturated condition up to 25 MPa. The tests on compacted saturated specimens include swelling pressure measurements during wetting of initially compacted specimens at fully confined condition followed by subsequent one-dimensional compression. The influence of mineralogy on the water retention and volume change due to an increase in suction at zero applied mechanical stress was investigated and analysed using suction stress approach. The observed macroscopic behaviour could be explained by the fabric of the clays at the respective loading paths. The experimental void ratio-stress relationships are compared to their theoretical counterparts obtained from various approaches based on diffuse double layer theory; their applicability was discussed.

1. Introduction

Clays of different mineralogical composition are used for various geotechnical and geoenvironmental engineering applications, such as road and dam constructions and fills. They are used in near-surface waste containment facilities consisting of a cover and a bottom liner. Bentonites have been proposed as a suitable barrier and backfilling material for the underground storage of nuclear and toxic waste in many countries (Pusch 1977, Dixon & Gray 1985, Herbert & Moog 2002) due to their high swelling capability, low permeability upon imbibing water or electrolytes, and low ion diffusivity (Pusch 1982).

According to the specific applications of the clays given above, they are in either initially compacted unsaturated or initially saturated state (slurry). Unsaturated clayey soils possessing clay minerals exhibit swelling or compression when inundated with fluids. Similarly, saturated clays composed of these clay minerals usually undergo significant volume decrease during the drying process and due to an increase in the surcharge. Considering the application of bentonite in an underground waste disposal, the relevant magnitude of applied mechanical stress on the clay can be in the order of up to 20 MPa. The changes in void ratio, water content and degree of saturation induced by mechanical or hydraulic loading depend on the clay mineral type. The various clay mineral types are characterised by typical microstructural features and physicochemical properties, such as specific surface area, cation exchange capacity, and type and amount of exchangeable cations present. The macroscopic volume change behaviour is strongly related to these features. Identification of the relevant micromechanical mechanisms and the prediction of the engineering behaviour of clays of different mineralogy based on these mechanisms and the physicochemical properties is still a challenge.

The work presented herein has covered the following aspects: (1) experimental determination of the basic and physicochemical properties of the clays studied; (2) experimental determination of the applied stress-void ratio relationships for oedometric

loading condition for initially saturated clays and compacted saturated clays for maximum applied mechanical stresses up to 25 MPa (Baille et al. 2010); (3) experimental investigation of the influence of mineralogy on the water retention behaviour of the clays including measurement of water content, void ratio and degree of saturation due to an increase in suction; (4) microstructural investigation of the clays at selected stress states; (5) assessment of the void ratio-stress relationships based on considerations using the diffuse double layer theory and comparison to the experimental relationships for the various initial specimen conditions and loading paths; (6) assessment of the influence of mineralogy on effective stress in clays using suction stress approach (Baille et al. 2014).

2. Materials

The clays used in this study are Calcigel bentonite, NX illite, and Spergau kaolin, each of them comprised predominantly of one of the main clay mineral groups (montmorillonite, illite, and kaolinite). The main properties of the clays studied are presented in Table 1, the measured mineralogical composition is shown in Table 2. Details regarding the methods used for determination of the material properties can be found in Baille (2014).

Table 1. Properties of the clays studied (Baille 2014).

	Calcigel bentonite	NX illite	Spergau kaolin
Particle density, ρ_s (Mg/m ³)	2,80	2,71	2,67
Liquid limit, w_L (%)	178	77,6	53,4
Plastic limit, w_P (%)	56,1	30,1	32,3
Plasticity index, I_P (%)	121,9	47,5	21,1
Shrinkage limit, w_s	11,8	25,7	31,3
Activity (-)	2,2	0,5	0,4
Optimum water content, w_{opt} (%)	40,0	35,9	22,8
Maximum dry density, $\rho_{d,Pr}$ (Mg/m ³)	1,19	1,29	1,50
Cation exchange capacity, CEC (meq/100g)	74	26	8
Specific surface area, A_s (m ² /g)	525	154	28
Weighted average valency, v (-)	1.93	2.00	1.92

Table 2. Quantitative mineralogical composition of the clays studied.

	Montm.	Quartz	Illite	Kaolinite	Calcite	Dolomite	Sum
Calcigel bentonite	78	4	8	2	3,5	3	98,5
NX illite			77	10	12		99
Spergau kaolin		8	16	76			100

3. Swelling pressures and one-dimensional compressibility behaviour of clays at large pressures

Most of the studies on the volume change behaviour of bentonites due to the application of mechanical stress were for initially saturated clays with initial water content greater than the liquid limits of the clays (Bolt 1956, Olson & Mesri 1970, Sridharan & Rao 1973, Marcial et al. 2002, Di Maio et al. 2004). The compressibility behaviour of compacted bentonites after the swelling pressure is developed under confined conditions is a near field situation and has not been studied so far. The tests on compacted saturated specimens include swelling pressure measurements at confined condition due to hydration of initially compacted unsaturated specimens followed by subsequent one-dimensional compression up to 25 MPa at oedometric condition. The loading regime was applied also to Spergau kaolin and NX illite for comparison reason.

Figure 1 shows the compression–decompression line of the initially saturated specimens and the swelling pressures of the compacted specimens for the clays studied. Several compacted specimens with varying initial dry density were tested for each of the clays (Baïlle 2014).

The swelling pressure data points of Spergau kaolin specimens CK 3, CK 4, CK 5 and CK 6 remained on or close to the decompression path of specimen SK, either slightly above (CK 2, CK 5) or below (CK 3, CK 4 and CK 6) (Fig. 1a). The points of the compacted NX illite specimens CI 1 to CI 6 (Fig. 1b) are mainly located between the compression and the decompression line of the initially saturated specimen SI. The swelling pressure–void ratio data for the compacted saturated bentonite specimens CB 1 to CB 10 remained distinctly below that of the compression path of SB 3 (Fig. 1c). On the other hand, the swelling pressure data points remained either above or below that of the decompression path of SB 3.

The test results clearly showed that the void ratio–stress relationships are strongly dependent on the stress paths and the initial compaction conditions that significantly influence the fabric and structure of the clay. The complete discussion including compression–decompression paths of the compacted saturated specimens, the compression and decompression indices, and the calculated coefficients of consolidation and coefficients of permeability can be found in Baïlle et al. (2010) for Calcigel bentonite and in Baïlle (2014) for Spergau kaolin and NX illite.

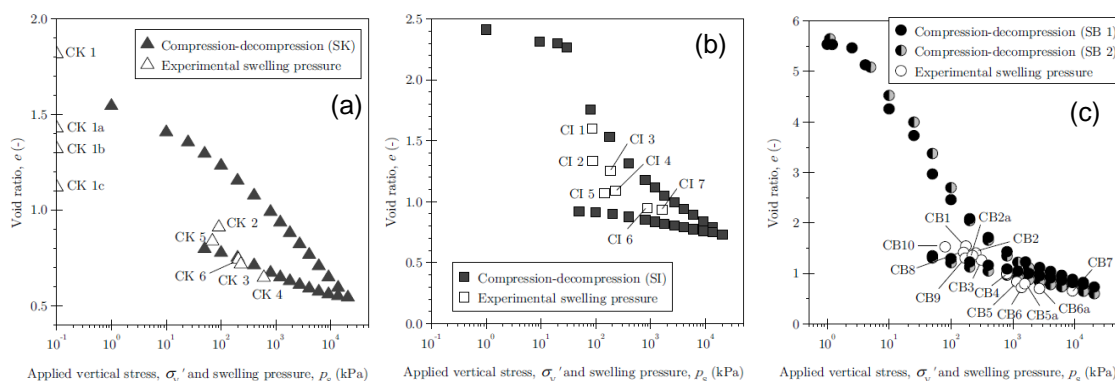


Figure 1. Applied vertical stress and swelling pressure–void ratio relationships: (a) Spergau kaolin, (b) NX illite, (c) Calcigel bentonite.

4. Effect of loading type and mineralogy on volume change of clays

The volume change behaviour of the initially saturated clays was investigated. The initially saturated specimens were subjected to either a change in total axial stress in k_0 condition or an increase in suction.

Figure 2 provides a comparative illustration of the fabric of the three clays at initially saturated state. Figure 3(a) shows the suction–water content SWCCs and Figure 3(b) the applied suction vs. void ratio plots of the clays studied. Suction was applied using osmotic method and vapour equilibrium technique. In Figure 3(c) the applied vertical stress vs. void ratio plot is shown to compare it with the suction tests. The shapes of the suction–water content SWCCs and suction vs. void ratio responses of Calcigel bentonite and NX illite were very similar; that is, a monotonic decrease in the water content and void ratio occurred with an increase in the applied suction, whereas a decrease in the water content for Spergau kaolin was abrupt between suctions of about 2.0 to 7.0 MPa. The residual zone was distinct for Spergau kaolin, whereas it was indistinct for Calcigel bentonite and NX illite. For applied suctions <2.0 MPa, the equilibrium void ratios and water contents of the clays were arranged according to the liquid limits of the clays in the order of Calcigel bentonite, NX illite, and Spergau kaolin. For applied suctions >2.0 MPa, the ordering of the suction vs. void ratio plots changed, with the void ratios of Spergau kaolin remaining distinctly greater than the void ratios of NX illite and Calcigel bentonite.

Spergau kaolin and NX illite mineral crystals form a rigid type of fabric dominated by frictional contacts between the aggregates. The quasi-crystals of Calcigel bentonite are flexible in nature. The internal layer-redistribution within the quasi-crystals during suction increase, i.e., the change of the ratio between interlayer pores and pores between the quasi-crystals, together with the flexible nature of the quasi-crystals enable the Calcigel bentonite to drain its water out of the pores while staying saturated up to large suction values, leading to smaller void ratios as compared to Spergau kaolin and NX illite in case of applied suction increase.

The mechanical loading of 2 to 20 MPa vertical applied stress caused a tight compression of the fabric of Spergau kaolin, where only negligible pore space was discernable. The anisotropic nature in the oedometer tests as compared to the isotropic suction loading lead to a particle re-orientation and a smaller global void ratio as compared to the other clays. Re-orientation was not pronounced for Calcigel bentonite

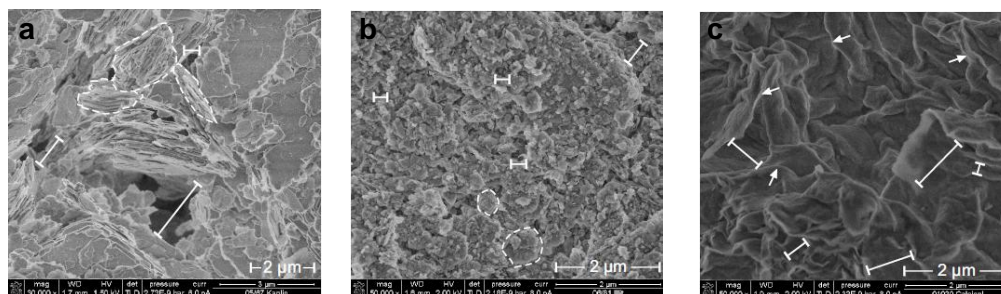


Figure 2. ESEM photomicrographs at initially saturated state corresponding to $1,1w_L$ [dashed lines: boundary of an aggregate; arrows: point towards quasi-crystals forming walls of large pores; bars: extension of voids]: (a) Spergau kaolin; (b) NX illite; (c) Calcigel bentonite.

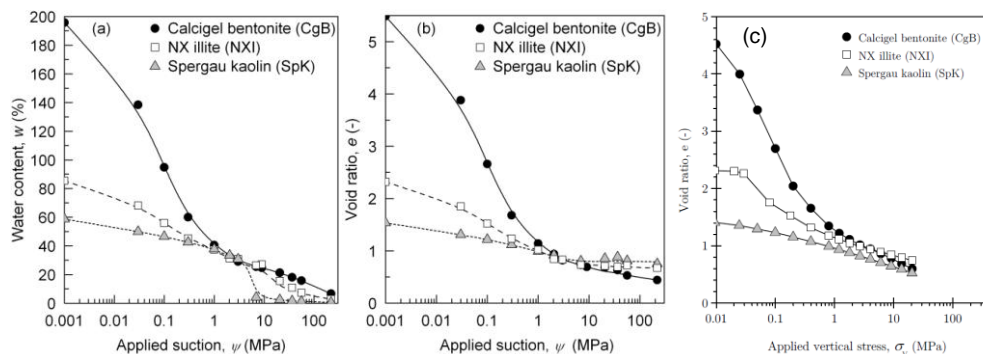


Figure 3. (a) suction–water content soil-water characteristic curves (SWCCs), (b) suction vs. void ratio plot (Baille et al. 2014) and (c) applied vertical stress vs. void ratio of the clays studied.

during mechanical loading. The intraaggregate pore space of the stable, rigid NX-illite aggregates, which are not affected by large suctions and stresses leads to a higher global void ratio of NX illite as compared to Calcigel bentonite for both types of loading.

Figure 4 shows, for each clay, the void ratio changes due to an increase in the applied vertical stress in one-dimensional compressibility tests (applied vertical stress σ vs. void ratio e) and an increase in the applied suction on the void ratio of the clays in suction tests. For comparison, the suction–water content SWCCs of the clays are also shown in the relevant plots in Fig. 4. The void ratio axes in Fig. 4 (see right-side y axes) were scaled to match the water contents on the left-side y axis for fully saturated conditions.

For any clay, the oedometer compression path and the suction vs. void ratio response were very similar within a range of applied vertical stress or applied suction (i.e., up to about 2.0–4.0 MPa for Spergau kaolin, 10.0–20.0 MPa for NX illite, and up to about 21.0 MPa for Calcigel bentonite). This indicates that an applied suction and vertical

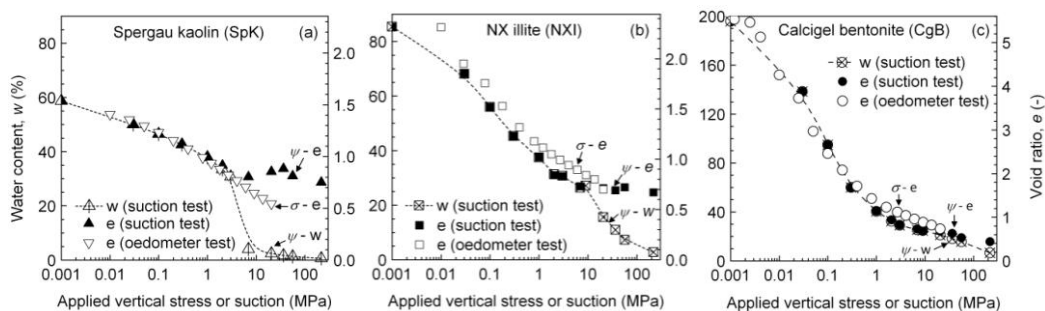


Figure 4. Void ratio changes due to one-dimensional loading and suction loading for (a) Spergau kaolin, (b) NX illite, and (c) Calcigel bentonite (Baille et al. 2014).

stress of equal magnitude caused similar volume changes of the clays within the specified stress ranges. The results are in agreement with the test results for various clays reported in the literature (Fleureau et al., 1993; Tripathy et al., 2010). For suctions less than the noted values, the suction–water content SWCC and suction vs. void ratio response for any clay were similar and the clays remain saturated. At high applied suctions, the suction vs. void ratio plots of Spergau kaolin and NX illite remained distinctly above that of the corresponding applied vertical stress–void ratio curves and suction–water content SWCCs. Deviations of the suction vs. void ratio responses from the corresponding saturated compression paths can be considered for approximately determining the AEVs of soils (Tripathy et al., 2010).

5. Application of physico-chemical theories

The application of classical diffuse double layer theory was found to be relevant to some extent for Calcigel bentonite, but not relevant for NX illite and Spergau kaolin. Classical diffuse double layer calculations were found to represent reasonably well the experimental data in limited ranges of considered dry densities or applied stresses and suctions of Calcigel bentonite. The overestimation of swelling pressures for lower dry densities and the overestimation of void ratio in the low stress range of the one-dimensional consolidation test and in the low suction range of the water retention tests is attributed to the nonideal particle arrangement in the compacted specimens and the slurry specimens. The significant deviations in calculated swelling pressures at high dry densities and applied stresses are attributed to the hydration forces manifest as strong repulsion in the swelling pressure test and as a greater resistance to volume change in the oedometer test. It is important to note that diffuse double layer forces are not the single operating force within the clay–water system. Thus, the use of approaches based of

diffuse double layer only can not be expected to represent the full range of observed phenomena, especially for small interparticle distances (Tripathy et al. 2006).

6. Conclusions

In the present work, the influence of the mineralogy and the related physicochemical and microstructural properties on the hydromechanical behaviour of various clays possessing significant proportion of one of the clay minerals from kaolinite, illite, and montmorillonite over a wide range of stress and suction was found to be extremely relevant. The test results clearly showed that the void ratio-stress relationships are strongly dependent on the stress paths and the initial compaction conditions that significantly influence the fabric and structure of the clay. Theoretical approaches considering the physico-chemical properties of the clays based on diffuse double layer theory were shown not to fully represent the observed behaviour, especially at small interparticle distances and high stresses, other mechanisms than diffuse-double layer forces need to be taken into account.

7. References

- Baille, W., Tripathy, S., Schanz, T (2010). Swelling pressures and one-dimensional compressibility behaviour of bentonite at large pressures. *Applied Clay Science*, 48(3):324-333, doi:10.1016/j.clay.2010.01.002.
- Baille, W. (2014). Hydro-Mechanical Behaviour of Clays – Significance of Mineralogy. Phd-Thesis, Ruhr-Universität Bochum, Schriftenreihe Grundbau, Boden- und Felsmechanik, Heft 53.
- Baille, W. Tripathy, S. and Schanz, T. Effective stress in clays of various mineralogy. *Vadose Zone Journal*, 13(5), 2014, doi:10.2136/vzj2013.06.0112.
- Bolt, G. (1956). Physico-chemical analysis of the compressibility of pure clays. *Géotechnique* 6(2), 86–93.
- Di Maio, C., Santoli, L. & Schiavone, P. (2004). Volume change behaviour of clays: the influence of mineral composition, pore fluid composition and stress state. *Mechanics of Materials* 36, 435–451.
- Dixon, D. & Gray, M. (1985). The engineering properties of buffer material. Technical Report TR-350, Fuel Waste Technology Branch, Whiteshell Laboratories., Pinawa, Man.
- Fleureau, J.-M., Kheirbek-Saoud, S., Soemitro, R. & Taibi, S. (1993). Behaviour of clayey soils on drying-wetting paths. *Can. Geotech. J.* 30, 287–296.
- Herbert, H.-J. & Moog, H. (2002). Untersuchungen zur Quellung von Bentonit in hochsalinaren Lösungen. Technical Report GRS-179, Gesellschaft für Anlagen und Reaktorsicherheit (GRS) mbH, Berlin.
- Marcial, D., Delage, P. & Cui, Y. J. (2002). On the high stress compression of bentonites. *Canadian Geotechnical Journal* 39(4), 812–820.
- Olson, R. E. & Mesri, G. (1970). Mechanisms controlling the compressibility of clay. *ASCE Journal of the Soil Mechanics and Foundations Division* 96(6), 1863–1878.
- Pusch, R. (1977). Required physical and mechanical properties of buffer masses. Technical report 33, KBS, Swedish Nuclear Fuel Supply Co., Stockholm.
- Pusch, R. (1982). Mineral–water interactions and their influence on the physical behavior of highly compacted na bentonite. *Can. Geotech. J.* 19, 381–387.
- Sridharan, A. & Rao, G. (1973). Mechanisms controlling volume change of saturated clays and the role of the effective stress concept. *Géotechnique* 23(3), 359–382.
- Tripathy, S., Kessler, W., Schanz, T (2006). Determination of interparticle repulsive pressures in clays. In G.A. Miller, C.E. Zapata, S.L. Houston, and D.G. Fredlund, eds., *Proc. of the Fourth International Conf. on Unsat. Soils*, p. 2198-2209, Carefree, Arizona, USA, April 2nd-6th 2006.
- Tripathy, S., R. Bag, and H.R. Thomas. 2010. Desorption and consolidation behaviour of initially saturated clays. In: E.E. Alonso and A. Gens, editors, *Proceedings of the 5th International Conf. on Unsat. Soils*, Barcelona, Spain. 6–8 Sept. 2010. CRC Press, Boca Raton, FL. p. 381–386.

QUANTITATIVE COMPARISON BETWEEN THE CRACK APERTURES, STRAINS AND MICROSTRUCTURE IN TOURNEMIRE CLAY-ROCKS

Anne-Laure Fauchille¹ (anne.laure.fauchille@univ-poitiers.fr), Stephen Hedan¹, Dimitri Prêt¹, Valéry Valle², Justo Cabrera², Philippe Cosenza¹

¹University of Poitiers, CNRS UMR 7285 IC2MP, HydrASA, Poitiers, France.

²University of Poitiers, CNRS UPR 3346 Institut PPRIME, FuturoscopeChasseneuil, France.

³DEI-SARG Department, Institute for Radiological Protection and Nuclear Safety, Fontenay-aux-Roses, France.

ABSTRACT

The aim of this study is to compare quantitatively the influence of the microstructure on the strain and crack aperture intensity in Tournemire clay-rocks. In the laboratory, a clay-rock sample was submitted to a desiccation process in a waterproof box. One camera has taken images of a small zone of 5.5x4.1mm². The images were analysed by digital image correlation to obtain in-plane strain fields and local crack aperture values. After the desiccation process, the same small zone was analysed under a scanning electron microscope to obtain a map of its microstructure. The proportion of clay-matrix and hard grains were locally quantified. At the study scale, the preliminary results show: a) there is a non-bijective relationship between the proportion of clay-matrix and the 2D strains, and b) the local aperture of desiccation cracks seems to be higher at the interface between a hard grain zone and a clayey zone.

1. Introduction

The clay-rocks are an interesting medium to nuclear waste disposal at great depth because of their mechanical and microstructural properties. Nevertheless, a significant cracking due to a desaturation process of the argillaceous medium is observed on the gallery walls of the Underground Laboratory of Tournemire (Aveyron, France). This desiccation cracking takes part in the so called excavation damaged zone (EDZ). The initiation and extension of the EDZ are governed by different parameters such as the material anisotropy, the initial stress field, the geometry of the gallery, the mineralogy and so on (Bossard et al., 2002, Charpentier et al., 2004, Tsang et al., 2005; Blüming et al, 2007). The desiccation cracking is organised in a network of sub-horizontal cracks parallel to the bedding planes and spaced out 64 to 100 mm (Cabrera et al, 2001, Hedan et al, 2014), and a vertical network which shows more complex orientations. The mean crack aperture of these cracks is correlated with the relative humidity in the gallery (Hedan et al, 2014, Bailly et al, 2014). In the laboratory, the sub-horizontal desiccation cracks are located in the clay matrix next to hard grain heterogeneities such as a high local proportion of coarse grains or a high concentration of large grains of quartz and carbonates (Fauchille et al, 2014). At different scales, the majority of desiccation cracks are in the same direction than the bedding planes. Moreover, the desiccation deformation of clay rocks is usually really higher perpendicularly to the bedding planes (Valès et al, 2004, Pham et al, 2007, Guillon et al, 2012, Wang 2012). Consequently, these results demonstrate a close relationship between the deformation and cracking behaviour, and the microstructure of clayey rocks. During desiccation, some authors interpreted the high deformations of clay rocks by high proportions of clay matrix and the low deformations by high proportions of coarse grains (Montes 2002, Wang 2012). However, these observations were qualitative. The aims of this paper are a) to measure the in-plane deformation and cracking behaviour of a clay rock sample submitted to a

desiccation path and b) to study the relationship between these experimental results and the 2D microstructure with a quantitative approach.

2. Geological Setting and Sampling

The Tournemire Underground Laboratory (URL) of the French Institute for Radioprotection and Nuclear Safety (IRSN) is located in a Mesozoic marine basin on the southern limit of the Causse du Larzac. The sample used in this study is a cub of 20x20x20 mm³ extracted from the drill FD90 five meters deep (out the EDZ) in the East96 gallery (excavated in 1996). It comes from decimeter samples (d=80mm, L=200 mm) between 4.20 and 4.40 meters, where the rock is considered as saturated and kept away from EDZ. The sample was taken in an undisturbed zone. The mineralogical composition of the rock shows that clay minerals represent about 20-50 wt% (kaolinite, illite, interstratified illite/smectite), quartz about 10-20 wt %, carbonates about 10-30 wt% (calcite, dolomite, siderite), and sulphides 2-7 wt% (pyrites) (Cabrera et al. 2001). One face of the sample is finely polished with silicon carbide and diamonds products to delete relief artefacts under SEM and to have a good contrast for DIC.

3. Experimental Setup and Methods

3.1. Experimental Setup

The experimental setup is composed of a plastic water and airproof box in which humidity and temperature conditions are controlled. Relative humidity is controlled by saline solutions and temperature by an air-conditioning unit at 22°C. The box contains a RH/T sensor (Testo© 175H1), a precision balance (ADAM© PGW 753e) and a magnetic agitator for saline solutions. The agitation is controlled by an electric point and imposed for 2 min over 15 min to maintain a constant temperature. A camera (IDS µEye SE) takes images of five millions of pixels (2560x1920 pixels) every two minutes, of one sample's face of 5.5x4.1 mm² with a spatial resolution of 2.2µm.pixel⁻¹. A spot of 400W lights up the sample while the camera taking an image to avoid a disruption of the temperature. This spot is located a few meters far from the experimental box.

The sample was saturated for two months with a relative humidity of 98%. Then, it was submitted to a desiccation process during 10.3 days between 98 to 33% of relative humidities, corresponding to close extreme RH values observed in the tunnel of Tournemire (from 100% to 30%).

3.2. The Digital Image Correlation

- Classical digital image correlation
In geomechanics, the DIC technique allows the strain localization in geomaterials (Desrues et al., 1985), detection of crack positions and the calculation of the crack aperture in clay rocks (Hedan et al., 2014). It consists in recording images during a physical transformation as mechanical or hydric loadings. The images are composed of pixels and each one is represented by a grey level between 0 and 255 (8-bit). The method is based on the comparison of small areas (subsets) of grey levels between two images, in order to obtain the local displacement fields, and then the strain fields by a derivative of the displacements fields. In this study, the in-plane principal deformations ε_1 and ε_2 were used to be compared to the microstructure. The subsets are 64x64 pixels (140.8x140.8µm²) with a precision of 0.1 pixel (0.22µm).

- The H-DIC algorithm
The H-DIC algorithm (X-correl software) was used in this paper to detect the crack position and to calculate the aperture of the desiccation cracks (Valle et al, 2015). It allows the detection of displacement discontinuities to characterize the location of

desiccation cracks on the small zone. The crack aperture was calculated by subtracting the extrema of displacements on both sides of the crack in an area of 5x3 pixels just around the crack. Other sizes of areas were also tested (not shown, see Fauchille, 2015).

3.3. The Scanning Electron Microscopy

After the desiccation process, the surface of the small zone which was recorded by DIC was analysed under SEM with back-scattered electrons. A mineral map of the surface of the small zone was investigated as form of a mosaic image of 8806x6606 pixels with a resolution of $0.625\mu\text{m}\cdot\text{pixel}^{-1}$. The drift of the electron beam (displacement, rotation, deformation and grey levels) was considered to superimpose the strain fields to the microstructure. From the mineral map, the hard grains and the clay matrix were discriminated with the software $\mu\text{PHASEmap}$ (Prêt et al. 2010 a,b). Then the local surface proportion of clay matrix and hard grains were calculated in same domains than DIC domains used to calculate the strains, to be superimposed and compared.

In this paper, the study scale is the mesoscopic scale because the grains and the clay matrix are well discriminated (same scale system than Robinet, 2008).

4. Preliminary Results and Comments

4.1. Comparison between the strain intensity and microstructure

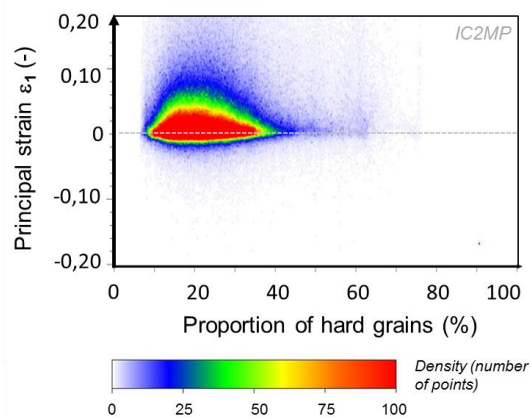


Figure 1. Principal strain ε_1 vs. the proportion of hard grains in the small zone.

The local principal strains ε_1 and ε_2 were superimposed on the local proportion of hard grains. The results were similar for ε_1 and ε_2 , so Figure 1 represents only the results for ε_1 . It reveals there is a high variability of strain values from -0,04 to 0,20, with an important concentration of values between -0,01 and 0,04 (red part in Figure 1). At the study scale, a low proportion of hard grains (from 8 to 40%), in other words a high proportion of clay matrix (from 60 to 92 %), does not correspond only to high strains but to very variable strains.

At the microscopic scale, Wang et al, (2013, 2014) explained the different desiccation strain intensity of Callovo-Oxfordian clay rocks by different proportions of clay matrix and hard grains, while considering a high proportion of clays causes higher deformations. In clay materials and at different scales, different deformation behaviour during a desiccation path are usually interpreted by different proportions of clay matrix (Montes et al, 2004, Yigzaw 2009, Wang 2012).

In our experiment conditions, our study reveals that there is not a bijective relationship between the intensity of ε_1 and the proportion of hard grains and clay matrix at the mesoscopic scale.

4.2. Comparison between the crack aperture and microstructure

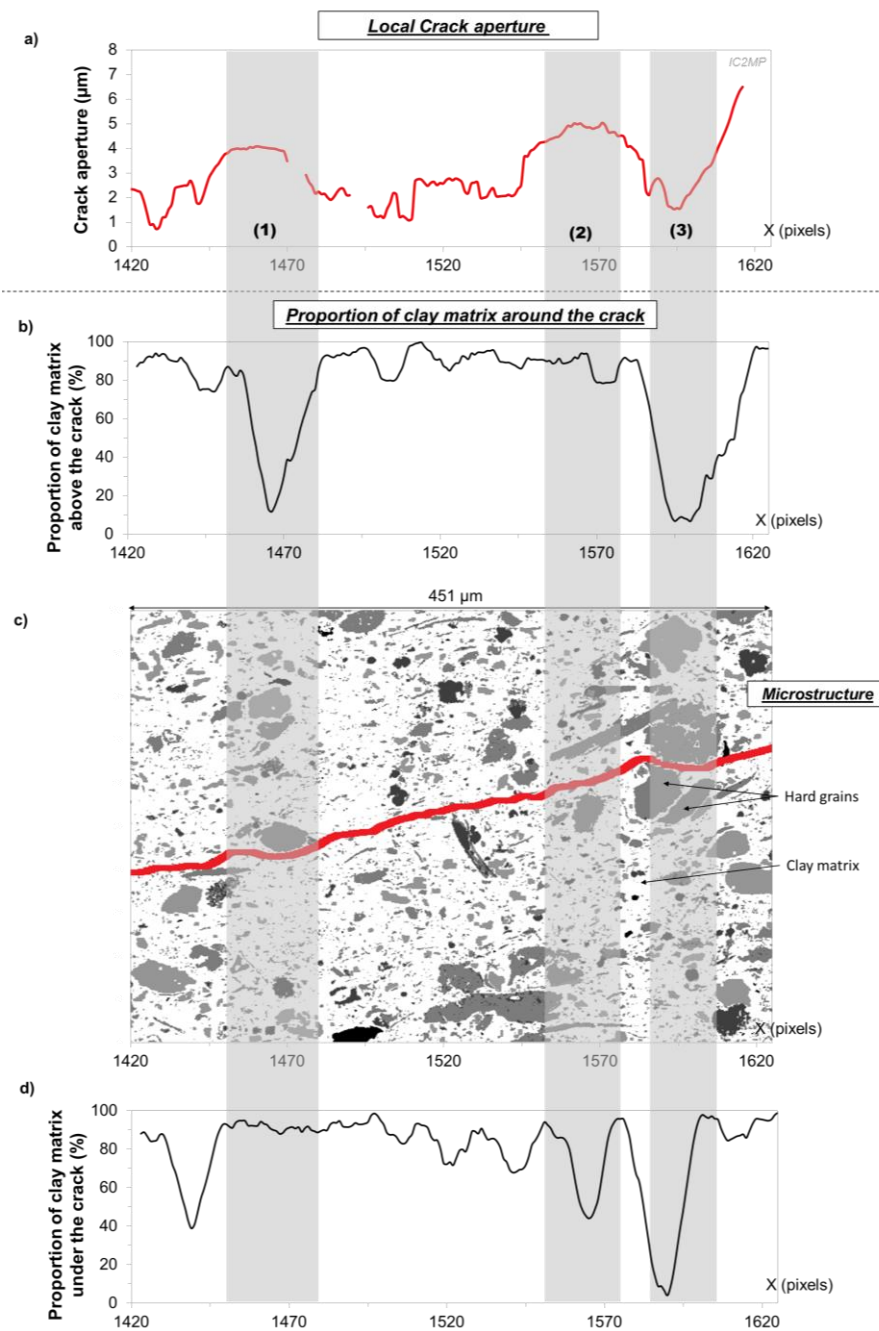


Figure 2. a) Crack aperture vs the X coordinates, b) proportion of clay matrix above the crack vs. the X coordinates, c) map of the microstructure, d) proportion of clay matrix under the crack vs. the X coordinates.

The local crack aperture was compared to the local proportion of clay matrix along a desiccation crack of 205 pixels length (451 μm) (Figure 2) located in the small zone of the sample. The clay matrix proportion is calculated on areas of 90 pixels (22x19,8 μm^2) perpendicular to the crack. This calculation is repeated along the crack and for each side of the crack. Other sizes of successive areas were also tested (not shown, see Fauchille, 2015). The crack aperture and the profiles of the clay matrix proportion are represented along the X coordinates of the zone (Figures 2a, b and d).

Figure 2a reveals that the local crack aperture is heterogeneous at the study scale, with values between 0.5 to 7 μm . The proportion of clay matrix is also heterogeneous above and under the crack (Figure 2b to d).

In two domains (Figure 2, grey part (1) for $X=1455$ to 1480 pixels, and grey part (2) for $X=1555$ to 1580 pixels), the local crack aperture increases significantly where there is an interface between a clayey zone and a hard grain zone. For the first domain, such an interface is characterized by a clay matrix proportion of 13% above the crack and 92% under the crack. For the second domain, the clay matrix proportions are respectively 88% and 45% above and under the crack. In a third domain (Figure 2, grey part (3) for $X=1585$ -1610), the crack aperture is very weak with a minimum of 1.5 μm . Large hard grains are just next to the crack (Figure 2c) so the clay matrix proportion is very low on both sides of the crack with values up to 8% above the crack and 6.5% under the crack (Figures 2b and d). This interface between large and coarse grains could restrict the crack opening during the desiccation process.

Nevertheless, the crack analysed here also presents other weak apertures, such as between $X=1480$ to 1510 pixels or for $X<1430$ pixels, whereas the proportion of clay matrix is higher than 80% on either sides of the crack.

5. Conclusions and Prospects

An experimental setup coupling DIC and SEM methods was used in this study to compare quantitatively the in-plane strains, crack apertures and the 2D microstructure during a desiccation path. At the mesoscopic scale, that is to say where the clay matrix and the hard grains are well distinguished, a simple relationship between the desiccation crack aperture, the strain intensity and the microstructure is not obvious. Contrary to the literature, the results obtained in this study focused on the fact that a high proportion of clay matrix is not correlated to a high deformation or a high crack aperture and vice versa. However, the interface between clayey and rich hard grain zone seems to be correlated to a local crack opening because of an important incompatibility of local deformation. To improve the knowledge about the link between deformation, cracking and microstructure in clayrocks, other microstructural parameters should be integrated to next studies such as the local proportion of swelling clays minerals and observations in 3D should be necessary.

Aknowledgments

The authors would like to express their acknowledgment to the NEEDS-MIPOR program (Nucléaire, Energie, Environnement, Déchets, Société-MilieuxPOReux) and to the French Institute for Nuclear Safety and Radioprotection (IRSN) for supporting and funding this work. They are also grateful to M. Pascal Touvenet, M. Pascal Rogeon, M. Claude Laforest and M. Frédéric Limousin for their technical help.

6. References

- Bailly, D., Matray, J.M., Abadou, R., (2014). Temporal behavior of a ventilated claystone at the Tournemire URL: Cross-spectral analyses focused on daily harmonics, *Engineering Geology* 183, 137-158.
- Blüming, P., Bernier, F., Lebon, P., Martin, C.D., (2007). The Excavation-Damaged Zone in clay formations - Time-dependent behaviour and influence on performance assessment. *Phys. Chem. Earth* 32, 588-599.
- Bossard, P., Meier, M.P., Moeri, A., Trick, T., Major, J.C., (2002). Geological and hydraulic characterisation of the excavation disturbed zone in the Opalinus Clay of the Mont Terri Rock Laboratory. *Eng. Geol.* 66(1-2), 19-38.

- Cabrera, J., Beaucaire, C., Bruno, G., De Windt, L., Genty, A., Ramambasoa, N., Rejeb, A., Savoye, S., Volant, P., (2001). Projet Tournemire : Synthèse des Résultats des Programmes de Recherche 1995/1999. *IRSN Report*.
- Charpentier, D., Mosser-Ruck, R., Cathelineau, M., Guillaume, D., (2004). Oxidation of Mudstone in a Tunnel (Tournemire, France): Consequences for the Mineralogy and Chemistry of Clays Minerals. *Clay Minerals* 39, 135-149.
- Desrues, J., Lanier, J., Stutz, P., (1985). Localization of the deformation in tests on sand sample. *Eng. Fract. Mech.* 21(4), 909-921.
- Fauchille, A.L., Hedan, S., Prêt, D., Valle, V., Cabrera, J., Cosenza, P., (2014). Relationships between desiccation cracking behavior and microstructure of the Tournemire clay rock by coupling DIC and SEM methods. *Proceedings of IS-Cambridge*, Geomechanics from Micro to Macro 1-3 Sept. 2014, (2), 1421-1424.
- Fauchille, A.L., (2015). Déterminismes microstructuraux et minéralogiques de la fissuration hydrique dans les argilites de Tournemire : apports couples de la pétrographie quantitative et de la corrélation d'images numériques, *PhDthesis*, University of Poitiers (France).
- Guillon, T., Giot, R., Giraud, A., Armand, G., (2012). Response of Callovo-Oxfordian claystone during drying tests : unsaturated hydromechanical behaviour, *Acta Geotechnica*, 7, 313-332.
- Hedan, S., Fauchille, A. L., Valle, V., Cabrera, J., & Cosenza, P. (2014). One-year monitoring of desiccation cracks in Tournemire argillite using digital image correlation. *Int. J. Rock Mech. Min. Sci.*, 68, 22-35.
- Montes-H., H.G., Duplay, J., Martinez, L., Escoffier, S., Rousset, D., (2004). Structural modifications of Callovo-Oxfordian argillite under hydration/dehydration conditions. *Ap. Clay Sc.* 25, 187-194.
- Pham, Q.T., Vales, F., Malinsky, L., Nguyen, M.D., Gharbi, H., (2012). Effects of desaturation-resaturation on mudstone, *Physics and Chemistry on the Earth* 32, 646-655.
- Robinet, J-C. (2008). Minéralogie, porosité et diffusion de solutés dans l'argilite du Callovo-Oxfordien de Bure (Meuse/Haute-Marne, France) de l'échelle centimétrique à millimétrique. PhD thesis, University of Poitiers, France.
- Tsang, C.F., Bernier, F., Davies, C., (2005). Geohydromechanical processes in the Excavation Damaged Zone in crystalline rock, rock salt, and indurated and plastic clays - In the context of radioactive waste disposal. *Int. J. of Rock Mech. and Min. Sci.* 42(1), 109-125.
- Valès, F., Nguyen Minh, D., Gharbi, H., Rejeb, A., (2004). Experimental study of the influence of the degree of saturation on physical and mechanical properties in Tournemire shale (France). *App. Clay Sci.* 26, 197-207.
- Valle, V., Hedan, S., Cosenza, P., Berdjane, M., Fauchille, A-L., (2015). Digital Image Correlation Development for the Study of Materials Including Multiple Crossing Cracks. *Experimental Mechanics* 55, 379-391.
- Wang, L., (2012). Micromechanical experimental investigation and modeling of strain and damage of argillaceous rocks under combined hydric and mechanical loads. *Ph-D Thesis*, Ecole Polytechnique, Palaiseau (France).
- Wang, L., Bornert, M., Chanchole, S., Yang, D.S., Héripré, E., Tanguy, A., Caldemaison, D., (2013). Microscale experimental investigation of the swelling anisotropy of the Callovo-Oxfordian argillaceous rock. *Clay Minerals* 48, 391-402.
- Wang, L., Bornert, M., Héripré, E., Yang, D.S., Chanchole, S., (2014). Irreversible deformation and damage in argillaceous rocks induced by wetting and drying. *Journal of Applied Geophysics* 107, 108-118.
- Yigzaw, Z.G., (2009). Analyse des processus de retrait-gonflement des sols argileux en réponse à des sollicitations hydriques cycliques, Rôle de la microstructure. *PhDthesis*, Ecole Nationale Supérieure des Mines de Paris.

Multiscale modelling and analysis

DEVELOPMENT AND APPLICATION OF A MULTISCALE MODELLING APPROACH FOR HYDROMECHANICAL COUPLING

Bram van den Eijnden^{1,2,4} (a.p.vandeneijnden@tudelft.nl), Pierre Bésuelle^{2,4}, René Chambon², Frédéric Collin⁴

¹Andra, 1-7 rue Jean Monnet, 92298 Châtenay-Malabry, France

²Univ. Grenoble Alpes, 3SR, 38000 Grenoble, France

³CNRS, 3SR, 38000 Grenoble, France.

⁴ArGEnCo dept, Univ. of Liège, 4000 Liège, Belgium.

ABSTRACT. The work summarized in this paper concerns the development and application of a multiscale modelling approach for the application in the study of the excavation damaged zone. In a first part, a finite element squared (FE²) method is developed in the framework of computational homogenization. Two scales are identified in this method; a macroscale continuum with second gradient paradigm and a microscale capturing the microstructure of the material. First order computational homogenization allows the derivation of homogenised response to the kinematical loading of a microstructural REV, providing a macroscale constitutive relation from the microscale computations. The application of the method in simulations of biaxial compression tests and gallery excavations demonstrates the capability of the method to derive complex material behaviour including strain localisation, material anisotropy and complete history dependency from a micromechanical formulation.

1. Introduction

This paper presents some of the aspects and principles of both the development and the application of the extension of the finite element squared (FE²) method to hydromechanical coupling. In FE² computations, a macroscale boundary value problem is solved by means of the finite element method, for which the constitutive relation at the integration points is derived from simulations of the material behaviour at a microscopic scale on which the material shows a microstructure. This microscale simulation is performed by means of representative elementary volumes (REVs) for which the BVPs are solved by a finite element approach, hence the term FE². A schematics of the presented model is given in Figure 1, showing the scheme of passing the (gradients of) displacements u_i and fluid pressure p to the microscale to derive the stress σ and (flux of) fluid mass responses \vec{m} and \dot{M} .

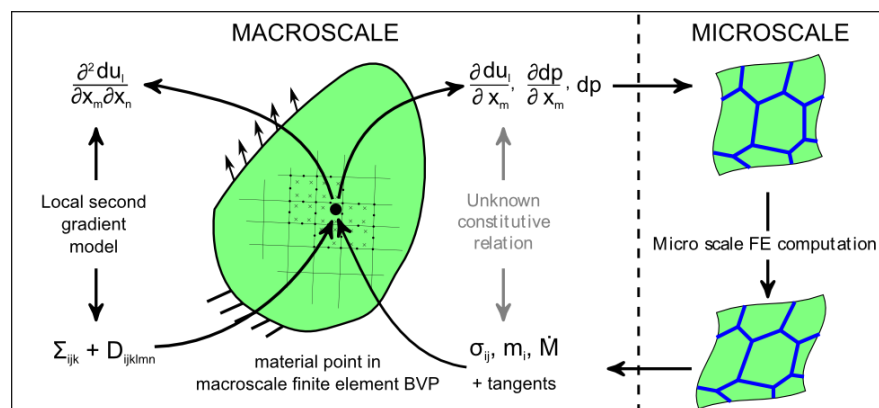


Figure 1. Schematic representation of the FE² method for hydromechanical coupling (van den Eijnden, 2015)

A local second gradient model is introduced at the macroscale as a phenomenological relation to ensure mesh objectivity when material softening and strain localization phenomena are simulated.

In this work the macroscale field equations will be presented (Chapter 1), followed by the microscale model for the material microstructure (Chapter 2) and the framework of computational homogenization (Chapter 3). The application of the model is presented (Chapter 4).

2. A macroscale poromechanical continuum with local second gradient paradigm

On the macroscale, a poromechanical continuum with HM coupling in a saturated porous medium is defined. For assessing material softening and localization phenomena in a finite element method without losing the objectivity of the mesh, a local second gradient paradigm (Chambon et al. 2001; Collin et al. 2006) is used for regularization. For the mechanical balance equations, this leads to the introduction of the double stress Σ with components Σ_{ijk} as a dual to the gradient of microkinematical gradient \mathbf{v} , which in local second gradient models is enforced to the second gradient of displacement. The balance equation for any kinematically admissible variation of displacement u_i^* is written as

$$\int_{\Omega} \left(\sigma_{ij} \frac{\partial u_i^*}{\partial x_j} + \Sigma_{ijk} \frac{\partial^2 u_i^*}{\partial x_j \partial x_k} \right) d\Omega - \int_{\Gamma} \left(\bar{t}_i u_i^* + \bar{T}_i \frac{\partial u_i^*}{\partial x_j} n_j \right) d\Gamma = 0 \quad (1)$$

with σ the Cauchy stress and \bar{t} and \bar{T} the boundary traction related to the first and second gradient parts. To solve this equation in a finite element method, without relying on higher continuous elements, the constraint on \mathbf{v} is weakened by means of Lagrange multipliers (Chambon et al. 2001). The balance equation for the fluid phase remains classical. For fluid mass flux \bar{m} and fluid mass density M , the balance equation for any kinematically admissible variation of pore pressure p^* is written as

$$\int_{\Omega} \left(m_j \frac{\partial p^*}{\partial x_j} - \dot{M} p^* \right) d\Omega - \int_{\Gamma} \bar{q} p^* d\Gamma = 0 \quad (2)$$

where \bar{q} is the fluid mass flux over domain boundary Γ . Finite element discretization allows solving these nonlinear field equations for prescribed boundary conditions in an iterative way, for which the method is implemented in the finite element code Lagamine (Université de Liège). The local second gradient paradigm provides the assumption of decoupling between the classical part of the model and the second gradient part, which is of vital importance to the coupling with the framework of computational homogenization; the first and second gradient part of the model can therefore be formulated independently. A general formulation of the constitutive relations can therefore be formulated as

$$\begin{bmatrix} C_{ijkl} & A_{ijl} & B_{ij} \\ D_{ikl} & E_{il} & G_i \\ H_{kl} & K_l & L \end{bmatrix} \begin{bmatrix} \frac{\partial \delta u_k}{\partial x_l} \\ \frac{\partial \delta p}{\partial x_l} \\ \delta p \end{bmatrix} = \begin{bmatrix} \delta \sigma_{ij} \\ \delta m_i \\ \delta \dot{M} \end{bmatrix} \quad (3)$$

and

$$D_{ijklmn}^{SG} \frac{\partial \delta v_{lm}}{\partial x_n} = \delta \Sigma_{ijk} \quad (4)$$

The latter is formulated as a phenomenological relation (Collin et al. 2006), the former is the general expression of the classical part of the model, which is coupled to the micromechanical part in the framework of computational homogenization. The lefthand matrix of (3) is derived from the microscale modelling of the material response to a variation of the kinematics increments.

3. The framework of computational homogenization for HM coupling

The classical part of the macroscale constitutive relation in (3) is to be derived from the response to kinematical loading of the material at the microscale. For coupling the micro and macroscale, a representative elementary volume is used to model the material response to kinematical loading. The periodic boundary conditions of the boundary value problem on the REV are dictated by the local kinematics of the macroscale. The microscale fluid pressure p^m is decomposed in an average pressure \bar{p} and a fluctuation part \hat{p} ;

$$p^m = \bar{p} + \hat{p}(5)$$

with the variation of the pressure fluctuations of the microscale fluid pressure within the REV is negligibly small with respect to the average pressure and only serves as to derive the fluid mass fluxes.

$$\delta u_i^+ = \delta u_i^- + \frac{\partial \delta u_i^M}{\partial x_j} (x_j^+ - x_j^-)(6)$$

$$\delta \hat{p}^+ = \delta \hat{p}^- + \frac{\partial \delta p^M}{\partial x_j} (x_j^+ - x_j^-)(7)$$

$$\delta \bar{p} = \delta p^M(8)$$

For a consistent application of periodic boundary conditions, the microstructure is enforced to honour the REV periodicity. With these boundary conditions, the BVP on the microstructural REV can be solved for an arbitrary micromechanical model using finite element discretization of the steadystate problem. The application of the internal equilibrium of the microscale problem, Gauss theorem of divergence and the periodic boundary conditions, the homogenised response of the REV can be derived according to the Hill-Mandel condition of macro homogeneity (van den Eijnden, 2015);

$$\sigma_{ij}^M = \frac{1}{V_{REV}} \int_{\Gamma^+} \bar{t}_i^m (x_j^+ - x_j^-) dS(9)$$

$$m_i^M = \frac{1}{V_{REV}} \int_{\Gamma^+} \bar{q}^m (x_j^+ - x_j^-) dS(10)$$

$$M^M = \frac{1}{V_{REV}} (\int_{\Omega^{grn}} n \rho^w dV + \int_{\Omega^{int}} \rho^w dV)(11)$$

These integrals are solved numerically by means of the finite element method, in which the boundary integrals are replaced by the sum of the reaction forces and fluxes at the boundary nodes. For deriving the consistent tangent stiffness matrix, the global finite element system of equations of the coupled micromechanical problem is used. This system of equations has the general form

$$\begin{bmatrix} K^{mm} & K^{mh} \\ K^{hm} & K^{hh} \end{bmatrix} \begin{Bmatrix} \delta u \\ \delta p \end{Bmatrix} = \begin{Bmatrix} \delta f \\ \delta q \end{Bmatrix}(12)$$

This system of equations is the linearization of the equilibrium of the microscale problem with respect to the current loading direction. Using boundary conditions (6)-(8) and global response definitions (9)-(11), this system of equations, can be extended to include the

variations of the macroscale kinematics and its dual responses, after which the system can be reduced to allow static condensation into a 7×7 system of equations forming the linearization of the REV response around the current configuration relative to the current loading rate of the macroscale kinematics:

$$\begin{bmatrix} C_{ijkl}^* & A_{ijl}^* & B_{ij}^* \\ D_{ikl}^* & E_{il}^* & G_i^* \\ H_{kl}^* & K_l^* & L^* \end{bmatrix} \begin{bmatrix} \frac{\partial \delta u_k}{\partial x_l} \\ \frac{\partial \delta p}{\partial x_l} \\ \delta p \end{bmatrix} = \begin{bmatrix} \delta \sigma_{ij} \\ \delta m_i \\ \delta M \end{bmatrix} \quad (13)$$

This expression is fully consistent with the definitions of the macroscale response in (9)-(11). A final transformation of this linearization is the transformation of the 7th equation to change δM into $\delta \dot{M}$ by a finite difference approximation over the macroscale timestep Δt . After correction for the storage term, (13) forms the consistent linearization that provides the consistent tangent matrices as defined in (3), required for solving the macroscale boundary value problem.

4. The microscale model

At the microscale, the material microstructure is modelled as a granular assembly of solid or porous units (grains), separated by cohesive interfaces, using a model based on Frey et al. (2012). These interfaces form a network of pore channels between the grains through which fluid can percolate (Figure 2).

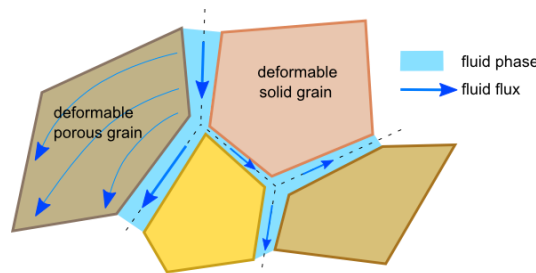


Figure 2. Concept of the micromechanical model. (van den Eijnden, 2015)

Solids are considered to be linear elastic; interface cohesive forces as a function of the relative openings of interfaces is modelled through damage laws for normal and tangential forces as a function of normal and tangential interface openings Δu_n and Δu_t respectively (Figure 3). Main part of the material deformation and degradation therefore takes place in the grain interfaces.

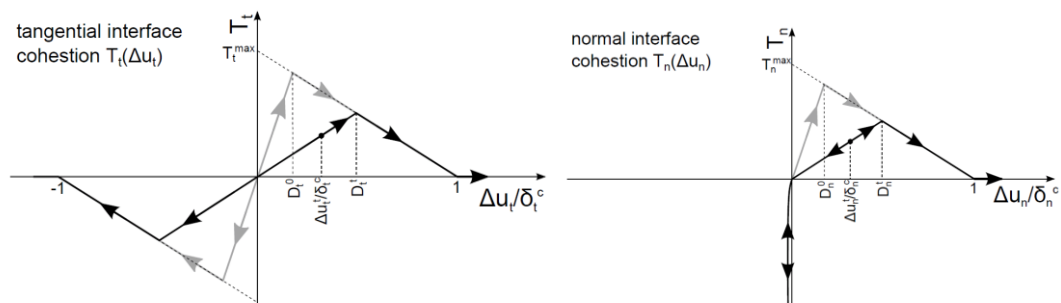


Figure 3. Damage model for normal and tangential cohesion $T_n(\Delta u_n)$ and $T_t(\Delta u_t)$ (van den Eijnden, 2015)

As a result of the separation of scales, the microscale problems can be solved in steady state conditions and fluid storage is only a macroscale phenomenon. Poiseuille flow between parallel plates, separated by the local interface opening Δu_n , is used to model fluid flow in the interface channels; Darcian flow is considered in the porous grains. The micromechanical solid-fluid interaction is through the mechanical opening of the interfaces and the hydrostatic fluid pressure at the solid grain boundaries. Separation of scales allows solving the (nonlinear) mechanical microscale problem independent from the fluid system, after which the hydraulic problem is solved in a direct way.

5. Application to biaxial compression tests and gallery excavations

Two examples of the application of the model are shown here. A first one is the simulation of the biaxial compression test on a lab specimen under transient loading conditions. Drainage is applied at the top and the bottom; both sides are considered impervious. The specimen is loaded beyond the peak strength to study the post-peak mode of deformation of the macroscale domain (shear banding), microstructural deformation (interface softening and decohesion) and the hydraulic response (fluid mass flux and permeability evolution) as shown in Figure 4.

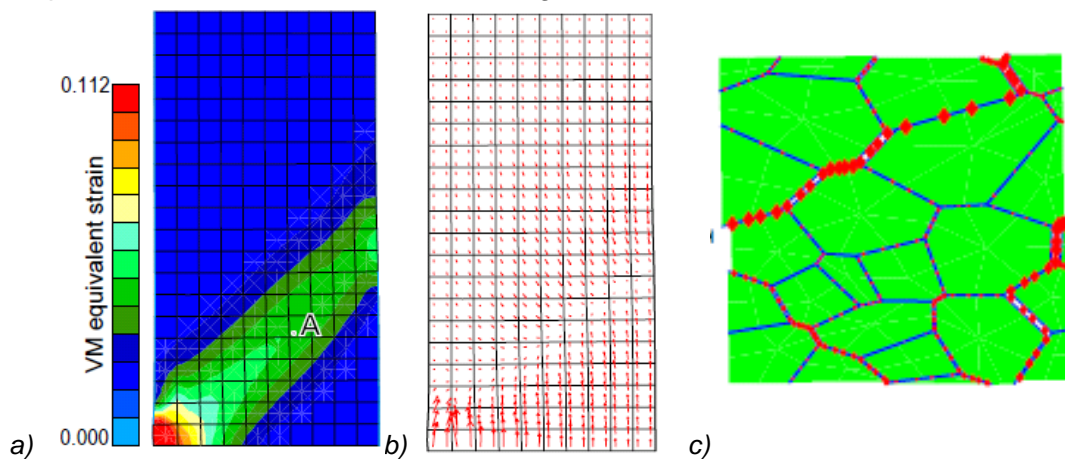


Figure 4. Macro and micro response to biaxial loading. a) Von Mises equivalent strain shows the shear band that developed in the sample. b) the fluid mass flux tends towards the active localized zone due to shear dilatancy. c) The microstructure inside the shear band (point A) shows continuous paths of interfaces under softening (in red).

A second example is the simulation of the excavation of a gallery by means of a quarter-gallery simulation under anisotropic stress state $\sigma_{xx}/\sigma_{yy} = 12.7 \text{ MPa} / 16.4 \text{ MPa}$ representative for in-situ conditions of deep geological repositories for nuclear waste disposal. Excavation is simulated by lowering the gallery support from initial conditions to free boundary. Figure 5 shows the shear bands forming around the gallery. The positioning and orientation of the shear bands are influenced by the in-situ stress state, the inherent material anisotropy and (in case of material softening) the periodic boundary conditions enforced on the REV.

6. Conclusions

A multiscale FE² approach to the modelling of hydromechanical behaviour of geomaterials is developed in the framework of computational homogenization. The presented modelling approach allows the definition of a macroscale constitutive relation for a poromechanical continuum to be derived from microscale modelling of the material microstructure and the interaction between solid skeleton and the pore fluid. A fully

consistent homogenization approach allows the derivation of the consistent tangent stiffness matrix without relying on numerical perturbations.

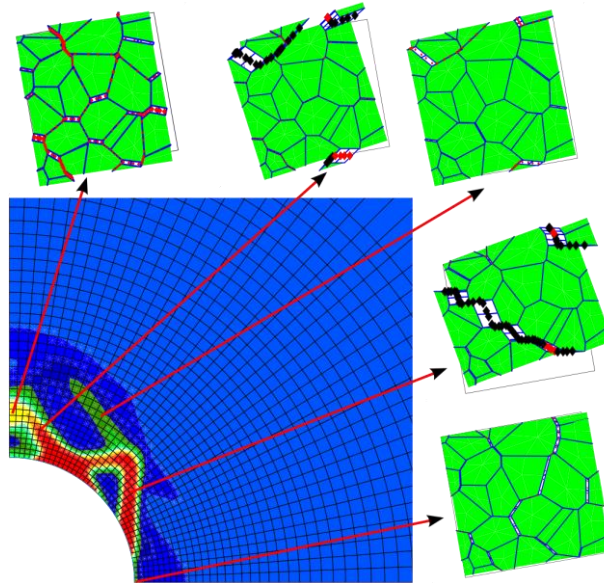


Figure 5. Localization around a quarter-gallery, visualized by VM equivalent strain, with deformed microstructures in the different shear band orientations with red for interface softening and black for full interface decohesion (van den Eijnden, 2015).

The implementation of the developed model in the finite element code Lagamine and the combination with a local second gradient model for hydromechanical coupling allows the application of the model to simulations of strain localization in both academic and engineering examples. The application to the simulations of biaxial compression tests and strain localizations in the excavation damaged zone around galleries for deep geological disposal sites are demonstrated.

7. Acknowledgements

The authors like to thank the French national radioactive waste management agency (Andra) for supporting the first authors PhD thesis.

8. References

- Chambon, R., Caillerie, D., Matsushima, T. 2001. Plastic continuum with microstructure, local second gradient theories for geomaterials: localization studies, *International Journal of Solids Struct.* 38: (46-47), 8503–8527.
- Collin, F., Chambon, R., Charlier, R. 2006. A finite element method for poromechanical modelling of geotechnical problems using local second gradient models. *International Journal for Numerical Methods in Engineering* 65 (11), 1749–1772.
- van den Eijnden, B., 2015. Multiscale modelling of the hydromechanical behaviour of argillaceous rocks. *PhD. thesis*, Université de Grenoble.
- Frey, J., Dascalu, C., Chambon, R., 2012. A two-scale poromechanical model for cohesive rocks. *Acta Geotechnica* 7, 1–18.
- Geers, M., Kouznetsova, V., Brekelmans, W., 2010. Multi-scale computational homogenization: Trends and challenges. *Journal of Computational and Applied Mathematics* 234 (7), 2175–2182.
- Kouznetsova, V., Brekelmans, W., Baaijens, F., 2001. An approach to micro-macro modeling of heterogeneous materials. *Computational Mechanics* 27 (1), 37–48.

MULTISCALE MODELLING OF THE THERMO-VISCOELASTIC PROPERTIES OF CEMENT-BASED MATERIALS AND STRUCTURES AT EARLY-AGE

Tulio Honorio (tulio.honorio-de-faria@enpc.fr)

CEA, DEN, DPC, SECR, Laboratoire d'Etude du Comportement des Bétons et des Argiles, F-91191 Gif-sur-Yvette, France

LMT (ENS Cachan, CNRS, Université Paris Saclay) 94235 Cachan, France

Benoit Bary

CEA, DEN, DPC, SECR, Laboratoire d'Etude du Comportement des Bétons et des Argiles, F-91191 Gif-sur-Yvette, France

Farid Benboudjema

LMT (ENS Cachan, CNRS, Université Paris Saclay) 94235 Cachan, France

ABSTRACT. The prediction of the thermo-mechanical response of concrete structures depends on the adequate determination of the thermal and mechanical properties of the material. These properties, especially at early-age, depend on the evolution of the microstructure and multiscale characteristics of cement-based materials. Based on upscaling techniques, we propose a strategy to estimate the viscoelastic and thermal properties of cement-based materials. Then, in a sequenced approach, a phenomenological analysis is performed at the structure level in order to derive practical information regarding the construction of a massive concrete structure for nuclear waste disposal on surface. This sequenced approach constitutes a holistic way of predicting the behaviour of concrete structures from the composition of the material as well as other initial and boundary conditions.

1. Introduction

The prediction of the thermo-mechanical response of concrete structures depends on the adequate determination of the thermal and mechanical properties of the material. Phenomena of different physical origins influence the overall behaviour of cement-based materials. More particularly at early-age, hydration processes, which are exothermic and lead to capital changes in the microstructure of the material, affect the evolution of key mechanical and thermal properties. Moreover, a relevant description of the behaviour of cement-based materials needs to account for the multiscale character of the material since, in general, the mechanisms modifying the properties of interest cannot be completely understood at that macroscopic scale (scale of the industrial applications).

In this context, we propose (1) to develop and apply upscaling tools to estimate rigorously the key properties of concrete needed in an early-age analysis from the composition of the material, and (2) to perform numerical simulations in order to describe and predict the thermo-chemo-mechanical behaviour at early-age of a massive concrete structure devoted to nuclear waste disposal on surface. Firstly, by means of a simplified model of cement hydration kinetics, the evolution of the different phases at the cement paste level can be estimated. Then, analytical and numerical tools to upscale the ageing properties are applied to estimate the mechanical and thermal properties of cement-based materials. Secondly, a thermo-chemo-mechanical analysis aims at determining the influence of boundary conditions on the thermo-mechanical response of the massive concrete structure. Practical recommendations regarding the construction of this structure are provided in order to limit the maximum temperature and the crack opening reached within the structure. This sequenced approach constitutes a holistic way of predicting the behaviour of concrete structures from the composition of the material as well as other initial and boundary conditions.

2. Multiscale representation of cement-based materials

We combine analytical and numerical tools to upscale cement-based materials properties. Analytical homogenization is used to estimate the properties at the cement paste up to mortar scale. We employ inclusions-matrix morphologies (Fig. 1) to represent the material from hydration products up to concrete scale, as similarly proposed by e.g. (Bary and Béjaoui, 2006). Mori-Tanaka (MT) and Generalized Self-Consistent (GSC) estimations are employed. At cement paste scale, the hydrating clinker particle is embedded in a high density (HD) products layer, which is, in turn, embedded in a low density (LD) products layer. At mortar scale, sand particle is embedded in an ITZ layer, which is embedded in a cement paste layer. The formulations of the schemes in ageing linear viscoelasticity are presented in (Honorio, 2015; Sanahuja, 2013a). At concrete scale, the coarse aggregates are embedded in a mortar matrix and no ITZ is considered. Analytical homogenization is used to estimate thermal properties and numerical homogenization is used to estimate linear viscoelastic properties. The evolution of the volume fractions at the hydration products scale is obtained by means of a simplified model of hydration kinetics (Honorio et al., submitted), as shown in Fig. 2. The values of elastic properties and thermal properties used in the estimations can be found in (Honorio, 2015). For air thermal conductivity, no convection and radiation effects are considered. Also, we assume that a percolated structure exists at the different levels.

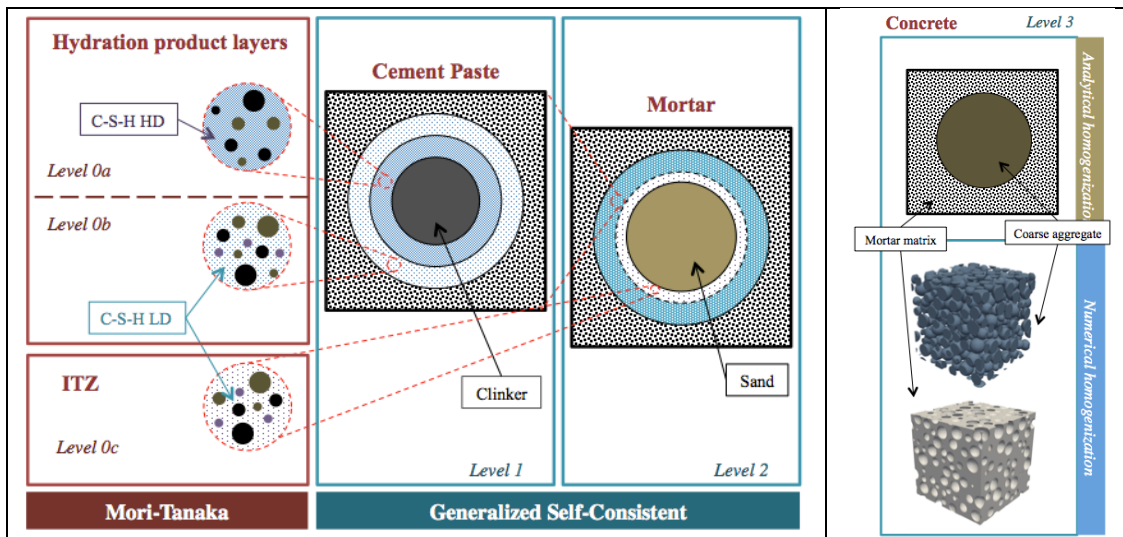


Figure 1. Representation of the materials from hydration products up to concrete

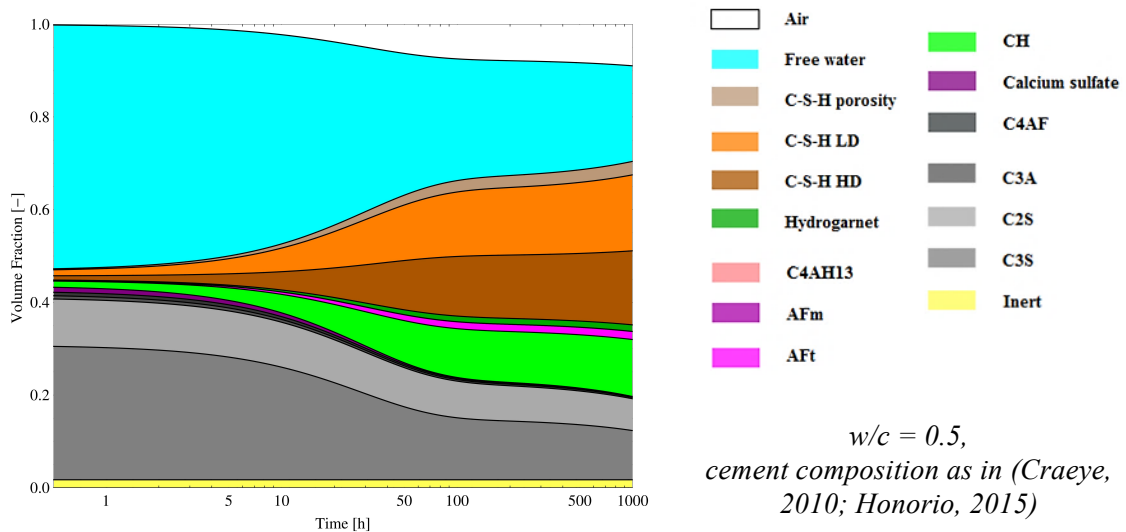


Figure 2. Evolution of volume fractions at cement paste scale.

Cement paste scale: solidification and space-filling

Bazant (1977) showed that an ageing effective behaviour can be observed in materials in which one of the constituents shows a change in its volume fraction in time, as occurs for example in a solidification process, even if the basic constituents are non-ageing. This so-called *solidification theory* can be extended to a general form in which dissolution and precipitation of multiphase systems occur in more complex geometries (other effects, which can also be the origin of the ageing aspect in cement-based materials, are not considered hereafter (Bazant et al., 1997)). Sanahuja (2013b) proposed a tensorial extension of this theory. An evolution function is attributed to each phase present in the paste according to the previously cited hydration kinetics model. The repartition of the products in High Density and Low Density layers is made proportionally to the volume of C-S-H in the layer. A part of the products is reserved to the ITZ. A viscoelastic behaviour is attributed to C-S-H phases following Vandamme and Ulm (2009) results. The other phases are assumed to behave elastically.

Mortar and concrete scales

ITZ is explicitly considered at the mortar scale. To compute the volume of the ITZ according to the PSD of sand, we adopt Garboczi and Bentz (1997) approach, so that the interpenetration of the ITZs is accounted for. At the concrete scale (Level 3), numerical homogenization is used to estimate the properties. Two phases are considered: the coarse aggregates with elastic behaviour and the mortar matrix with ageing viscoelastic behaviour obtained from the previous sections. Note that, since the specific surface of coarse aggregates is much smaller than that of the sand, the ITZ of the coarse aggregates are neglected (Bary et al., 2015).

Thermal properties

Similarly to what is done for the viscoelastic properties, we propose a multiscale estimation of the thermal conductivity, heat capacity and coefficient of thermal expansion (CTE) at early age based on homogenization theory, following (Honorio et al., 2015a) approach and hypotheses. Regarding the **thermal conductivity**, MT and GSC estimations for a n-phase composite with spherical inclusions, as given by (Benveniste, 1987, 1986), are used. Regarding the **heat capacity**, for small changes in strain and temperature in a thermoelastic n-phase isotropic composite, it can be shown that the effective heat capacities at constant stress $\overline{C_p}$ and strain $\overline{C_v}$, for cement-based materials, are almost equivalent so $\overline{C_p} \approx \langle C_v \rangle \approx \overline{C_v}$ (Honorio et al., 2015a). Finally, regarding the **CTE**, assuming perfect bonded phases, Levin (1967) equation can be applied for both Mori-Tanaka and self-consistent schemes by adopting the corresponding localization tensor. This formulation can be derived for a solidifying solid in ageing linear viscoelasticity, assuming no thermo-activation on the viscous effects (Honorio et al., 2015a).

3. Structure scale and environment

At the structure scale, the environmental conditions affect directly the thermo-mechanical response. Conduction, convection and radiation (solar and reradiation emitted by the structure) phenomena impact the thermal response. Internal and external mechanical restraints also play a major role on the overall response. A systematic study of these aspects does not necessarily need to take into account the multiscale character of the material once the key properties have been estimated. Therefore, by means of a phenomenological approach the main estimated properties can be used.

A chemo-thermal study developed in Honorio et al. (2014), is proposed in order to obtain the thermal response of a concrete massive structure. Then, by means of a

mechanical analysis based on an ageing visco-damage behaviour of concrete (Honorio et al., 2015), the risk of damage is assessed and the crack openings evaluated (following (Matallah et al., 2010) method). The estimations of concrete properties obtained by homogenization are used to feed the phenomenological analysis. Only the asymptotic values of thermal properties are used in the simulations. The studied structure of reinforced concrete, devoted to surface nuclear waste disposal, is to be built in Dessel, Belgium (the data concerning the weather of this region is considered). Other details about the simulation can be found in (Honorio et al., 2014; Honorio et al., 2015, p. 201).

4. Results

Ageing viscoelastic and thermal properties

The estimated creep response of the studied concrete and the comparison with experimental data are shown in Fig. 3. Numerical samples with spherical and Voronoi inclusions are studied (see Honorio et al. (2015), for details). A reasonable agreement between the experimental results and the estimation are obtained.

Figure 4 shows the estimations of the heat capacity (left) and thermal conductivity (right). Similar CTE estimation can be obtained as presented in (Honorio et al., 2015). A concordance between the asymptotic values obtained by (Cræye, 2010) is observed.

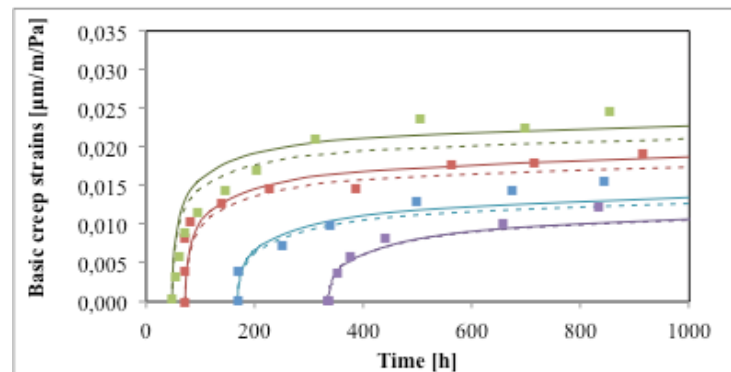


Figure 3. Basic creep of concrete obtained experimentally (symbols, (Cræye et al., 2009)) and by modelling: comparison between the mesostructures with spherical (full lines) and Voronoi (dashed lines) inclusions for scenarios with space-filling

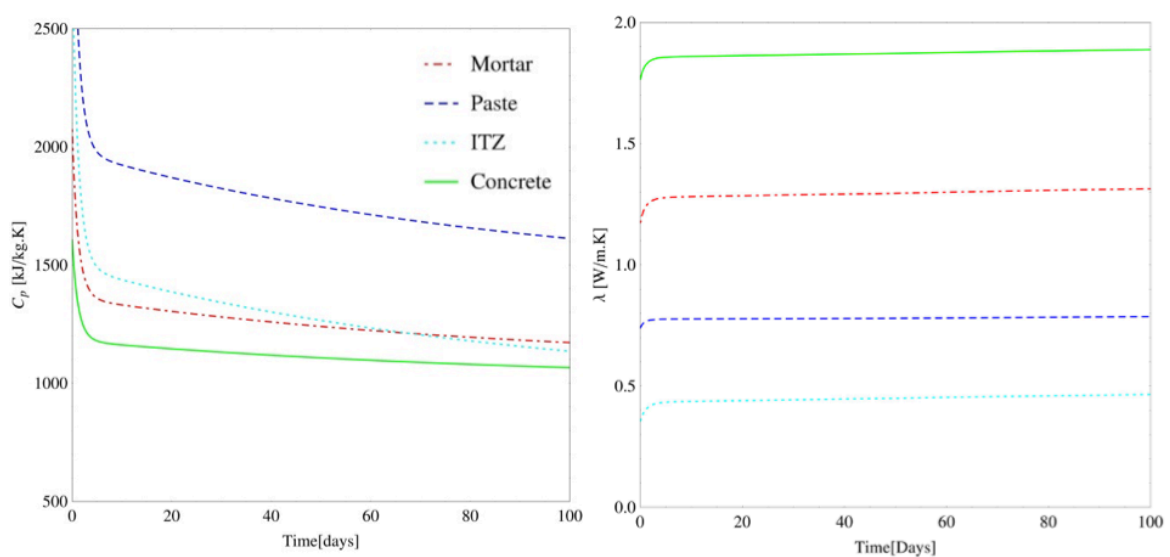


Figure 4. Heat capacity (left) and thermal conductivity (right) of cement paste, mortar, ITZ and concrete as estimated in an ageing multiscale framework.

Thermo-chemo-mechanical response at the structure scale

Figure 5 shows the comparison of the estimated evolution of temperature in different points of the studied structure and the in-situ measured temperatures. Again, an agreement between estimations and experimental measurements is observed. With this validation of the chemo-thermal analysis, new scenarios of interest were tested for the temperature of a cold reference month (November) and a hot reference month (August). The damage patterns and resulting crack openings are shown in Figure 6 for August. A parameter β (Mazzotti and Savoia, 2003) accounting for the coupling between creep and damage is considered in the simulations. In all scenarios the crack opening is below the preconized maximum opening of 300 μm .

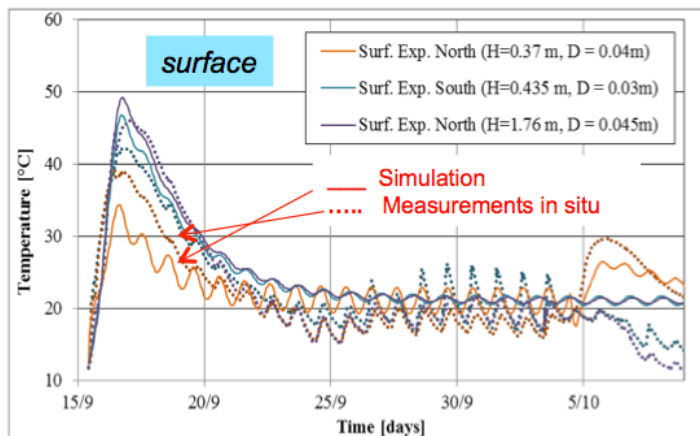


Figure 5. Evolution of the temperature in different points of a massive structure: modelling results compared to in-situ measurements

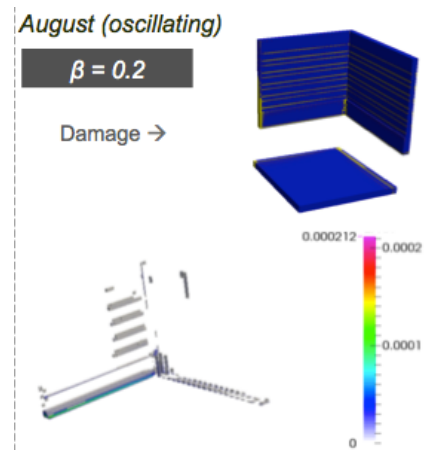


Figure 6. Damage pattern and crack opening ($>1 \mu\text{m}$) for August temperatures.

5. Conclusions and perspectives

We proposed a holistic approach to analyse massive concrete structures from the composition of the material and the main initial and boundary conditions. Thermal and viscoelastic properties are estimated by means of upscaling techniques developed in an ageing framework and provide the input data to a phenomenological analysis performed at the level of the structure. At this level the influence of the thermal and mechanical boundary conditions is evaluated in order to define scenarios in which the risk of thermal cracking is limited. Such kind of analysis provides a good practical response to the construction of massive concrete structures. Also, by means of the homogenization approach developed, a contribution towards the understanding of the phenomena affecting the evolution of properties at early age is presented. The homogenization-based approach also allows increasing the confidence of the phenomenological analysis reducing its empirism and enlarging its scope of application.

The confrontation of the modelling approach with a more exhaustive experimental campaign may validate in a more comprehensive way the strategy developed here. The non-consideration of a mechanical percolation threshold limits the range of applicability of the estimations. Further researches in this direction could be interesting. An approach accounting for the dependency of the temperature on the mechanical (including viscous) and thermal properties in a multiscale framework is to be developed.

Acknowledgements

This present work has been performed as part of the project on disposal of LILW-SL that is carried out by ONDRAF/NIRAS, the Belgian Agency for Radioactive Waste and enriched Fissile Materials.

6. References

- Bary, B., Béjaoui, S., 2006. Assessment of diffusive and mechanical properties of hardened cement pastes using a multi-coated sphere assemblage model. *Cem. Concr. Res.* 36, 245–258. doi:10.1016/j.cemconres.2005.07.007
- Bary, B., Bourcier, C., Helfer, T., 2015. Numerical analysis of concrete creep on mesoscopic 3D specimens. Presented at the Mechanics and Physics of Shrinkage, Creep and Durability of concrete: CONCREEP 10, Wien.
- Bazant, Z.P., 1977. Viscoelasticity of Solidifying Porous Material°Concrete. *J. Eng. Mech. Div.* 103, 1049–1067.
- Bazant, Z.P., Hauggaard, A.B., Baweja, S., Ulm, F.-J., 1997. Microprestressing-solidification theory for concrete creep. I: Aging and drying effects. *J. Eng. Mech.* 123, 1188–1194.
- Benveniste, Y., 1987. Effective thermal conductivity of composites with a thermal contact resistance between the constituents: Nondilute case. *J. Appl. Phys.* 61, 2840–2843. doi:10.1063/1.337877
- Benveniste, Y., 1986. On the effective thermal conductivity of multiphase composites. *Z. Für Angew. Math. Phys.* ZAMP 37, 696–713. doi:10.1007/BF00947917
- Craeye, B., 2010. Early-age thermo-mechanical behavior of concrete supercontainers for radwaste disposal. Gent University.
- Craeye, B., De Schutter, G., Van Humbeeck, H., Van Cotthem, A., 2009. Early age behaviour of concrete supercontainers for radioactive waste disposal. *Nucl. Eng. Des.* 239, 23–35. doi:10.1016/j.nucengdes.2008.10.006
- Garboczi, E.J., Bentz, D.P., 1997. Analytical formulas for interfacial transition zone properties. *Adv. Cem. Based Mater.* 6, 99–108. doi:10.1016/S1065-7355(97)90016-X
- Honorio, T., 2015. Modelling concrete behaviour at early-age: multiscale analysis and simulation of a massive disposal structure (PhD Thesis). ENS Cachan (Université Paris-Saclay), France.
- Honorio, T., Bary, B., Benboudjema, F., 2015a. Multiscale estimation of the thermal properties of cement-based materials at early-age. Presented at the SCS 2015 Numerical Modeling - Strategies for Sustainable Concrete Structures.
- Honorio, T., Bary, B., Benboudjema, F., 2015b. Factors affecting the thermo-chemo-mechanical behaviour of massive concrete structures at early-age. *Mater. Struct.* 1–19. doi:10.1617/s11527-015-0704-5
- Honorio, T., Bary, B., Benboudjema, F., 2014. Evaluation of the contribution of boundary and initial conditions in the chemo-thermal analysis of a massive concrete structure. *Eng. Struct.* 80, 173–188. doi:10.1016/j.engstruct.2014.08.050
- Honorio, T., Bary, B., Benboudjema, F., Poyet, S., submitted. Modelling hydration kinetics based on boundary nucleation and space-filling growth in a fixed confined zone.
- Levin, V.M., 1967. Thermal Expansion Coefficients of Heterogeneous Materials. *Lzu Akad Nauk SSSR Mekh Tuerd Tela Vol 2* 88–94.
- Matallah, M., La Borderie, C., Maurel, O., 2010. A practical method to estimate crack openings in concrete structures. *Int. J. Numer. Anal. Methods Geomech.* 34, 1615–1633. doi:10.1002/nag.876
- Mazzotti, C., Savoia, M., 2003. Nonlinear Creep Damage Model for Concrete under Uniaxial Compression. *J. Eng. Mech.* 129, 1065–1075. doi:10.1061/(ASCE)0733-9399(2003)129:9(1065)
- Sanahuja, J., 2013a. Effective behaviour of ageing linear viscoelastic composites: Homogenization approach. *Int. J. Solids Struct.* 50, 2846–2856. doi:10.1016/j.ijsolstr.2013.04.023
- Sanahuja, J., 2013b. Efficient Homogenization of Ageing Creep of Random Media: Application to Solidifying Cementitious Materials. *American Society of Civil Engineers*, pp. 201–210. doi:10.1061/9780784413111.023
- Vandamme, M., Ulm, F.-J., 2009. Nanogranular origin of concrete creep. *PNAS*.

METHODOLOGIES FOR AN EFFICIENT FORECAST OF THE DELAYED BEHAVIOUR OF PRESTRESSED CONCRETE BASED ON IMAGING AND NUMERICAL SIMULATIONS

Francis Lavergne (francis.lavergne@enpc.fr), Karam Sab, Michel Bornert
Université Paris-Est, Laboratoire Navier (ENPC, IFSTTAR, CNRS) 77455 Marne-la-Vallée Cedex, France

Julien Sanahuja, Charles Toulemonde
Département Mécanique des Matériaux et des Composants, EDF R&D, Site des Renardières, Avenue des Renardières, 77818 Moret-Sur-Loing Cedex, France

ABSTRACT. The time-dependent strains of concrete are investigated by describing concrete as a composite matrix-inclusion material, the cement paste being the sole responsible for the basic creep strains of the concrete. The hypothesis of a good binding between the aggregates and the cementitious matrix is backed by X-Ray tomography images and the influence of the morphology of aggregates is investigated by 3D numerical simulations. The sieve curve, the shape and the aspect ratio of aggregates are not expected to significantly affect the overall time-dependent strains. Though discrepancies of creep strains between similar concretes remain hard to explain, 3D numerical simulations can be applied to gain an insight on the local strains experienced in concrete subjected to loading conditions common in existing structures.

Introduction

Prestress losses due to the time-dependent strains of concrete is a matter of concern for the long-term operation of prestressed concrete structures, such as containment buildings and bridges. It has been observed that the time-dependent strains of concrete featuring similar formulations can be significantly different. Indeed, in the study of Granger [Granger1995], two concretes made of the same cement, using the same water to cement ratio, featured largely different basic creep strains [Lavergne2015a]. The only difference in their formulations was the use of crushed granite aggregates in one case and limestone and siliceous river aggregates in the other case. Various explanations have been proposed to explain such discrepancies : the difference might be attributed to the shape of the aggregates, to the adhesive properties between the aggregates and the cementitious matrix or more complex chemical phenomena might be occurring. To investigate these hypothesis, concrete is to be studied as a composite material featuring aggregates embedded in a cementitious matrix. First, it is shown that tomography can provide details on the microstructure of concretes supporting the hypothesis of a good binding between aggregates and the cementitious matrix. Then, 3D numerical simulations are performed to assess the effect of the shape of inclusions on the basic creep of viscoelastic composite materials. Lastly, the time-dependent strains of a sample of concrete material subjected to loading conditions similar to those experience in structures are estimated.

Observation of concrete by X-Ray tomography

Two different concretes have been observed using X-Ray tomography (fig. 1). These concretes differ in the nature of their aggregates. On the one hand, the first concrete, named B11 [Escoda2012], is made of crushed rough-shaped limestone aggregates and the imaged sample has experienced a drying creep test. On the other hand, the concrete of the VERCORS mock-up [Masson2015] is made of limestone and silicious aggregates which

where extracted near the Seine river. Consequently, these aggregates are rather oblate. The difference between these aggregates is easily spotted on the tomographic images. On the one hand, the difference of X-Ray absorption between the cement paste and the limestone aggregates is such that these aggregates can be distinguished from the cementitious matrix. On the other hand, at low energy, the absorption of silicious aggregates is similar to the one of the cementitious matrix. Consequently, the use of limestone aggregates is recommended if tomography of concretes with water to cement weight ratios around 0.5 is to be performed, to ease the segmentation of the aggregates.

Samples of different sizes have been scanned using X-Ray tomography. These images support the description of concrete as a multiscale matrix-inclusion composite material. Indeed, the sieve curve of concrete is such that it is not straightforward to guess the scale of an image. Moreover, the fact that no cracks have been spotted bolsters the hypothesis of a good binding between the aggregates and the cementitious matrix (fig. 2). The size of the voxels on the most resolved images is about $5\mu\text{m}$.

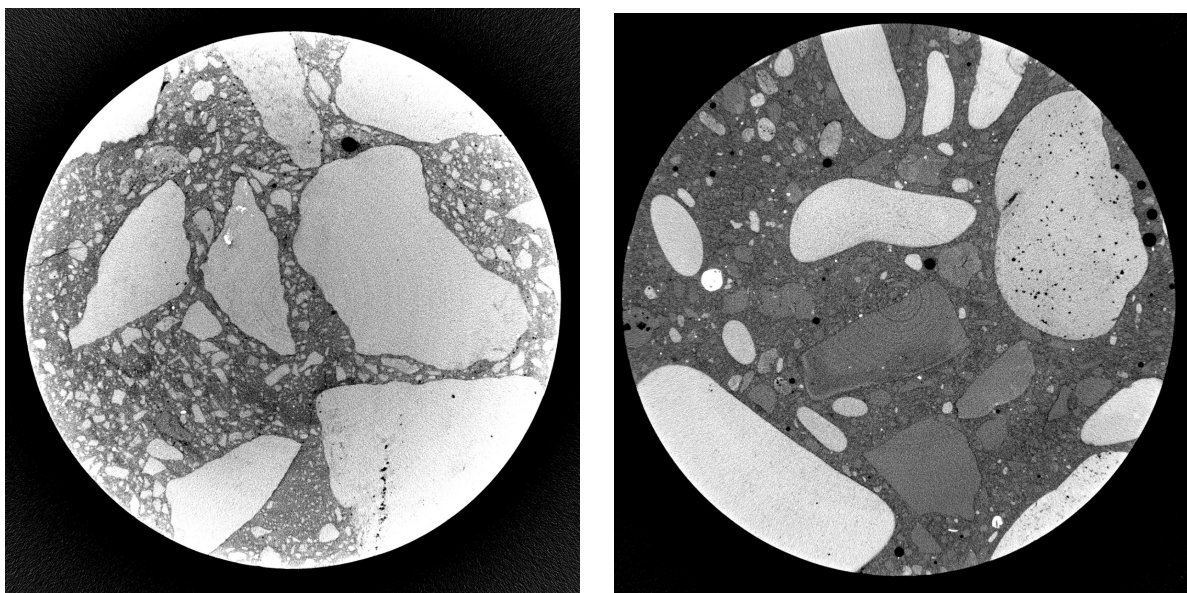


Figure 1. Excerpts of tomography images of 50mm cylinders of concretes. The voxel size is about $26\mu\text{m}$. Left: B11, The tension is $E=120\text{kV}$, the intensity is $I=200\mu\text{A}$. right: VERCORS. $E=150\text{kV}$ and $I=160\mu\text{A}$. The images are filtered to enhance the contrast.

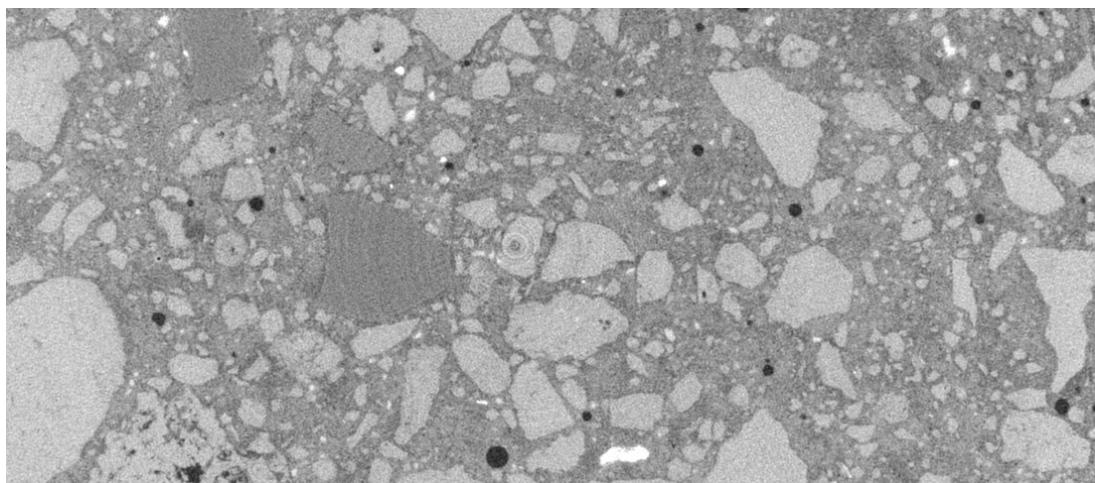


Figure 2. Excerpt of a tomography of the concrete B11. The size of the prismatic sample is $8\text{mm} \times 8\text{mm}$, $E=93\text{kV}$, $I=80\mu\text{A}$ and the size of the voxel is $6.3\mu\text{m}$. The size of the image above is $6.8\text{mm} \times 3\text{mm}$.

The influence of the morphology of aggregates on the overall basic creep strains of concrete

The influence of the size distribution, the shape and the aspect ratio of aggregates on the basic creep strain of concrete is estimated by performing 3D numerical simulations in the frame of periodic homogenization [Lavergne2015a]. First, an artificial unit cell of a periodic matrix-inclusion composite material is to be described. To this end, the Lubashevsky-Stillinger algorithm [Lubashevsky1990] and the Random Sequential Adsorption algorithm [Feder1980] have been adapted to model periodic microstructures featuring respectively spherical and convex polyhedral inclusions. In the second case, the overlapping between convex polyhedra is prevented by using the Gilbert–Johnson–Keerthi distance algorithm [Gilbert1987]. The periodicity of the inclusions is required so as to prevent boundary effects which would alter the estimate of the overall time-dependent strains. The unit cell is projected on a regular grid for mechanical computations. The aggregates are considered to be elastic, with a Young modulus of 60GPa and a Poisson's ratio of 0.2. The viscoelastic behavior of the cementitious matrix is similar to the series of Kelvin chains adjusted by Granger [Granger1995] on the experimental basic creep strain of the concrete of Penly. The compliance of the cementitious matrix $J(t,t')$ writes:

$$J(t-t') = C_0^{-1} + \sum_k C_k^{-1} (1 - e^{-\frac{t-t'}{\tau_k}})$$

where τ_k are the characteristic times of the Kelvin chains and the Young moduli of the stiffness C_k of the Kelvin chains are scaled so as to match an elastic Young modulus of 12GPa. All Poisson's ratio are set to 0.2. The 3D numerical simulations are performed as in [Smilauer2010]: the behavior is integrated on each time step according to the exponential algorithm and the FFT method of Moulinec and Suquet [Moulinec1998], accelerated by Eyre and Milton [Eyre1999] is applied to solve the elastic periodic homogenization problem on each time step. This numerical method is programmed so as to be run on clusters, using distributed memory. That way, using 12 nodes of the cluster enables to solve 180 elastic problems on a 384x384x384 grid in less than 4 hours. The major gain is that the inclusions can be accurately depicted while keeping a unit cell large enough to produce precise and representative estimates of the time-dependent strains.

The time-dependent strains corresponding to microstructures featuring unimodal spherical inclusions, bimodal spherical inclusions and polydisperse polyhedral inclusions (fig. 3) proved similar. Moreover, combining the correspondence principle and the mean-field scheme of Mori-Tanaka [Mori1973, Vandamme2013, Zhang2014] or the tri-sphere [LeRoy 1995, deLarrard1999] scheme provides comparable estimates of the time-dependent strains (fig. 4). Hence, neither the sieve curve of the aggregates nor their shape can explain discrepancies between measured time-dependent strains. An interfacial transition zone is then introduced at the mortar scale, following the model of Nadeau [Nadeau2003]: in the cementitious matrix, close to the aggregates, the stiffness decreases due to an increase of porosity and a change of the chemical constituents. As the width of the interfacial transition zone increases, both the estimated overall instantaneous strain and the estimated overall long-term strains are affected in comparable ways. For instance, a 50 μ m-thick ITZ induces a 20% increase of the instantaneous strains and a 26% increase of the strains 60 years after loading. Further investigations involving the use of mean-field schemes in the range of aging viscoelasticity have been conducted [Sanahuja2013, Lavergne2015b]. The behavior of cementitious matrix is set according to the aging compliance of the B3 model [Bažant1995] which satisfies the logarithmic long-term trend of creep strains of cementitious materials [Vandamme2013]. The aspect ratios of aggregates of reasonable flakiness ratios do not influence significantly the estimated effective time-dependent strains. Consequently, the morphology of the aggregates is not expected to affect the estimated overall compliance of

the concrete. Indeed, the experimental discrepancies between the measured basic creep strains of similar concrete is yet to be fully understood. The 3D numerical simulations also provide an insight on the local strains and the local stresses within the concrete, at the scale of the cement paste.

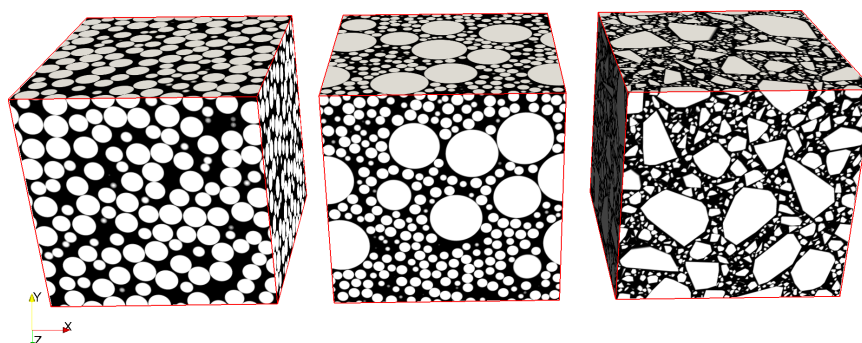


Figure 3 : Artificial unit cells of periodic matrix-inclusion microstructures are built to model concrete and discretized on $384 \times 384 \times 384$ regular grids. Unimodal spherical inclusions, bimodal spherical inclusions and polydisperse polyhedral inclusion are considered, the volume fraction of inclusions being 60%.

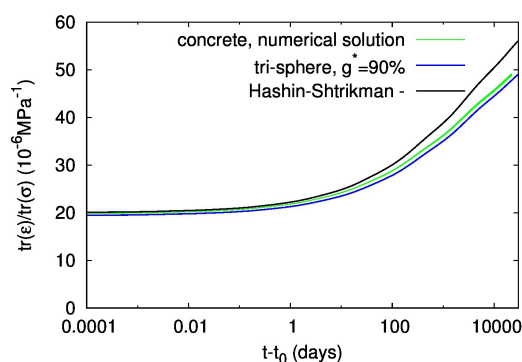


Figure 4 : The 3D numerical estimates of the time-dependent strains of a concrete made of 60% of polyhedral aggregates is similar to the estimates obtained by coupling the correspondance principle and mean-field schemes.

Numerical simulations of a concrete subjected to a biaxial loading

The 3D numerical simulations can also be applied to estimate the time-dependent strains of a sample of concrete experiencing a loading similar to the one existing in the cylindric section of a containment building. The loading, which occurs two years after casting the concrete, is biaxial : the vertical prestress is 12MPa while the circumferential prestress is 8.1MPa (fig 5). To account for the shrinkage of the cement paste, a time dependent eigenstrain is set in the cementitious matrix according to B3 model, the thickness of the cylinder being 1.2m. Moreover, the loading is actuated so as to account for the relaxation of prestressing tendons and the prestress losses induced by the time-dependent strains of concrete. Lastly, the effect of temperature is accounted for by introducing an activation energy of 4000K : keeping the equivalent time as a reference, the pressure tests performed every 10 years on real structures are modeled every 11 years in the simulation. The 3D numerical simulations produce estimates of the overall time-dependent strains which could be compared to the strains measured at structural scale and estimates of the prestress

losses (fig. 5). Moreover, the simulations can estimate local stresses within the microstructure, at the scale of the cement paste. For instance, the Rankine criterion can be positive in the cement paste despite the biaxial compressive load : there are positive principal stresses at the local scale. The Mazars criterion [Mazars1984] evolves significantly at loading time due to the Poisson's effect : the strain ϵ_{rr} in the radial direction is positive due to the compressive loading. This insight on the stress state at the local scale might prove valuable to investigate the evolution of the air tightness between pressure tests, but the orientations of the positive principal strains or stresses, related to the directions of potential opened microcracks, must be accounted for.

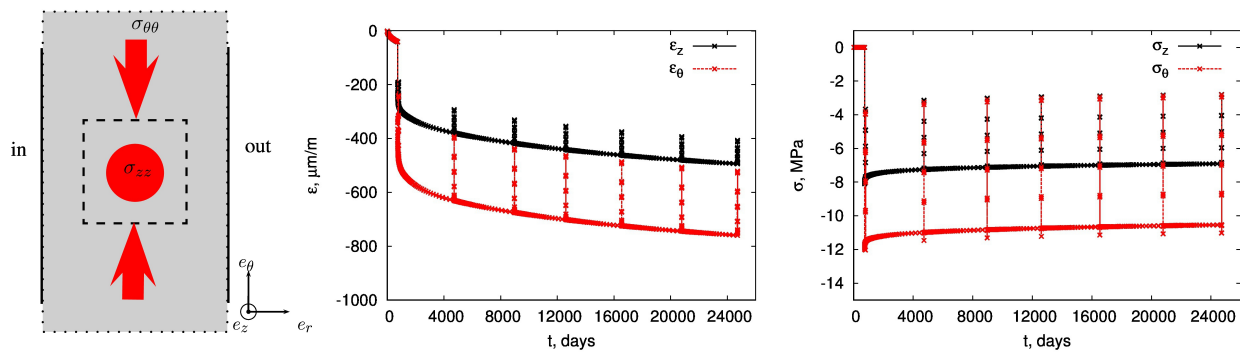


Figure 5 : Left : 3D numerical simulations are performed on a unit cell, the loading being similar to the one experienced in structures. Middle and right : estimates of the time-dependent strains and estimates of the prestress losses. The concrete remain compressed, even during the pressure tests.

Conclusions

The observations of concrete samples using X-Ray tomography have not shown any cracks that would entail the hypothesis of a perfect binding between the aggregates and the cementitious matrix. Hence, this hypothesis is considered as adequate as 3D numerical simulations are performed at concrete scale. By using such simulations on unit cells of artificial periodic matrix-inclusion microstructures, it is shown that the grain size distribution of the inclusions, their shape or their aspect ratio have no significant effect on the overall estimated time-dependent strains of the concrete. Hence, the use of a semi-analytical homogenization schemes such as the one of Mori-Tanaka should be considered as valid to study the viscoelastic behavior of concrete. Moreover, introducing an interfacial transition zone between the aggregates and the cementitious matrix in 3D numerical simulations has been performed at mortar scale: such an interfacial transition zone would affect both the instantaneous Young modulus and the time-dependent strains. Hence, understanding the discrepancies of the time-dependent strains between concretes featuring similar formulations and comparable Young modulus remains a challenge. Assumptions taken to describe the interfacial transition zone may be questioned or additional chemical effects could be considered. Finally, 3D numerical simulations allows for the study of the local strains and stresses within a artificial concrete microstructure while loading conditions similar to the ones experienced in structures are considered. In the future, such simulations might prove helpful in understanding the evolution of the air tightness of containment buildings, though more attention must be paid to the influence of the temperature and the relative humidity on the time-dependent strains of the cementitious matrix.

References

- Bažant, Z. P. and Baweja, S. (1995) Creep and shrinkage prediction model for analysis and design of concrete structures— model B3. *Materials and Structures*, 28(6) :357–365
- Escoda, J. (2012) Modélisation morphologique et micromécanique 3D de matériaux cimentaires. PhD thesis, Mines Paristech.
- Eyre, D. J. and Milton, G. W.(1999) A fast numerical scheme for computing the response of composites using grid refinement. *The European Physical Journal Applied Physics*, 6 :41–47, 4.
- Feder, J., Random sequential adsorption.(1980) *Journal of Theoretical Biology*, 87(2) :237 – 254
- Gilbert, E.G., Johnson, D. and Keerthi, S.S. (1987) A fast procedure for computing the distance between complex objects in three space. *In Robotics and Automation. Proceedings. IEEE International Conference on*, volume 4, pages 1883–1889
- Granger, L. (1995) Comportement différé du béton dans les enceintes de centrales nucléaires : analyse et modélisation. PhD thesis, Ecole Nationale des Ponts et Chaussées.
- de Larrard, F. (1999) Structures granulaires et formulation des bétons - Concrete Mixture - Proportionning - A scientific approach. Number 9. *Modern technology Series*, E & FN SPON, Londres.
- Lavergne, F., Sab, K., Sanahuja, J., Bornert, M. and Toulemonde, C.,(2015) Investigation of the effect of aggregates' morphology on concrete creep properties by numerical simulations. *Cement and Concrete Research*, 71(0) :14 – 28
- Lavergne, F., Sab, K., Sanahuja, J., Bornert, M. and Toulemonde, C.,(2015) Homogenization schemes for aging linear viscoelastic matrix-inclusion composite materials with elongated inclusions, *International Journal of Solids and Structures*, Available online 22 October 2015
- Le Roy, R. (1995) Déformations Instantanées et différées des bétons à hautes performances. PhD thesis, Ecole Nationale des Ponts et Chaussées.
- Lubachevsky, B. D. and Stillinger, F. H.,(1990) Geometric properties of random disk packings. *Journal of Statistical Physics*, 60 :561–583
- Masson, B., Galenne, E., Oukhemanou, E., Aubry, C., & Laou-Sio-Hoi, G. (2015). Vercors: a 1/3 scaled mockup and an ambitious research program to better understand the different mechanisms of leakage and aging. *Fontevraud 8: Conference on Contribution of Materials Investigations and Operating Experience to LWRs Safety, Performance and Reliability*, France
- Mori, T. and Tanaka, K. (1993) Average stress in matrix and average elastic energy of materials with misfitting inclusions. *Acta Metallurgica*, 21(5) :571 – 574.
- Moulinec, H., and Suquet, P. (1998) A numerical method for computing the overall response of nonlinear composites with complex microstructure. *Computer Methods in Applied Mechanics and Engineering*, 157(1–2) :69 – 94
- Mazars, J. (1984) Application de la mécanique de l'endommagement au comportement non linéaire et à la rupture du béton de structure, Université Pierre et Marie Curie, Laboratoire de mécanique et technologie.
- Nadeau, J.C. (2003) A multiscale model for effective moduli of concrete incorporating ITZ water–cement ratio gradients, aggregate size distributions, and entrapped voids. *Cement and Concrete Research*, 33(1) :103 – 113.
- Sanahuja, J. (2013) Effective behaviour of ageing linear viscoelastic composites : Homogenization approach. *International Journal of Solids and Structures*, 50 (19) :2846 – 2856.
- Smilauer, V. and Bažant, Z. P. (2010) Identification of viscoelastic C-S-H behavior in mature cement paste by fft-based homogenization method. *Cement and Concrete Research*, 40(2) :197 – 207.
- Vandamme, M. and Ulm, F.-J. . (2013) Nanoindentation investigation of creep properties of calcium silicate hydrates. *Cement and Concrete Research*, 52(0) :38 – 52.
- Zhang, Q., Le Roy, R., Vandamme, M., and Zuber, B.,(2014) Long-term creep properties of cementitious materials : Comparing microindentation testing with macroscopic uniaxial compressive testing. *Cement and Concrete Research*, 58(0) :89 – 98.

A MICRO-MECHANICAL STUDY OF CEMENTED GRANULAR MATERIALS

Alessandro Tengattini (alessandro.tengattini@sydney.edu.au), Itai Einav
School of Civil Engineering, The University of Sydney, Sydney, NSW 2006, Australia

Gioacchino Viggiani
Univ. Grenoble Alpes, 3SR, F-38000, Grenoble, France.

ABSTRACT. Cemented Granular Materials (CGMs) are ubiquitous in nature. Their behaviour is driven by phenomena occurring at the scale of individual grains and cement bonds. However, the effect of this scale on the engineering response has lacked a systematic description and is rarely acknowledged in the models portraying their behaviour. This work contributes to the development of a methodological framework for CGMs, relating the behaviour of individual grains to their collective response at the macroscopic scale, through a combination of analytical, experimental and numerical approaches. In this contribution, crucial features and main conclusions of the former two are overviewed.

Analytically, a novel constitutive model for CGMs is developed which adopts measurable internal variables describing the evolution of key grain-scale processes. This model can successfully predict stress-strain responses as well as the onset and development of localisation patterns for a wide range of pressure regimes. Its constitutive parameters have a precise physical meaning and are directly quantifiable.

Experimentally, specimens of CGMs are tested while acquiring x-ray images at a resolution sufficient to discern individual grains and cement bonds. A toolset is developed to characterise, for the first time, each grain and cement bridge in the specimen, their evolution, and to extract statistically representative measures of the grain-scale processes. This allows for a realistic validation of the constitutive models not only at the scale of the specimen response and its localisation features but also at the scale of individual grains, pivotal in several open engineering problems controlled by the localised evolution of the micro-structure.

1. Introduction

Cemented Granular Materials (CGMs) are a broad class of geomaterials in which densely packed particles are bridged by cement, which partially or completely fills the interstitial space, including sandstones, bio-cemented sands and even concrete. The shared micro structure of this materials causes analogous micro-mechanisms to lead the macroscopic response: grain crushing, cement damage and fragment reorganisation [1, 2]. Despite the coherent picture drawn by the experimental literature, most existing models for CGMs are phenomenological adaptations of classic elastoplasticity which neglect the grain-scale origin of the observed behaviour. These models have demonstrated their capability to fit the experimentally observed macroscopic behaviour, although the absence of direct links with the micro-scale processes often causes a high number of parameters and of the lack of physical interpretation for some of them.

Beside the ever-improving access to grain-scale phenomena given by recent technological advancements in microscopic imaging, also the advancements in computational power and numerical modelling (e.g. DEM) are allowing to get further understanding of such processes. This unprecedented insight on the physics involved at different scales urges the development of new theories, capable of extracting and describing the crucial phenomena. This allows both practical advancements in the prediction of the material behaviour and give direction to further pertinent studies.

The micro-mechanical bases of the proposed constitutive model its macroscopic performance are reviewed in §2 (a more comprehensive description can be found in [3,

4)]. The feasibility of the direct measurement of the proposed internal variables in 3D, in-situ, x-ray images is assessed in §3.

2. A constitutive model for cemented granular materials with micro-mechanics based internal variables

In the development of micro-mechanics based models a crucial step is the choice of the internal variables, which should ideally be identifiable, measurable and related to the dominant modes of irreversible rearrangements of the material microstructure. As highlighted in [6], in fact "internal variables inferred from phenomenological evidence and selected to fit a particular stress strain-curve may provide a result that pleases the eye but seldom contributes to the understanding of the processes represented by the fitted curve".

In CGMs, three main inelastic micro-scale processes drive the macroscopic behaviour: grain crushing, cement damage and fragment reorganization [1, 2]. The description of grain crushing has previously been tackled in [7, 8], by measuring the evolution of the grain size distribution. The scalar variable *Breakage* B , described in Fig 1a has therein been proposed and has been shown to successfully correlate the evolving micro-structure to the macroscopic behaviour.

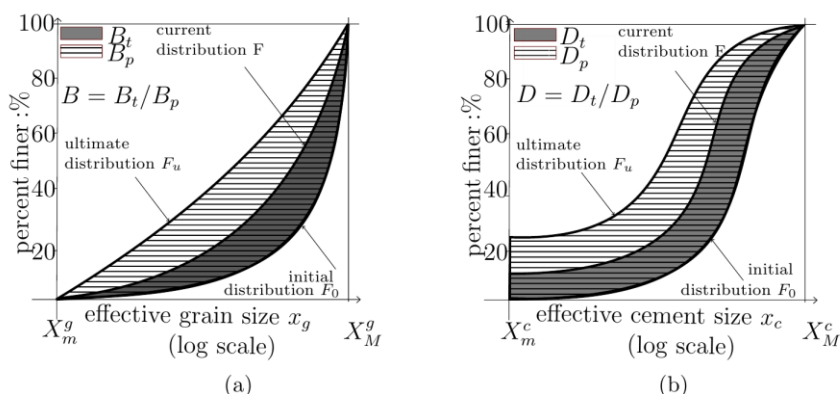


Figure 1. Scalar internal variables: a) Breakage (B), [7], b) Damage (D) [3].

The cement phase has an inherently different behaviour: it endows the system with tensile resistance, distributes the forces at the grain contacts, and enhances shear strength of the granular phase. When damage occurs in the cement, its role in the system is strongly re-dimensioned (e.g. see [9, 10]) and the mechanical contribution of its fragments to the force network is negligible to a first approximation. The proposed approach is therefore to describe damage through the evolution of the effectively working cement: when a cement bridge is partially cracked, we can in principle substitute it with another, with a smaller sectional area, but made of undamaged material with the same contribution to the system. It is then possible to define an effective cement size distribution and, analogously to the breakage variable B , define damage as the area ratio in Fig.1b. The possibility to experimentally assess this variable directly is discussed in §3.

The last inelastic microscopic process occurring, fragment reorganisation, can be effectively characterised by the plastic strain, which, describing the unrecoverable macroscopic strain, lends itself as an natural measure for this phenomenon.

The model at a glance

Beyond the possibility of having observable (at least in principle) descriptors of the micro-scale texture, the use of physically meaningful internal variables allows a rational connection between them, the evolution of the elastically stored energy and the energy dissipation. As shown in [7], in fact, it is possible to describe, through statistical

homogenization over a Representative Elementary Volume (REV), the elastically stored energy in a granular material describing how the Helmholtz free energy is distributed according to the grain size. It is then possible to deduce the evolution of the elastically stored energy as grain crushing proceeds and to connect its loss to the increment of dissipation. Imposing the first two laws of thermodynamics, it is eventually possible to deduce the full constitutive model, as detailed in [3, 4].

Macroscopic and structural validation of the model.

The proposed model requires only 8 parameters and 3 geometrical indexes, each having a precise physical interpretation, to be compared with the 13 or more parameters of well-established models (e.g. [5]). An example of the capabilities of the model to reproduce the experimentally observed macroscopic response for Bentheim sandstone is reported in Fig. 2.

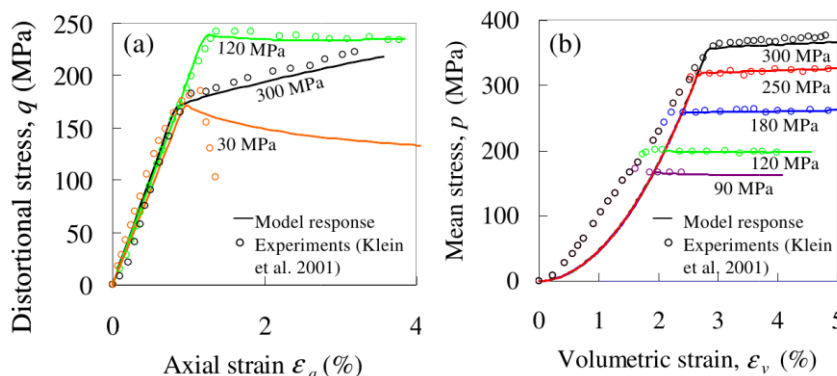


Figure 2. Drained triaxial tests on Bentheim sandstone (Klein et al., 2001); experimental observation and model predictions.

Implementing then the constitutive model within a finite element model with the very same set of mechanical parameters it is also possible to reproduce the typical localization patterns experimentally observed in samples undergoing drained triaxial compression, as shown in Fig. 3. An exhaustive description of the calibration process for the model parameters as well as the details of the finite element implementation and the localization analyses are reported in [4], but the aim of this contribution is to explore the possibility to also verify the model predictions regarding the evolution of the micro-structure.

3. Experimental measures of the evolving grain-scale structure

The grain-scale investigations of the behaviour of CGMs available in the literature,, upon which the above model is based, are largely qualitative in nature. While these observations do provide a valuable insight into the micro-mechanics, sufficient to build the model, quantitative measures are necessary to verify them and identify patterns hidden to the human eye. In the case of models with internal variables connected to the evolving microstructure, quantitative measures also open the possibility of a double-scale validation of the model prediction.

An ideal investigation tool for this purpose should have a resolution sufficient to discern the individual grains and cement bridges for an entire sample. The observations should ideally be in 3D and should allow multiple realisations of the observations at different stages of the tests without affecting the material behaviour. X-ray tomography is one of such tools and three key phenomena occurring in CGM, grain crushing, cement damage and fragment rearrangement can easily be imaged with this technique.

In [11] and subsequent works a technique to follow the individual grains throughout a test have been proposed for uncemented granular materials, allowing an immediate

measure of fragment rearrangement. Preliminary works exploring the in-situ 3D measure of the crushing-induced evolution of grain size distribution in granular materials have been proposed in [12, 13]. In this contribution we explore the possibility to also measure the last of the grain-scale phenomena: cement damage.

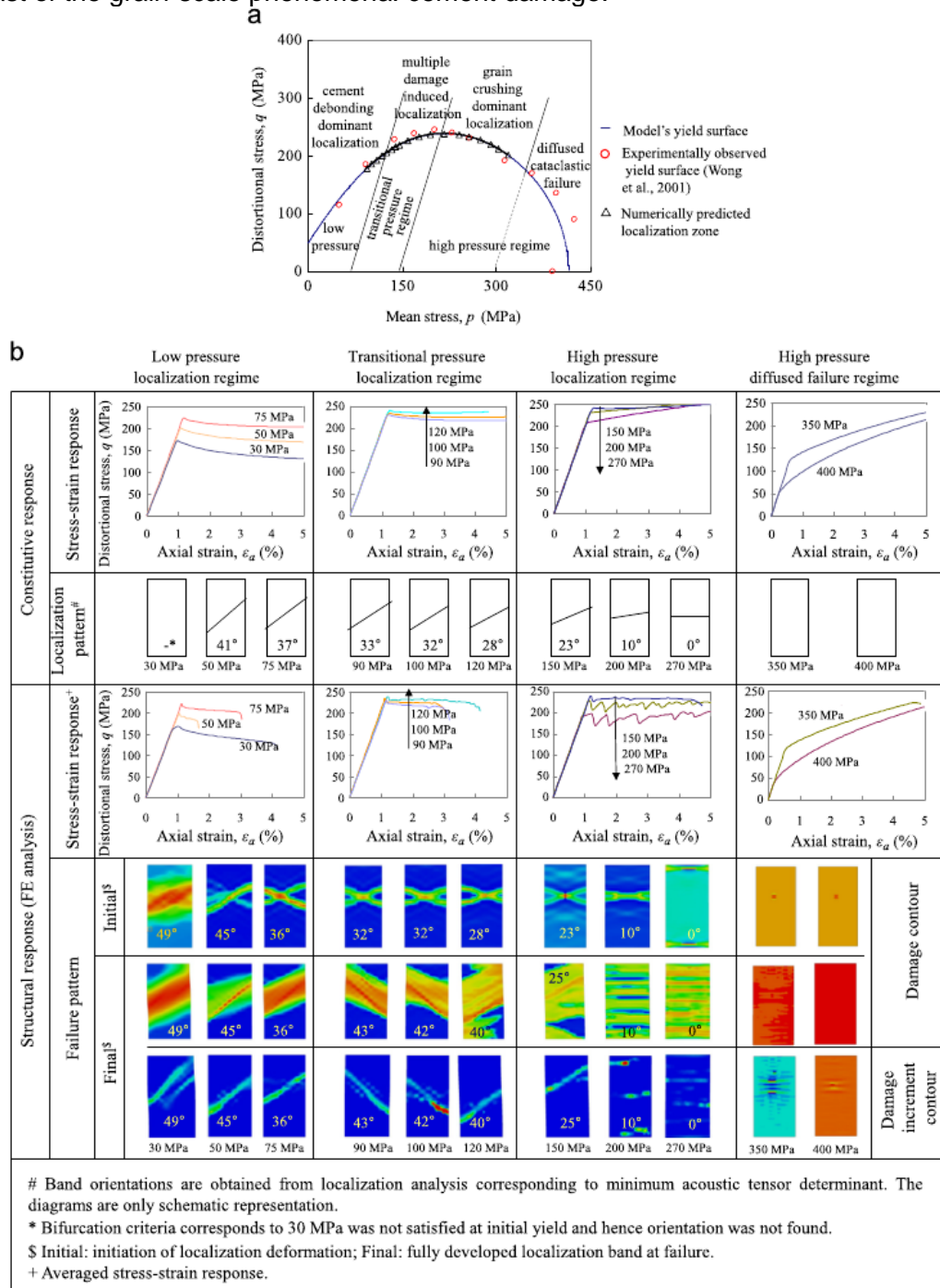


Figure 3. Failure modes of Bentheim sandstone: (a) yield envelope (the lines dividing zones are indicative only) (b) model responses under drained triaxial condition at different stress regimes.

With the aim of isolating cement fragmentation, a model material has been designed to prevent other inelastic phenomena such as grain crushing. Also, since a simple geometry of the granular phase allows to take advantage of the grain topology for image post-processing, spheres have been selected. The material proposed is calcite-cemented glass ballottini, with a D50 of about 300 μ m. Two different phases of image processing aimed to measuring damage can broadly be identified: cement identification and damage measure.

Phase identification

This crucial phase of image processing is traditionally named segmentation and, despite the large number of existing approaches, none of the methods proposed in literature has so far provided accurate, user-independent results for the images at hand. For this reason a new tool, named '*Kalisphera*', which takes advantage of the spherical shape of the granular part has been proposed as part of this doctoral work [14]. The idea of this method is to identify, through a template matching procedure, spheres in 3D images, as sketched in Fig. 4. It is at that point straightforward to remove the granular component from the images, obtaining an image containing only cement and voids. These remaining phases can be easily classified adopting any of the existing segmentation methods, which are straightforward and reliable for two-phase materials.

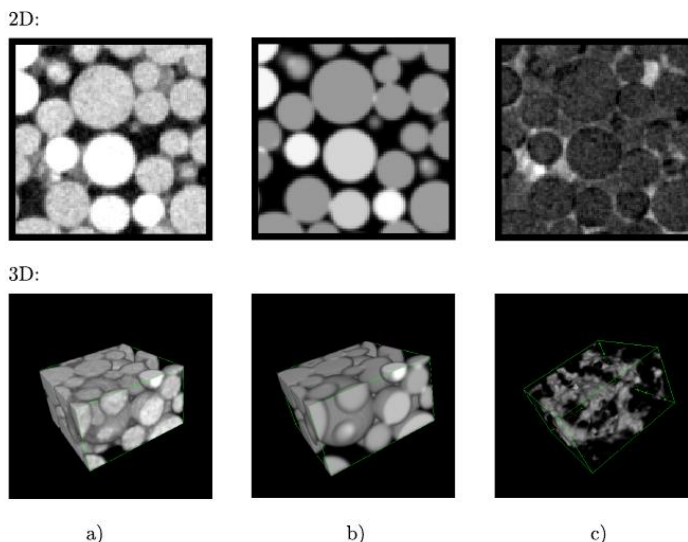


Figure 4. Example of the application of the proposed segmentation in 2D (top row) and 3D (bottom row): a) original image b) spheres obtained using the *Kalisphera* [14] method c) subtraction of the spheres from the original image, leaving behind only air and cement.

Measuring cement damage

Once discerned the existing phases it is possible to identify the individual inter-granular cement bridges, *i.e.* the cement contained in between any sufficiently close grain pair, as in Fig 5a. Combining this knowledge with that of the position of the individual grains throughout the test as in [11], it is possible to follow the position of each cement bridge in the test as well as their progressive fragmentation. Measuring then the reduction of intact cement, as proposed in the model in §2, it is possible to deduce the damage of each cement bridge. Averaging then this measure over multiple REV's, as in Fig 5b, it is possible to deduce statistically relevant measures of cement damage. This allows the study of the evolution of damage and its correlation with all the measured fields (e.g. strain, porosity), as in Fig. 5c, which highlights how damage concentrates within the shear band (measured using Digital Image Correlation). The direct measure of damage also allows the validation of the model's prediction of the evolution of the grain-scale texture, not included in this contribution for sake of brevity.

A video summarising some key steps of the image processing, prepared with the aid of computer graphics, can be found at <http://youtu.be/jilfKn1wqyU>.

4. Conclusions

In the present paper the fundamental hypotheses of a novel micro-mechanics based constitutive model for Cemented Granular Materials are discussed and its micro-

mechanics based internal variables described. Its capability to reproduce both the macroscopically observed mechanical response and the structural (specimen-scale) localization patterns is highlighted. The micro-mechanics based nature of the model calls though for a further level of validation, to assess its capability to predict the evolution of the grain-scale inelastic processes. To do so it has been necessary to develop *ad-hoc* image processing tools to extract quantitative, statistically representative measures of the evolving processes (grain crushing, cement damage and fragment rearrangements). This contribution focuses on the experiments and post-processing tools required to measure the evolution of each cement bridge of a mechanically representative sample of calcite cemented glass ballottini. The possibility of measuring *in-situ* cement damage goes well beyond the model validation itself and opens unprecedented possibilities in the understanding of the inter-relations of the micro-scale inelastic phenomena occurring in cemented granular materials.

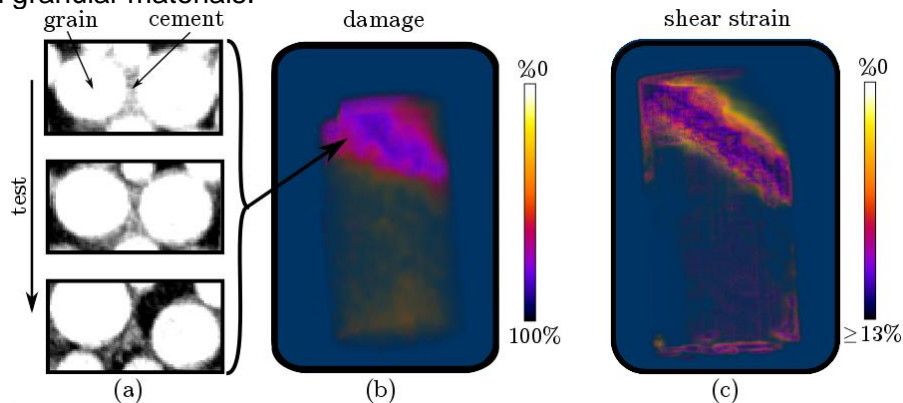


Figure 5. Experimental measure of damage: (a) typical fragmentation of inter-granular cement. It is possible to measure this damage and study its distribution as in the 3D rendering in (b). Damage is found to concentrate where also the shear strain focuses (c).

5. References

- [1] Menendez, B., Zhu, W., and Wong, T. Micromechanics of brittle faulting and cataclastic flow in Berea sandstone. *Journal of Structural Geology*, (1996) 18: 1-16.
- [2] Wong, T., and Baud, P. The brittle-ductile transition in porous rock: A review. *Journal of Structural Geology*. (2012) 44: 2-53
- [3] Alessandro Tengattini, Arghya Das, Giang D. Nguyen, Gioacchino Viggiani, Stephen A. Hall, Itai Einav, A thermomechanical constitutive model for cemented granular materials with quantifiable internal variables. Part I—Theory, . *J. Mech. Phys. Solids*, Volume 70, 2014, Pages 281-296, ISSN 0022-5096,
- [4] Arghya Das, Alessandro Tengattini, Giang D. Nguyen, Gioacchino Viggiani, Stephen A. Hall, Itai Einav, A thermomechanical constitutive model for cemented granular materials with quantifiable internal variables. Part II – Validation and localization analysis, *J. Mech. Phys. Solids*, Volume 70, 2014, Pages 382-405,
- [5] Vatsala, A., Nova, R., and Murthy, S. Elastoplastic Model for Cemented Soils. (2001) *J. Geotech. Geoenviron. Eng.* 127(8): 679-687.
- [6] D. Krajcinovic. Selection of damage parameter Art or science ? (1998) *Mech. of Materials* 28: 165-179,
- [7] Einav, I. Breakage mechanics-Part I: Theory. (2007) *J. Mech. Phys. Solids*. 55(6):1274-1297.
- [8] Einav, I. Breakage mechanics-Part II: Modelling granular materials. (2007) *J. Mech. Phys. Solids*. 55(6): 1298-1320.
- [9] M. R. Coop and J. H. Atkinson, The mechanics of cemented carbonate sands, (1993) *Geotec.* 43: 53-67.
- [10] J. Huang and D. Airey, Properties of artificially cemented carbonate sand. (1998) *J. Geot. Geoenviron. Eng.* 124,6 :492-499.
- [11] Ando, E., Hall, S.A., Viggiani, G., Desrues, J., Besuelle, P. Grain-scale experimental investigation of localised deformation in sand: a discrete particle tracking approach, (2011) *Acta Geotech.* 7-1: 1-13
- [12] Tengattini, Alessandro, et al. "Double-Scale Assessment of Micro-mechanics Based Constitutive Models for Granular Materials Undergoing Mechanical Degradation." *Bifurcation and Degradation of Geomaterials in the New Millennium*. Springer International Publishing, 2015. 175-180.
- [13] Gkiousas-Kapnisis, Marios, et al. "Development of image analysis tools to evaluate in-situ evolution of the grain size distribution in sand subjected to breakage." *Bifurcation and Degradation of Geomaterials in the New Millennium*. Springer International Publishing, 2015. 253-258
- [14] Tengattini, Alessandro, and Edward Andò. "Kalisphera: an analytical tool to reproduce the partial volume effect of spheres imaged in 3D." *Measurement Science and Technology* 26.9 (2015): 095606.

Structures

TUNNELLING IN ANISOTROPIC SQUEEZING CONDITIONS

Huy TRAN-MANH (manh-huy.tran@enpc.fr), Jean SULEM
École des Ponts ParisTech, Champs-sur-Marne, France.

ABSTRACT.As part of the Lyon–Turin project, the excavation of the Saint-Martin-La-Porte access adit between 2003 and 2010 encountered severe operational difficulties in the coal schists section associated with an extreme squeezing condition. Careful instrumentation of displacement measurements of the tunnel walls along different directions clearly showed important anisotropic behaviour, in accordance with the preferential directions of the main mechanical weakness planes. In this paper, the analysis of the convergence measurements is performed for the sections between chainage 1250 and 1385 where the largest displacements have been recorded. By assuming an elliptic deformation of the tunnel walls, a preliminary geometrical treatment of the raw data is presented to determine the principal axes of deformation. A new anisotropic time-dependent constitutive model, which includes ubiquitous joints of specific orientation embedded in a viscoplastic medium, is then proposed. 3D numerical simulations with the new model are carried out to back analyse the convergence measurements.

1. Introduction

During the excavation of Saint-Martin-La-Porte access adit, extreme squeezing conditions occurred when the tunnel encountered the Carboniferous Formation, exhibiting strong time-dependent and highly anisotropic convergence of cross-section. The squeezing behavior observed in this access gallery has been analyzed in several studies, emphasizing either the time-dependent behavior (Barla et al. 2008, 2011, Pellet 2009) or the anisotropic behavior of rock mass (Russo et al. 2009, Vu et al. 2013a,b). The present paper aims to propose a new model that considers both anisotropic behavior and explicit time-dependent deformation of the rock mass to investigate the squeezing behavior of the Saint-Martin-La-Porte access adit.

2. Geological conditions

Apart from recent superficial formations, the rock masses encountered in the Saint-Martin-La-Porte access adit belong to the internal structural zones of the Alps, characterized by an extreme geological complexity from both lithological and structural points of view. The section of the access gallery is characterized by the overlapping of the “HouillèreBriançonnaise” zone on the “Sub-briançonnaise” zone, originating a contact marked by Triassic formations (gypsum and anhydrite), called “Front du Houiller” (Figure 1). In particular, the tunnel has been excavated in the “Productive Carboniferous Formation” (Encombres Unit) which is composed of schists and/or carboniferous schists (45–55 %), sandstone (40–50 %) and a significant proportion of cataclastic rocks (up to 15 %) (Barla et al. 2008). A characteristic feature of the ground observed at the face during excavation is the anisotropic, highly heterogeneous, disrupted and fractured conditions of the rock mass, which exhibits a very severe squeezing behavior. Several traditional support systems were used but would not be feasible to cope with the severe squeezing conditions encountered. A novel excavation and support method was finally adopted with highly deformable elements inserted in the shotcrete lining which allowed for controlled deformation and stress in the rock mass and in the supports (Barla et al. 2008, BoninietBarla 2012).

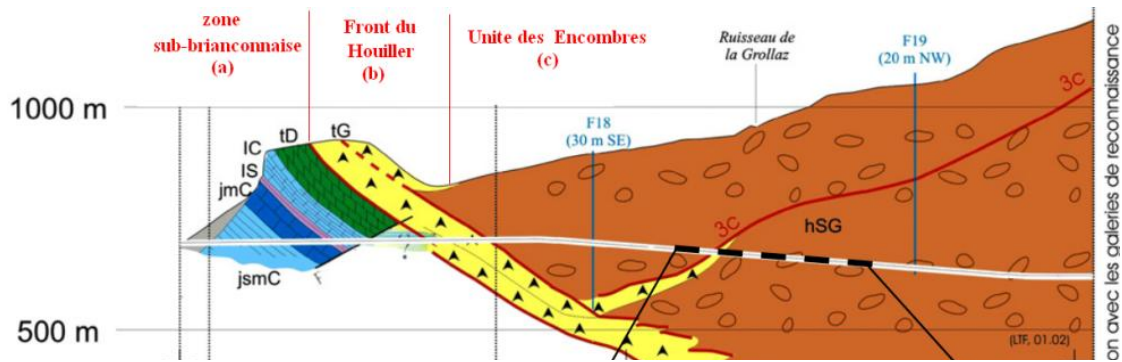


Figure 1. Geological profile.

3. Monitoring data during the excavation

The excavation of the Saint-Martin-La-Porte access gallery has been associated with a program of intensive geological and geotechnical monitoring. Convergence measurements were carried out by optical ranging on regularly spaced sections equipped each with five monitoring points along the perimeter of the section. In most cases, the initial measurements are taken less than 3 m away from the tunnel face. The convergence is defined as the shortening of the distance between two opposite points on the wall of the gallery. Figure 2a shows typical relative convergence curves at chainage 1311 m in an area of large convergence. The following observations can be made:

- the magnitude of the convergence is very high, up to 2 m after 145 days;
- the deformational behavior is highly anisotropic, with a maximal convergence in almost case along arrays 1-3 and 1-5;
- deformations keep increasing even during face stops, which shows a time-dependent behavior of the rock;
- the face advance causes an increase in the rate of deformation even when the face is far from the considered section; hence the influence zone of the tunnel face is very large.

The convergence curves depend on the orientation of the arrays and on its initial length. These data can be analyzed globally by calculating the mean value over various arrays or the maximum one. However, such a choice results in an important underestimation of the real convergence of the gallery, since monitoring points are not perfectly diametrically opposed to each other.

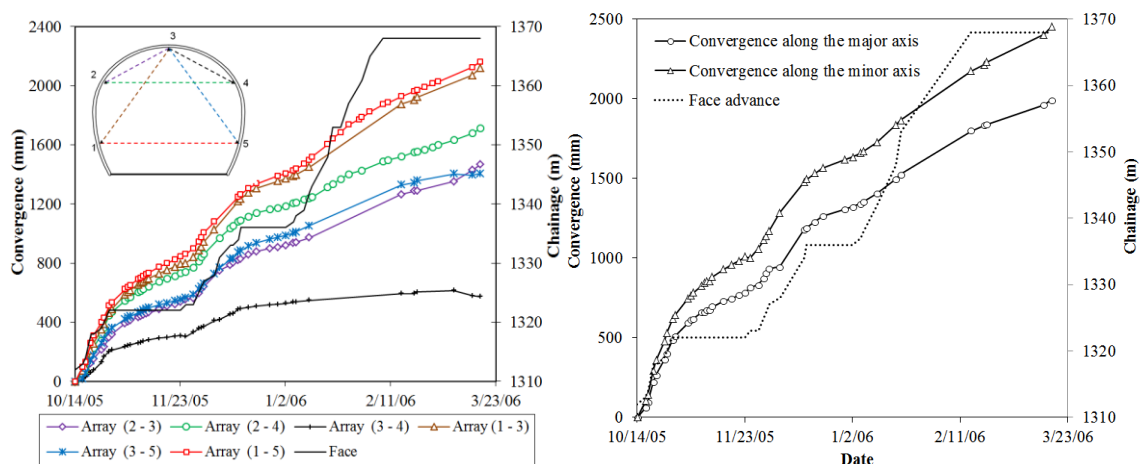


Figure 2. Example of convergence measurement (a) and convergences along two principal directions of deformation (b) at Chainage 1311 m.

Starting with a quasi-circular initial cross-section, the convergence data and the observation clearly show an ovalization of the cross-section with face advance. In order to describe the anisotropy observed in the gallery, a method for geometrical processing of the measurement data was proposed (Vu et al. 2013b). The evolution of the cross-section is described by fitting the cross-section with an ellipse. After the projection of the points on the mean vertical plane of the cross-section considered, an elliptical approximation of the actual shape of the deformed section is carried out by fitting the 5 parameters of this ellipse, which are the two semi-axes lengths a and b , the orientation α and the coordinates (X_c, Y_c) of the center of the ellipse. The principal axes of the ellipse give directly the principal directions of deformation and the convergences along both semi-axes of the ellipse are evaluated (Figure 2b).

4. Anisotropic time-dependent deformation modelling

Constitutive model

Starting with the concepts of pseudo-discontinuous anisotropic approach, Tran-Manh et al. (2015) have proposed a new anisotropic time-dependent constitutive model that includes one set of ubiquitous joints of specific orientation embedded in a viscoplastic medium. As such, the ubiquitous joint model is used to simulate the anisotropy while a viscoplastic model of the matrix is used to account for the time-dependent behavior of the rock mass (Figure 3a).

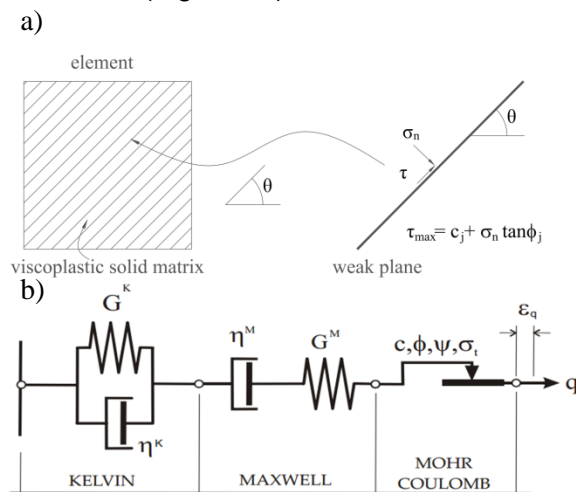


Figure 3. Ubiquitous joint model in a viscoplastic matrix.

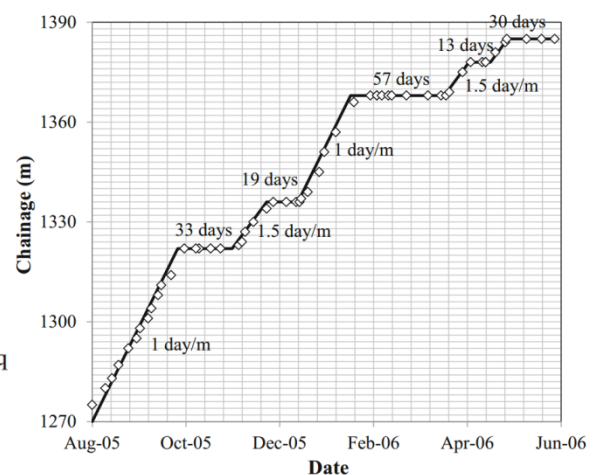


Figure 4. Face advancement in the length considered for numerical modeling.

The Burger-creep visco-plastic model (CVISC) is used to characterize the solid matrix. The advantage of this model is that it is rather simple to use and that the parameters that drive the “short term behavior” are separated from those driving the “long term behavior”, even in a true scale problem. Instantaneous deformations are computed using an elasto-plastic constitutive model involving the Mohr-Coulomb failure criterion and the time-dependent deformations are driven by the Burgers model (Figure 3b). The sliding behavior on the joints (weak-plane) is governed by an elasto-plastic model with the Coulomb failure criterion.

Yielding may occur either in the solid or along the weak planes, depending on the stress state, the orientation of the weak planes and the material properties of the solid and weak planes.

The model is characterized by 13 constitutive parameters as follows: 9 parameters for the mechanical behavior of the solid (elastic bulk modulus K , Kelvin shear modulus

G^K , Kelvin viscosity η^K , elastic shear modulus G^M , Maxwell dynamic viscosity η^M , cohesion c , mass density ρ , dilation angle ψ , angle of internal friction ϕ and tension limit σ_t ; 4 parameters for the behavior of the weak-plane (joint cohesion c_j , joint friction angle ϕ_j , joint tension limit σ_{tj} and joint dilation angle ψ_j). In addition, two geometric parameters describe the orientation of the weak-plane (dip angle and dip direction of weakness plane).

Numerical simulation

Saint Martin La Porte access gallery are analyzed. We pay particular attention to the sections that have been excavated with the P7.3 soft support system. Its influence on the rock mass deformation is actually neglected in the computations. The sections between chainage 1250 and 1385 are investigated. The overburden there is approximately 300 m. The initial state of stress in the ground is assumed to be hydrostatic and equal to 8.5 MPa (Barla et al. 2010, Vu et al. 2013a). The water table is not present; therefore, any time-dependent effects induced by variations of pore-water pressure can be disregarded (Barla et al. 2011). The tunnel initial cross section is assumed to be circular, with an equivalent radius R of 5.5 m. A full-face excavation is considered. The face advancement history during the time window considered is shown in Figure 4. Five excavation phases, with rate of 1÷1.5 day/m, alternating with five stops of face advance have been considered.

Numerical analysis of the tunnel response is performed using the Finite Difference code FLAC3D in which the anisotropic creep model described above has been implemented. As the cross-section is circular and the initial stress state is hydrostatic, the joints are assumed to be horizontal in 3D model and hence the quarter-symmetry 3D mesh is sufficient (Figure 5). In order to simulate the excavation sequence and minimize boundary effects, the size of the model must be large enough. The far-field boundaries are placed at a distance of 16 radii from the axis of the tunnel and the length of the model in axial direction is 24 radii. The mesh is uniformly refined in the axial direction while the element size increases gradually in the radial direction from the tunnel wall, to decrease the number of zones. The mesh is finely discretized near the excavation perimeter with a typical element size of 0.5 m. Zero-displacement boundary conditions are imposed. The in-situ stresses are initially imposed everywhere in the domain. The excavation sequence versus time has been simulated numerically by means of discrete advancement steps of 1.0 m.

As the rock mass is highly heterogeneous, very stratified, and highly fractured, there is a scale effect and the in situ characteristics differ from those measured in the laboratory. Therefore, the calibration of the constitutive parameters is not based on laboratory tests, but on a back analysis of the convergence data collected during the tunnel construction. For consistency with previous numerical works on the simulation of Saint-Martin-la-Porte gallery (Russo et al. 2009, Pellet 2009, Barla et al. 2011), we take numerical values for the parameters describing the elastoplastic behavior of the isotropic rock matrix as: $E = 650$ MPa, $\nu = 0.3$ ($G^M = 250$ MPa), the friction angles are fixed both in the solid matrix $\phi = 26^\circ$ and on the ubiquitous joints $\phi_j = 23^\circ$; zero dilatancy is assumed ($\psi = 0^\circ$, $\psi_j = 0^\circ$) and the tension limit is $\sigma_t = \sigma_{tj} = 8.5$ kPa. The remaining parameters including the cohesion in the solid matrix c and on the ubiquitous joints c_j and the three parameters η^K , η^M and G^K for describing the time-dependent behavior of the rock matrix are evaluated by numerical simulations (Tran-Manh et al. 2015).

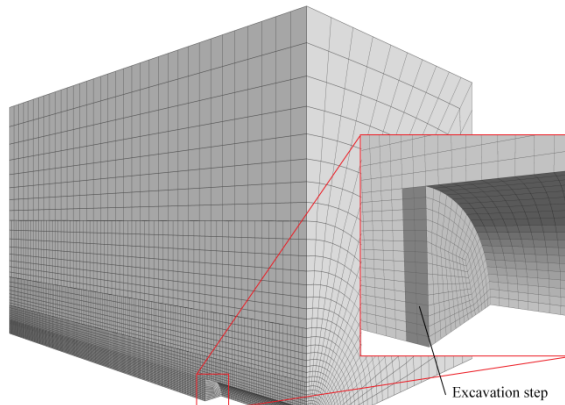


Figure 5. 3D mesh for FLAC3D computations.

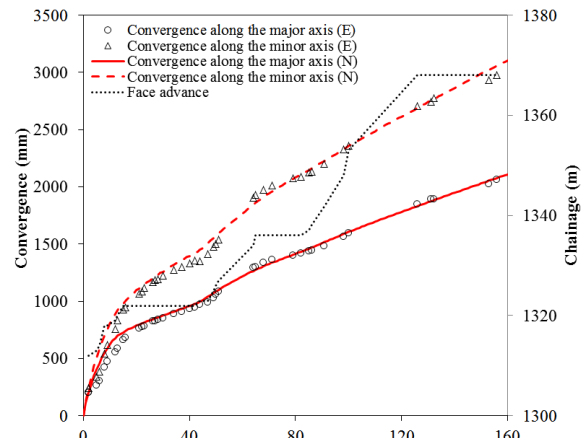


Figure 6. Comparison between the measurements (E) and the numerical results (N) at chainage 1311 m.

5. Comparison of monitoring data with numerical results

Numerical simulations have been performed for sections situated between chainage 1250 m and 1385 m. A total of 11 monitoring sections are investigated. An example of the comparison between computed and measured radial displacements of the tunnel wall along the two principal directions of deformation at chainage 1311 m is shown in Figure 6. The agreement of the numerical results with the observed values over a period of approximately 160 days is excellent. The constitutive parameters obtained are reported in Table 1. This permit to distinguish three zones, which are characterized with different parameters of the viscous (Kelvin, Maxwell) elements parameters for the rock matrix. The heterogeneity of the rock mass from one section to another is described with different values of the cohesion of the rock matrix (c) and of the weak-planes (c_j). The friction angle of the rock matrix and the weak-planes are taken constant for all sections studied. The ratio between the cohesion of the rock matrix and one of the weak-planes can be used to characterize the degree of anisotropy of rock mass. In zone 1 (from PM 1272 to PM 1298) and zone 3 (from PM 1267 to PM 1284), this ratio in the range 1.7- 3.8 exhibits a high anisotropic behavior of rock mass. On the contrary, in zone 2 (from PM 1311 to PM 1342), this ratio is smaller than 1.5 which shows a less anisotropic response. This result is compatible with the anisotropy ratio of convergence β defined from the analysis of convergence measurements (see Table 1 in Vu et al. 2013b).

6. Conclusions

This paper proposes a three dimensional constitutive model which combines the time-dependent behavior of an isotropic rock matrix and sliding along preferred orientations, the “ubiquitous joints”. As such it is capable of modeling both the time-dependent and the anisotropic deformations which are often observed in squeezing tunnels. The proposed model has been implemented into the finite difference code FLAC3D in order to back-analyze convergence data from the Saint-Martin-La-Porte access gallery. The numerical simulations show that the anisotropic behavior of the rock mass observed can be very well captured using the proposed model.

In this paper, we investigate only cross-sections between chainage PM 1,250 and PM 1,380 where a soft support system was installed and the influence of the support system is neglected. Numerical analyses of the yield-control support system with highly

deformable elements inserted in the shotcrete lining are preformed to study the effect of rock anisotropy on its behaviour (Tran-Manh 2014). Finally, we note that the anisotropic model can be easily generated using any other creep model for describing the solid matrix isotropic behavior.

Table 1. Constitutive parameters of the proposed model between chainage PM 1250 and PM 1385.

PM	Solid matrix							Joint	
	E (MPa)	ν -	G^K (MPa)	η^K (GPa.day)	η^M (GPa.day)	c (MPa)	φ (°)	c_j (MPa)	φ_j (°)
1272						0.80		0.25	
1278						0.45		0.35	
1284	650	0.3	250	6.25	35.00	0.40	26	0.18	23
1291						0.42		0.25	
1297						0.45		0.20	
1311						0.65		0.45	
1331	650	0.3	250	1.25	10.00	0.70	26	0.50	23
1342						0.73		0.70	
1367						1.55		0.40	
1375	650	0.3	550	2.20	13.75	1.30	26	0.35	23
1384						1.20		0.42	

7. References

- Barla, G., Bonini, M., & Debernardi, D. (2008). Time Dependent Deformations in Squeezing Tunnels. In 12th IACMAG. Goa, India.
- Barla, G., Debernardi, D., & Sterpi, D. (2011). Time-dependent modeling of tunnels in squeezing conditions. *Int. J. Geomech ASCE*, (December), 697–710. doi:10.1061/(ASCE)GM.1943-5622.0000163.
- Bonini, M., & Barla, G. (2012). The Saint Martin La Porte access adit (Lyon–Turin Base Tunnel) revisited. *Tunnelling and Underground Space Technology*, 30, 38–54. doi:10.1016/j.tust.2012.02.004.
- Pellet, F. (2009). Contact between a tunnel lining and a damage-susceptible viscoplastic medium. *Comput Model Eng Sci*, 52(3), 279-295.
- Russo, G., Repetto, L., Piraud, J., & Lavignerie, R. (2009). Back-analysis of the extreme squeezing conditions in the exploratory adit to the Lyon-Turin base tunnel. *Rock Engineering in Difficult Conditions*, Toronto, ON, Canada.
- Tran-Manh, H., Sulem, J., Subrin, D., & Billaux, D. (2015). Anisotropic Time-Dependent Modeling of Tunnel Excavation in Squeezing Ground. *Rock Mech & Rock Eng*. doi:10.1007/s00603-015-0717-y.
- Tran-Manh, H. (2014). Comportement des tunnels en terrain poussant. PhD Thesis, Université Paris Est, France.
- Vu, T. M., Sulem, J., Subrin, D., & Monin, N. (2013a). Semi-Analytical Solution for Stresses and Displacements in a Tunnel Excavated in Transversely Isotropic Formation with Non-Linear Behavior. *Rock Mech & Rock Eng*, 46(2), 213–229. doi:10.1007/s00603-012-0296-0.
- Vu, T. M., Sulem, J., Subrin, D., Monin, N., & Lascols, J. (2013b). Anisotropic Closure in Squeezing Rocks: The Example of Saint-Martin-la-Porte Access Gallery. *Rock Mech & Rock Eng*, 46(2), 231–246. doi:10.1007/s00603-012-0320-4.

MECHANICAL CHARACTERISTICS OF MONOPILE FOUNDATION IN SAND FOR OFFSHORE WIND TURBINE

Nuo Duan (duannuo37@hotmail.com)
University College London, London, UK.

Yi Pik Cheng
University College London, London, UK.

ABSTRACT. The behaviour of monopile foundations for offshore wind turbines deviates from classical assumptions and accumulated experience mainly due to their large diameter, reduced slenderness. The offshore environment poses an additional challenge of having large numbers of load cycles from wind and waves. These cyclic loads may change the soil properties and hence how the pile responds to the loads. Both of these issues are still not well understood and not being properly incorporated in current design guidelines. In drained sands, the accumulating displacements can lead to foundation failure. On the other hand, the effects of the long-term cyclic loading on the foundation's deformation and especially on its serviceability must also be studied. The purpose of this work was to gain an insight into both aspects, by developing a reasonable numerical tool for the soil-pile interaction, and hence exploring better criteria for design.

1. Combined loading tests

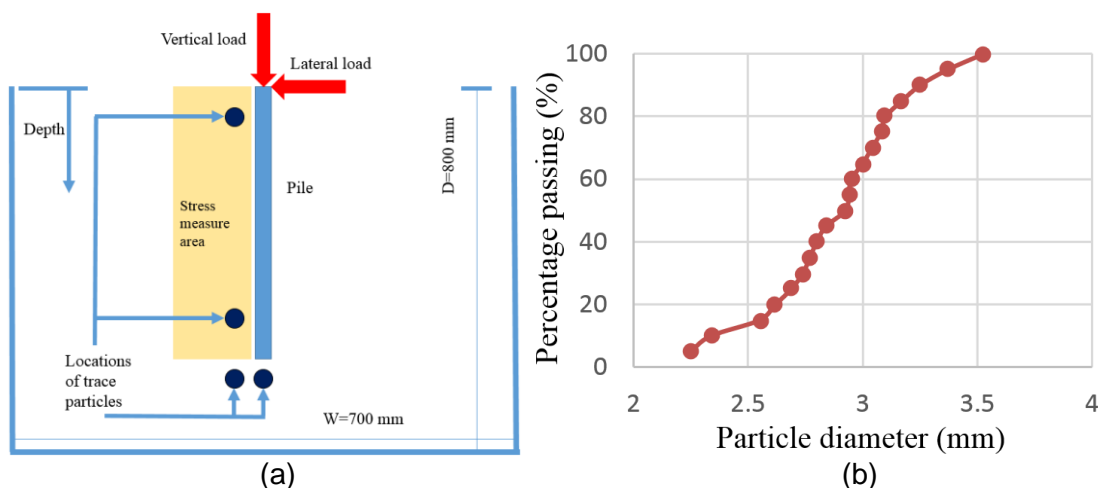


Figure 1. (a) Schematic view of the PFC model; (b) Particles size distribution in DEM simulation.

A 2D-Discrete Element Method (DEM) model that is used to study situations when vertical, lateral and combined loads are applied to a rigid monopile. At present, monopile foundations are widely used to support the tall and heavy wind turbines, which are also subjected to significant forces from wind and wave actions. Design guidance on the issue is limited, as well as the availability of laboratory and field test data. The interpretation of these results in sand, such as the relation between loading and displacement, relies mainly on empirical correlations to pile properties. A DEM model was used to study the combined loading behaviour. Verification of the DEM model was carried out by comparing simulation data against a model pile. Analyses of the model pile under pure vertical, pure lateral and combined loads are presented. They should offer insights on further research to optimise the design of mono-pile foundations to resist live loads in service.

All DEM analyses in this investigation were performed using the 2D PFC program. Fig 1(a) shows a sketch for analysis of pile-soil interaction and Fig 1(b) gives the particles

size distribution. The properties of material was shown in Duan & Cheng (2015). The pile was treated as a rigid material in view of high rigidity of a typical monopile, hence the consideration of bending moment was ignored. The vertical load and lateral load was applied to the ground surface on the top of pile.

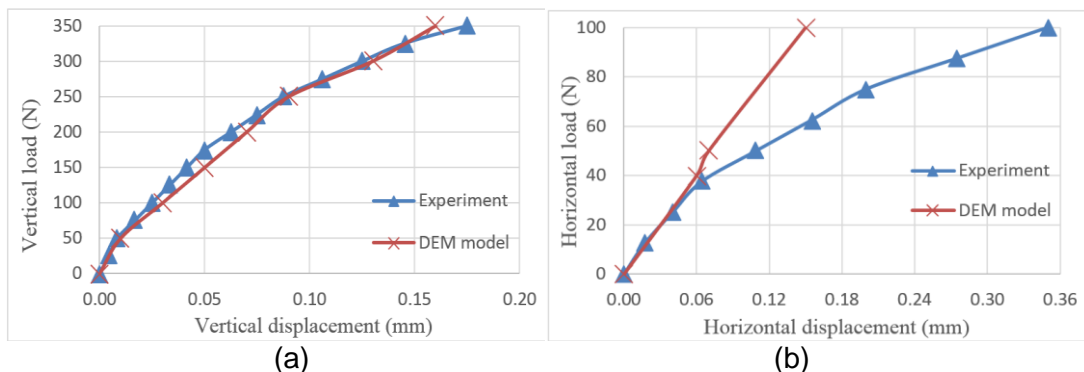


Figure 2. Figure legend Comparison of DEM predicted vertical and lateral response of pile with experimental test data of Anagnostopoulos & Georgiadis (1993): (a) vertical response of pile; (b) lateral response of pile.

Fig2(a) shows that the comparison is very good both at small and larger load levels for vertical response of pile. For the lateral responses of the pile, shown in Fig2(b), the comparison is good at a smaller horizontal load, but the percentage difference increases at the larger load levels. Up to a lateral displacement equal to 0.33% of the pile diameter, the difference between the measured and predicted pile loads is less than 6.25%. At a larger displacement equal to 0.84% of the pile diameter, the difference increases to approximately 54.28%. This deviation is acceptable in view of the many uncertainties in choosing the sand properties in the analysis, and also due to the rigid assumption of the monopile model. And the other main reason is that the actual experiment was performed in three-dimensions. Due to the good match at the relationship between vertical load and axial displacement, it is concluded that the numerical scheme adopted in the present investigation should be capable of modelling the pile-soil interaction under pure vertical load, lateral load, and a combination of vertical and lateral loads.

From this research, vertical load has a profitable influence on the lateral response of piles embedded in sand. This implies that it is conservative to design piles assuming that there is no interaction between axial and lateral loads. The traces of particles movements showed that there were obvious settlements of the soil particles near the bottom of the pile when there was a bigger vertical load. This should lead to soil densification near the pile tip and an increase in the lateral pile capacity under the combined loading condition. (Duan & Cheng, 2015).

2. Sample preparation

A modified technique, named as the Grid Method (GM), capable of generating homogeneous specimens for model scale centrifuge studies using the DEM. The DEM specimens were temporarily are divided into grids so that soil particles could be created in batches into a smaller area. Using the specimen, a 2D DEM-centrifuge model was prepared by applying an increased gravity condition, which was then used to study the monotonic loading behaviour of a rigid monopile. The input parameters for this DEM model was shown in Table 1.

Table 1. Input parameters for DEM simulations.

Density of sand particles (kg/m ³)	2650
--	------

Particle diameters, d (mm)	Fig. 3 (c)
Sand grain size, d ₅₀ (mm)	5.85
Friction coefficient of the particles μ(-)	0.5
Sand Young's Modulus, E _p (Pa)	4e7
Contact normal stiffness of particles, k _n (N/m)	8e7
Particle stiffness ratio (k _s /k _n)	0.25
Contact normal stiffness of walls, k _n (N/m)	6e12
Initial average porosity	0.25
Final average porosity	0.185
Bulk unit weight γ _{bulk} (kN/m ³)	2115.3

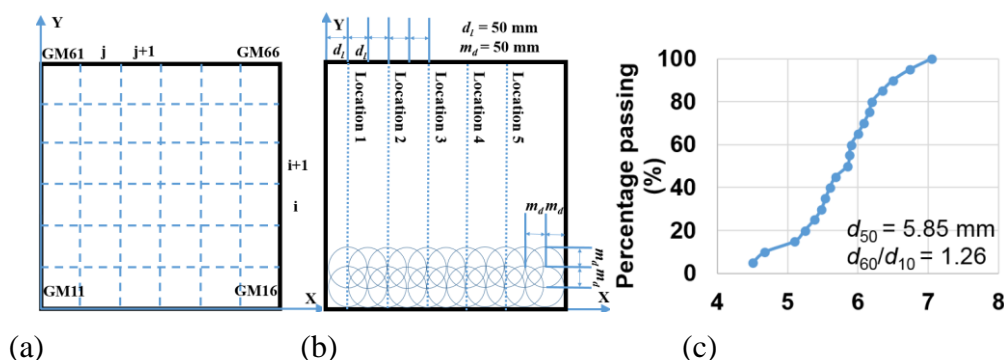


Figure 3. (a)(b)Schematic view of grid method;(c) Distribution of grain sizes in DEM analyses.

At the beginning of GM, the planned area of sample was divided into 36 grids (see Fig3 (a)), and there were 6 layers and 6 columns in this region. The each grid was square, each side were of 100 mm in length. The first grid which was named GM11 that was at the bottom-left of the model. “GM” is the abbreviation of grids method, then first number of “11” means the number of layer, second number stands for the number of column. Fig 1(b) shows the locations of the measurement circles (radius $m_d = 50$ mm) defined by the PFC intrinsic functions. These measurement circles were used to interpret the localized information within each grid. In the following simulations, 5 locations (location 1-5 of the Fig3 (b)) were picked to compare the final results. The input parameters for this DEM model was shown in Table 1.

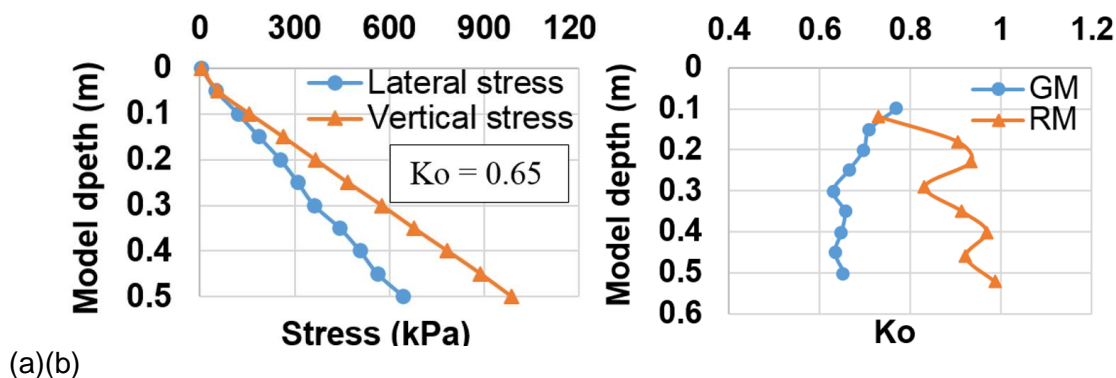


Figure 4. (a) Average lateral and vertical stress; (b) Comparison of K_0 between GM and RM.

Fig4(a) describes the comparison of average lateral and vertical stress distribution for different depths and shows K_0 is reasonable. Fig4 (b) expresses the comparison of K_0 -values of GM (Grid-Method) and previous RM (Random-generation Method) used in Duan & Cheng (2015), there is less amount of variation with depth. For the theory vertical stress, the sample density was calculated after the equilibrium state. Then function $p=\rho gh$ (p is the vertical stress, ρ is sample density, g is gravity, and h is depth) was used to calculate the theory vertical stress. From the Fig4 (b), there is only a slight difference. Combined with DEM-centrifuge model, it was found that the GM was efficient in preparing the dense samples because it reduced the overall sample preparation time and managed to generate more homogeneous specimens.

3. Monotonic loading tests

This part presents the data of a numerical model that is used to study the soil-structure interaction of a rigid monopile under monotonic loading using the 2D-DEM. It is found that the load-displacement curves of the DEM simulations compared well with a set of published centrifuge tests data. Fig 5 (a) shows the sketch view of the PFC model. The dimension of PFC model is same as the centrifuge experiment test which operated by Klinkvort (2013).

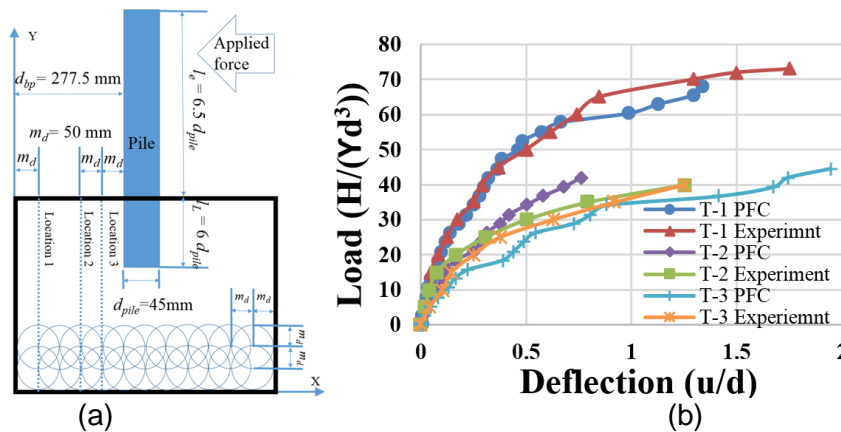
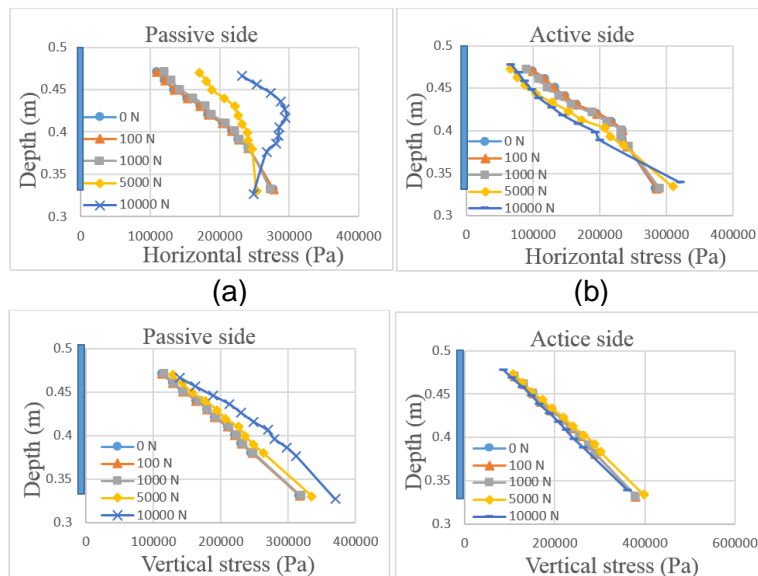


Figure 5. (a) Schematic view of the PFC model; (b) Comparison of DEM lateral response of pile with experimental test data of Klinkvort et al. (2010): T-1: $e=2.5d$; T-2: $e=4.5d$; T-3: $e=6.5d$.



(c) (d)

Figure 6. Lateral and vertical stress distribution comparison under different load level: (a)(b) Horizontal stress distribution at passive and active sides; (c)(d) Vertical stress distribution at passive and active sides.

Fig 5 (b) shows that there is a clear difference in the load-deflection curve for eccentricity of $6.5d$ and $4.5d$ or $2.5d$. The results matched well with the experiment data of Klinkvort *et al.* (2010). Failure is defined as the load correspond to a settlement equal to 10% of the pile diameter. The figures show that, before the failure, the results of DEM model are nearly same as the centrifuge experiment. Due to the good match at the relationship between lateral load and horizontal displacement, it is concluded that the numerical scheme adopted in the present investigation should be capable of modelling the pile-soil interaction under higher gravity condition (100 g).

Fig 6(a) and (b) show that these two sides' trends are opposite. (c) and (d) indicate that the results are nearly the same as the accordingly horizontal stress trend. The monotonic tests revealed a relationship between the lateral bearing capacity of the pile and the load eccentricity. This indicates that there are different failure mechanisms for piles with large load eccentricity and piles with smaller load eccentricity.

4. Cyclic loading tests

This part presents the data of a series of 2D DEM simulations of a large-diameter rigid monopile subjected to cyclic loading under a high gravitational force. A non-dimensional framework is presented and applied to interpret the simulation results. The DEM data compares well with various sets of published experimental centrifuge model test data in terms of rotation and lateral deflection. The accumulated permanent pile lateral displacements and rotation induced by the cyclic lateral loads were found to be dependent on the characteristics of the applied cyclic load, such as the extent of the loading magnitudes and directions. In some particular situations, it was found to cause a significant increase in the accumulated rotation.

Table 2. Test program.

PFC	ζ_b	ζ_c	Diameter of pile (mm)	Experiment	ζ_b	ζ_c	Diameter of pile (mm)
T2-3	0.36	0.5	45	E2-3	0.25~0.29	0.54	28
T3-1	0.36	-0.5	45	E3-1	0.33~0.34	-0.5	40
T4-3	0.36	0	45	E4-3	0.15~0.36	0.05	40

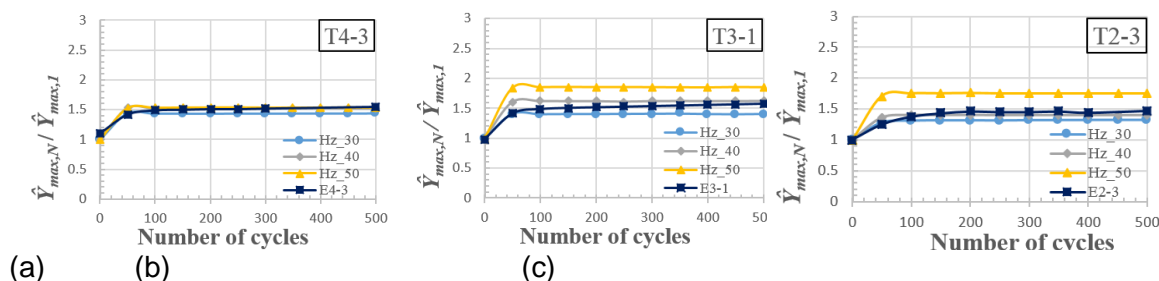


Figure 7. Comparison of DEM lateral response of pile with experimental test data (Klinkvort *et al.*, 2010)

The parameters of DEM tests were summarised in Table 2. In Fig 7, there figures show the comparison of DEM lateral response of pile with experimental test data with different frequencies (30 Hz, 40 Hz and 50 Hz). The centrifuge tests were operated by Klinkvort (2013). When the ζ_b value is closed to 0.36, the model result is approached to the experiment data. At the meantime, the best match is the 40 Hz, so this value also is chosen for the following PFC model tests.

The key issue-accumulation of displacements for the design of a monopile for wind turbine was investigated. The model data was matched well with the experiment data. And the frequency was chosen at 40 Hz. It was clearly seen that the accumulation of displacement is affected by the characteristic of the cyclic loading, and by the load amplitude (Augustesen *et al.*, 2010). The ongoing work aims to identify exact mechanisms that leads to the different behaviour at different ζ_c .

5. Conclusions

Several DEM models were developed in this research, including (1) a 2D monopile model to investigate the combined loading phenomenon, (2) a modified method of generating specimens for 2D DEM centrifuge model, (3) a micromechanics study of monopile under monotonic loading using DEM, (4) a study of monopile under cyclic loading using DEM. DEM is useful when looking into macro and micro scale problems (Cheng, 2004). It becomes extremely useful tool, if applied with wisdom, to identify the correct micromechanical behaviour, as it is clear that the future of soil mechanics lies in producing accurate constitutive models that have sound micromechanical bases. The effect of long term loading on monopile cannot be found from the triaxial test and regular constitutive model. With regard to the particles near the pile, their motion, densification and breakage will decide the influence of the long term loading. That why we need focus on the microscale discrete particles which cannot be modelled with FEM. With the development of modern computer, we can use the numerical particle model to simulate the whole process. Some characters of the constitutive model will be appeared from the numerical model automatically. Consequently, DEM is proved to be the efficient tool in simulating the complicated problems of granular flow and solid mechanics.

6. References

- Anagnostopoulos, C., & Georgiadis, M. (1993). Interaction of Axial and Lateral Pile Responses. *Journal of Geotechnical Engineering*, 119(4), 793-798.
- Augustesen, A. H., Sørensen, S. P. H., Ibsen, L. B., Andersen, L., Møller, M., & Brødbæk, K. T. (2010). *Comparison of calculation approaches for monopiles for offshore wind turbines*. Paper presented at the The European Conference on Numerical Methods in Geotechnical Engineering.
- Cheng, Y. P. (2004). *Micromechanical investigation of soil plasticity*. (PhD), Cambridge University.
- Duan, N., & Cheng, Y. P. (2015). *A 2D DEM mono-pile model under combined loading condition*. Paper presented at the Geomechanics from Micro to Macro, Cambridge.
- Klinkvort, R. T. (2013). *Centrifuge modelling of drained lateral pile - soil response: Application for offshore wind turbine support structures*. Technical University of Denmark.
- Klinkvort, R. T., Leth, C. T., & Hededal, O. (2010). *Centrifuge modelling of a laterally cyclic loaded pile*. Paper presented at the Physical Modelling in Geotechnics.

A PROBABILISTIC APPROACH FOR RAINFALL-INDUCED LANDSLIDE SUSCEPTIBILITY AT LARGE SCALE

Fanelli Giulia (giulia.fanelli@strutture.unipg.it)

Department of Civil and Environmental Engineering, University of Perugia, Italy.

ABSTRACT. In this work, a new probabilistic model for rainfall-induced landslide prediction at large scale is proposed. It represents an extension of the deterministic TRIGRS model proposed by Baum et al. (2002) to the probabilistic case, using the Point Estimate Method (PEM) for the evaluation of the Probability of Failure. The model accounts for the spatial variability of the soil strength properties by applying the kriging technique, which provides the synthetic indicators for the definition of the probability density functions of cohesion and friction angle. The hydraulic saturated conductivity is treated as a random variable as well. Besides, a negative correlation between cohesion and friction angle is considered. A comparison between PEM and Monte Carlo simulations has shown that PEM gives results with the same precision of Monte Carlo, but in much less time, resulting therefore an efficient tool for landslide prediction at large scale.

1. Introduction

As well known, modeling the physical process that leads a slope to instability conditions after a rainfall event is complex. Physically-based models are widely used in the common practice: they reproduce a physical process using analytical equations and considering the specific properties of the soil types in a study area.

The main distinction for physically-based models is related to the nature of the predictions: they can be deterministic or probabilistic. The deterministic approaches for susceptibility analysis do not consider any form of uncertainty in their implementation and regard the input variables (as well as the dependent variables) as fixed-value (Montgomery & Dietrich 1994, Iverson 2000, Baum et al. 2002, Baum et al. 2008, Salciarini et al. 2006, Montrasio & Valentino 2008, Cascini et al. 2010).

This limitation can be overcome by probabilistic models, which allow modeling uncertainties by considering the input variables as random, defined by a probability density function (PDF) and a correlation structure. In this way, the dependent variables are described as random variable as well.

As highlighted by Nadim (2007), working with uncertainty is an essential aspect of geotechnical engineering. Generally, uncertainty is due to: measurements error, difficulty in soil characterization, approximation of the hypotheses of the model used to reproduce the physical phenomenon, spatial variation of soil properties, etc.

To study the problem stochastically, several methods are suitable. The most famous are the Monte Carlo simulations and the Point Estimate Method.

The Monte Carlo approach represents a powerful tool to study landslide hazard. It consists in repeating a deterministic analysis for a very large number of times, varying each time the values of the input variables (according to specified probability density function), until the PDF of the output variable can be obtained. This method is largely used (Zhou 2003, Cho 2010, Wu 2013), despite its main drawback related to the high computational efforts required for carrying out the simulations.

The Point Estimate Method (PEM), originally developed by Rosenblueth (1975), represents a good alternative to Monte Carlo simulations. It requires knowing the statistical moments of the independent variables, necessary to select two points. By combining the two sample points of all the input variables, the statistical moments of the dependent variable can be computed and, therefore, the Probability of Failure can be obtained.

This work aims to demonstrate that the PEM is an efficient alternative to the widely used Monte Carlo approach for landslide predictions; in fact, Monte Carlo can be prohibitive for large-scale analyses, due to the significant number of simulations required. The comparison between the two probabilistic methods is performed for a single cell (i.e., for a single stratigraphic column), since it requires the minimum effort in terms of time. Then, after showing that the PEM gives results with the same accuracy as Monte Carlo, but in much less time, a probabilistic model for rainfall-induced landslide susceptibility at regional scale, based on the PEM, is described. In the end, an application of the new probabilistic method is proposed.

2. The new model for rainfall-induced landslide susceptibility

The probabilistic model for the prediction of shallow rainfall-induced landslides at large scale is written in *Matlab* and works with gridded area. It represents an extension of the TRIGRS model (Baum et al. 2002), valid for fully saturated conditions and based on an infinite slope stability model and on the linearized solution of the Richards equation proposed by Iverson (2000). TRIGRS computes the spatial-temporal evolution of the pore pressures and of the Factor of Safety in the soil, during a rainfall event.

The analysis is performed only in presence of loose soil covers, since the assumption of an infinite slope is reasonable for these soil types; conversely, the typical failure mechanism of rocks is represented by rockfalls and, therefore, cannot be modeled as shallow sliding. For this reason, the model provides probabilistic predictions only for those soil types corresponding to soil covers, while, in presence of rock types, the stability analysis is skipped.

For each cell of the study area, the model requires the following input soil properties: slope angle α , effective cohesion c' , friction angle φ' , unit weight of soil γ , saturated hydraulic conductivity k_s and oedometric modulus E_{ed} . Besides, the depth of the water table, the thickness of the soil cover, the steady pre-storm infiltration rate I_0 and the time t at which performing the analysis are required, as well as the characteristics of the rainfall event: the duration D and the intensity I .

The soil strength properties (cohesion and friction angle) are obtained by applying the geostatistical technique of kriging, as detailed in Fanelli et al. (2015): this is possible using an extensive database of geotechnical properties of the soils distributed in the Perugia province in central Italy. In that work, the spatial variability of the soil strength parameters has been investigated with geostatistical analyses finalized at the definition of the empirical variograms of the records included in the database, providing the weights necessary to apply the kriging method.

The soil covers identified in the Perugia province are listed in Table 1: for each of them, the empirical variograms of cohesion and friction angle are created and interpolated by the exponential model.

Table 1. Soil covers identified in the Perugia province.

Alluvium	Terraced alluvium
Clay	Eluvial deposit
Landslide deposit	Pyroclastic deposit
Gravel	Silt
Sand	Turbidite

The geostatistical module provides two quantities for each cell of the grid, essential for any probabilistic analysis: the expected value and the standard deviation, which represent the synthetic information on the probability density functions of the individual random variables controlling the hydraulic and mechanical process. The remaining soil

properties are assigned according to the soil classes in Table 1, on the basis of literature data.

In this model, the geotechnical properties treated as random variables are: the effective cohesion c' , the effective friction angle φ' and the saturated hydraulic conductivity k_s , described by the beta distribution, the normal distribution and the lognormal distribution, respectively. The choice of these probability distributions are justified in part by the results of the statistical analyses in Fanelli et al. (2015) and in part by literature (Baecher & Christian 2005, Zhai & Benson 2006).

As suggested by many authors (Lumb 1970, Li & Low 2010), cohesion and friction angle are characterized by a negative correlation coefficient ($\rho = -0.5$), while the correlation between the saturated hydraulic conductivity and the two soil strength parameters is assumed 0. In the following section, a comparison between two probabilistic methods is proposed, in order to select the most appropriate probabilistic model for rainfall-induced landslide susceptibility at large scale. Each of them provides a probabilistic prediction of the level of safety by means of the definition of the Probability of Failure, expressing the probability that the Factor of Safety (modeled using a normal PDF) is less than 1.

3. Comparison between Monte Carlo and PEM probabilistic methods

The comparison between Monte Carlo method and PEM on a single cell is finalized at demonstrating that the accuracy of Monte Carlo analyses can be obtained using PEM as well, which is a simpler and faster probabilistic method. Besides, PEM does not require knowing the exact probability density functions of the independent random variables as Monte Carlo, but only their statistical moments.

A crucial step in the Monte Carlo simulations is the generation of pseudo-random numbers, particularly if they are correlated (as cohesion and friction angle are). To this aim, the technique proposed by Nawathe & Rao (1979) has been used, based on the optimal linear prediction and the minimization of the error of prediction. Given two random variables X and Y , the procedure consists in the generation of two random sequences (following the assigned PDFs and not yet correlated): one for X and the other is a parent distribution of Y , which is rearranged to account for the correlation between X and Y . More details can be found in the paper of Nawathe & Rao (1979).

Another important aspect to consider in the Monte Carlo method is the number of simulations N to carry out. This number depends on the number of input random variables, along with the prescribed accuracy of the results. On one hand the number of simulations should be high enough, on the other, if N increases, the computational demand can be prohibitive. Once the number of simulations is set and a correspondent number of pseudo-random sequences is generated, the method consists in repeating N times a deterministic analysis, obtaining the data necessary to draw the PDF and the cumulative probability distribution CDF of the Factor of Safety. The Probability of Failure can be easily obtained as the value of the CDF corresponding to a unitary Factor of Safety.

The version of PEM used in this work is the one proposed by Panchalingam & Harr (1994), which, compared to the one proposed by Rosenblueth (1975), allows dealing with n correlated and skewed random variables. For three random variables, the PEM selects 6 sample points (2 for each one) and the dependent variable (the Factor of Safety F) is computed considering $2^3=8$ permutations of c' , φ' and k_s . For each estimate of F , a weighting function p is defined, accounting for correlation. The expected value and the standard deviation of the Factor of Safety are computed as follows:

$$E[F] = \sum_{i=1}^8 F_i p_i \quad (1)$$

$$\sigma[F] = \sqrt{E[F^2] - (E[F])^2} \quad (2)$$

Once known the mean and the standard deviation of F , the normal density function and the Probability of Failure can be extracted.

The geometrical, mechanical and hydraulic properties used for the comparison in the analyses are summarized in Table 2. The coefficients of variation of the three random variables are used to quantify their standard deviation, known their mean value. Their values are taken from literature for gravels. The depth of the water table is set as percentage of the soil cover thickness. The minimum and maximum values of the cohesion are necessary for the definition of the beta distribution parameters.

Table 2. Properties used in the comparison of the single cell.

Property	Value	Unit	Coeff. of variation for φ'	0.09	-
Slope angle	16	deg	Average k_s	1e-03	m/s
Soil cover thickness	4.9	m	Coeff. of variation for k_s	2.4	-
Average cohesion	1	kPa	Oedometric modulus	2e05	kPa
Coeff. of variation for c'	0.4	-	Unit weight of soil	20	kN/m ³
Minimum cohesion	0	kPa	Water table depth	50	%
Maximum cohesion	5	kPa	Rainfall duration	20	h
Average friction angle	30	deg	Rainfall intensity	10	mm/h

The results of the comparison between the two probabilistic methods are shown in Fig. 1 in terms of Factor of Safety (Fig. 1a) and Probability of Failure (Fig. 1b). PEM requires running only 8 simulations spending 0.014 s, while the time required by Monte Carlo analysis strictly depends on the number of simulations. Fig. 1a and 1b show that the results of Monte Carlo analysis are independent from N (i.e, tend to reach an asymptote) for a number of simulations greater than 1e04. Running at least 1e04 simulations, the results of Monte Carlo and PEM are almost the same, but Monte Carlo takes a time of around 0.14 s, which is one order of magnitude higher than the time required by PEM. Also the probability curves (PDFs and CDFs) of PEM and Monte Carlo have been compared. In particular, the distributions can be overlapped almost perfectly for at least 1e04 Monte Carlo simulations.

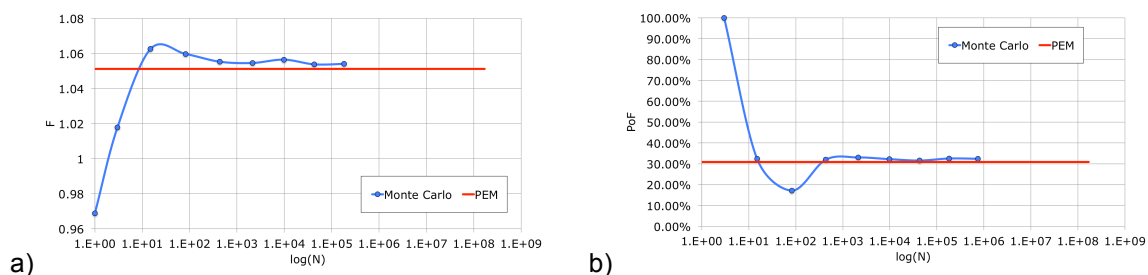


Figure 1. Comparison between Monte Carlo simulations and PEM, in terms of: a) Factor of Safety, and b) Probability of Failure.

This comparison shows that PEM provides as accurate results as Monte Carlo method, but in smaller times (about one order of magnitude less), which is a very attractive property when the analysis is referred to a large study area, rather than to a

single cell. This result has motivated the development of a probabilistic model for large-scale analyses based on the Point Estimate Method (Salciarini et al., submitted).

4. Application to a study area

The selected study area is in the center of the Perugia province of Umbria region and has an extension of 6 km x 6 km; it has been divided in 300 x 300 cells of 20 m side. The area has been selected for the high number of rainfall-induced landslides recently occurred.

Effective cohesion c' and friction angle φ' are evaluated, cell by cell, by applying the geostatistical technique of kriging to quantify the spatial correlation among the soil strength properties in the study area. For each cell, it is necessary to define: the slope angle, derived from the digital topography; the thickness of the soil cover d , derived from empirical relations, depending on the slope; the initial position of the water table, fixed in this application at the 80% of d for each cell; the rainfall intensity $I = 5$ mm/h and the rainfall duration $D = 24$ h.

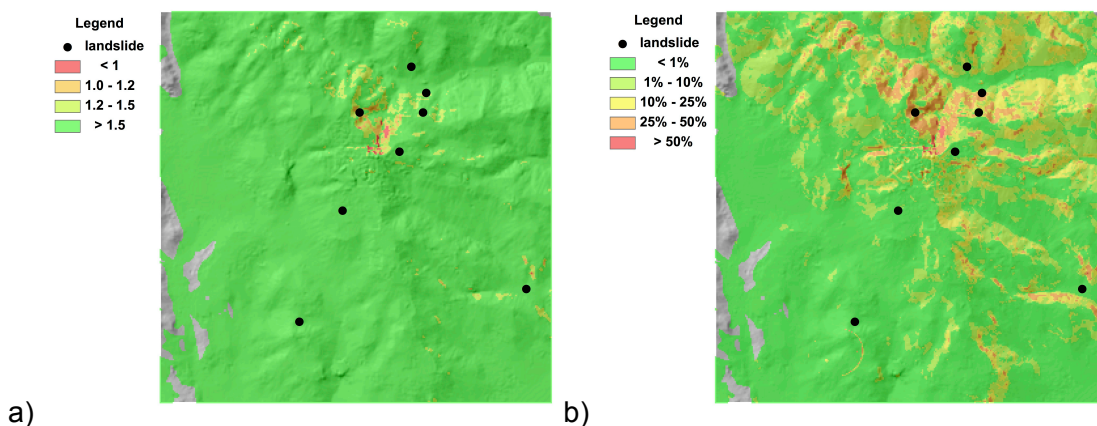


Figure 2. Results of the probabilistic model in the study area: a) expected Factor of Safety, and b) Probability of Failure.

The results of the probabilistic model are shown in Fig. 2, in terms of expected Factor of Safety (Fig. 2a) and Probability of Failure (Fig. 2b). The maps confirm the robustness of the developed model, showing good agreement between the probabilistic predictions and the landslides actually occurred in the area, particularly for the group of landslides on the north and on the eastern part of the area.

5. Conclusions

The work presented in this paper provides important results in the framework of the probabilistic modelling of landslides. A new probabilistic model, based on the TRIGRS code of Baum et al. (2002), has been developed, computing for each cell of a study area the Probability of Failure.

The comparison between the widespread Monte Carlo method and the simplified PEM has demonstrated that the latter gives results comparable to Monte Carlo, in much shorter times (around one order of magnitude less): this saving of time is fundamental in dealing with large areas, composed by millions of cells, which require that the analysis is repeated for each cell.

This work represents, therefore, an important validation of the probabilistic model developed by Salciarini et al. (submitted), consisting in an extension of the TRIGRS model through the probabilistic evaluation of the hazard operated by PEM. The

application of the model to a study area shows the reliability of the predictions of the probabilistic method.

6. References

- Baecher, G. B. & Christian, J. T. (2005). *Reliability and statistics in geotechnical engineering*, John Wiley & Sons.
- Baum, R. L., Savage, W. Z., & Godt, J. W. (2008). TRIGRS - a Fortran program for transient rainfall infiltration and grid-based regional slope-stability analysis, version 2.0. *US geological survey open- file report*, 08-1159.
- Baum, R. L., Savage, W. Z., & Godt, J. W. (2002). TRIGRS - a Fortran program for transient rainfall infiltration and grid-based regional slope-stability analysis. *US geological survey open- file report*, 424, 38.
- Cascini, L., Cuomo, S., Pastor, M., & Sorbino, G. (2010). Modeling of Rainfall-Induced Shallow Landslides of the Flow-Type. *J. Geotech. Geoenviron. Eng.*, 136(1), 85–98.
- Cho, S. (2010). Probabilistic Assessment of Slope Stability That Considers the Spatial Variability of Soil Properties. *Journal of geotechnical and geoenvironmental engineering*, 136(7), 975–984.
- Fanelli, G., Salciarini, D., & Tamagnini, C. (2015). Reliable soil property maps over large areas: a case study in central Italy. *Environmental & Engineering Geoscience*, 1078-7275.
- Iverson, R. M. (2000). Landslide triggering by rain infiltration. *Water resources research*, 36(7), 1897-1910.
- Li, H.-Z. & Low, B. K. (2010). Reliability analysis of circular tunnel under hydrostatic stress field. *Computers and Geotechnics*, 37: 50-58.
- Lumb, P. (1970). Safety factors and the probability distribution of soil strength. *Canadian Geotechnical Journal*, 7: 225-242.
- Montgomery, D. R. & Dietrich, W. E. (1994). A physically based model for the topographic control. *Water resources research*, 30: 1153-1171.
- Montrasio, L. & Valentino, R. (2008). A model for triggering mechanisms of shallow landslides. *Natural Hazards and Earth System Science*, 8.5: 1149-1159.
- Nadim, F. (2007). *Tools and strategies for dealing with uncertainty in geotechnics*, Springer.
- Nawathe, S. & Rao, B. (1979). A simple technique for the generation of correlated random number sequences. *IEEE Transactions on Systems, Man and Cybernetics*, 9: 96-102.
- Panchalingam, G. & Harr, M.E. (1994). Modelling of many correlated and skewed random variables. *Applied mathematical modelling* 18(11): 635-640.
- Rosenblueth, E. (1975). Point estimates for probability moments. *Proceedings of the National Academy of Sciences*, 72: 3812-3814.
- Salciarini, D., Fanelli, G. & Tamagnini, C. (submitted). A probabilistic and physically-based approach to model rainfall-induced shallow landslides at large scale.
- Salciarini, D., Godt, J. W., Savage, W. Z., Conversini, P., Baum, R. L. & Michael, J. A. (2006). Modeling regional initiation of rainfall-induced shallow landslides in the eastern Umbria Region of central Italy. *Landslides*, 3: 181-194.
- Wu, X. Z. (2013). Probabilistic slope stability analysis by a copula-based sampling method. *Computational Geosciences*, 17(5), 739-755.
- Zhai, H., & Benson, C. H. (2006). The log-normal distribution for hydraulic conductivity of compacted clays: Two or three parameters?. *Geotechnical & Geological Engineering*, 24(5), 1149-1162.
- Zhou, G., Esaki, T., Mitani, Y., Xie, M., & Mori, J. (2003). Spatial probabilistic modeling of slope failure using an integrated GIS Monte Carlo simulation approach. *Engineering Geology*, 68(3), 373-386.

Author Index

- Agofack Nicolaine, 45–50
- Bésuelle Pierre, 77–82
- Baille Wiebke, 64–69
- Bary Benoit, 83–88
- Benboundjema Farid, 83–88
- Bornert Michel, 89–94
- Cabrera Justo, 70–75
- Chambon René, 77–82
- Collin Frédéric, 77–82
- Cosenza Philippe, 70–75
- De Bresser Johannes, 58–63
- Duan Nuo, 108–113
- Dutto Paola, 20–25
- Fanelli Giulia, 114–119
- Fauchille Anne-Laure, 70–75
- Fortin Jérôme, 51–56
- Georget Fabien, 14–19
- Guéguen Yves, 51–56
- Hedan Stephen, 70–75
- Hellmich Christian, 39–44
- Hilaire Adrien, 33–38
- Honorio Tulio, 83–88
- Huet Bruno, 14–19
- Irfan-Ul-Hassan Muhammad, 39–44
- Lavergne Francis, 89–94
- Martin Stickle Miguel, 20–25
- Mayr Sibylle, 27–32
- Nicolas Aurélien, 51–56
- Niemeijer André, 58–63
- Pastor Manuel, 20–25
- Pichler Bernhard, 39–44
- Pimienta Pierre, 14–19
- Prévost Jean, 14–19
- Pret Dimitri, 70–75
- Ruiz Daniel, 8–13
- Sab Karam, 89–94
- Sanahuja Julien, 89–94
- Shapiro Serge, 27–32
- Spiers Christopher, 58–63
- Sviridov Viacheslav, 27–32
- Tengattini Alessandro, 95–100
- Toulemonde Charles, 89–94
- Tran-Manh Huy, 102–107
- Valle Valéry, 70–75
- Van Den Eijnden Bram, 77–82
- Verberne Berend Antonie, 58–63
- Yi Pik Cheng, 108–113